Pontifícia Universidade Católica
do Rio de Janeiro

**Helena Maria Borja Veiga**

# Study of wax deposits in pipelines



**TESE DE DOUTORADO**

Thesis presented to the Programa de Pós-Graduação em Engenharia Mecânica of PUC–Rio in partial fulfillment of the requirements for the degree of Doutor em Ciências –Engenharia Mecânica.

Advisor: Prof. Luis Fernando Alzuguir Azevedo

Rio de Janeiro
February 2017

Pontifícia Universidade Católica
do Rio de Janeiro

**Helena Maria Borja Veiga**

# Study of wax deposits in pipelines

Thesis presented to the Programa de Pós-Graduação em Engenharia Mecânica of PUC–Rio in partial fulfillment of the requirements for the degree of Doutor em Ciências –Engenharia Mecânica. Approved by the undersigned Examination Committee.

**Prof. Luis Fernando Alzuguir Azevedo**
Advisor
Departamento de Engenharia Mecânica — PUC–Rio

**Dr. Alexandre Mussumeci Valin de Freitas**
GE Centro Brasileiro de Pesquisas

**Dr. Daniel Merino Garcia**
Repsol

**Prof. Frederico Wanderley Tavares**
Universidade Federal do Rio de Janeiro

**Dr. Rafael Mendes**
Petrobras

**Prof. Marcio da Silveira Carvalho**
Vice Dean of Graduate Studies
Centro Técnico Científico — PUC–Rio

Rio de Janeiro — February 20th, 2017

**Helena Maria Borja Veiga**

Graduated in Mechanical Engineering at PUC-Rio in 2008 and obtained a degree of Master 2 in Complex Fluids at the University Paris Diderot, in 2009.



Bibliographic data

Veiga, Helena Maria Borja

Study of wax deposits in pipelines / Helena Maria Borja Veiga ; advisor: Prof. Luis Fernando Alzuguir Azevedo. — 2017.
190 f. : il. ; 30 cm

Tese (Doutorado em Engenharia Mecânica)-Pontifícia Universidade Católica do Rio de Janeiro, Rio de Janeiro, 2017.
Inclui bibliografia

1. Engenharia Mecânica – Teses. 2. Deposição de parafina. 3. Garantia de escoamento. 4. Temperatura da interface. 5. Condutividade térmica do depósito. 6. Envelhecimento do depósito. I. Azevedo, Luis Fernando Alzuguir. II. Pontifícia Universidade Católica do Rio de Janeiro. Department of Mechanical Engineering. III. Título.

CDD: xxx

## Acknowledgments



To god, for the beauty and mystery of all things, and for our capacity of perceiving it.

To my advisor, Professor Luis Fernando Azevedo, for his ingenious ideas, wise advises and full support, which encouraged and expanded my work.

To Luciana Souza and Professor Angela Nieckele for their laborious computational work, which enriched my work.

To Felipe Fleming and Guilherme Lima for their support with chemical analyses and for the rich discussions.

To my family that always offered me a safe harbor.

To Igor that kept life gentle during periods of hard work.

To my colleagues of PUC–Rio, who made the laboratory such a friendly place to work.

To Petrobras, for the continuous support of our activities along the years.

To Repsol-Sinopec Brasil for the support to this research project.

## Abstract

Veiga, Helena Maria Borja; Azevedo, Luis Fernando Alzuguir(Advisor). **Study of wax deposits in pipelines**. Rio de Janeiro, 2017. 190p. Tese de Doutorado — Departamento de Engenharia Mecânica, Pontifícia Universidade Católica do Rio de Janeiro.

The present research provided original information to aid the understanding of the physical mechanisms governing wax deposition in pipelines. The research program addressed a number of relevant open questions in the literature regarding the formation, growth and aging of the wax deposit layer. To this end, an experimental program was devised, following a strategy of conducting simple experiments, employing lab-scale test sections with well-defined boundary and initial conditions, and using simple test fluids with known properties. Measurements were performed in a rectangular and in an annular test section, both especially designed to allow for optical measurements of the time evolution of the spatial distribution of the wax deposit thickness. The test sections were equipped with heat flux sensor, temperature traversing probes and deposit sampling ports that allowed the measurement of relevant local information on the deposit, such as, thermal conductivity under flowing conditions, temperature profiles within the deposit, deposit-liquid interface temperature, and deposit composition. The temporal and spatial evolution of the deposit layer were measured for different values of the laminar flow Reynolds number. Excellent agreement was obtained between measured values of the deposit thickness and predictions from a numerical model developed previously in our research group. Measurements of the evolution of the deposit-liquid interface temperature have shown that the interface temperature evolves from a value equal to the solution wax appearance temperature, WAT, to the wax disappearance temperature, WDT, as the deposit grows to attain its steady state thickness. The temperature traversing probe was employed to obtain information on the temperature profiles within the wax deposit layer under flowing conditions. A comparison of the measured temperature profiles within the deposit with the theoretical solutions, indicated the possibility of convective transport in the deposit. Measurements of the deposit thermal conductivity under flowing conditions did not reveal any effects of the imposed shear rate, for the range of Reynolds numbers investigated. Local variations of the thermal conductivity across the deposit layer indicated the presence of liquid close to the cold wall. Deposit samples were obtained and analyzed by high temperature gas chromatography, for the range of the laminar Reynolds numbers tested and for different durations of the deposition experiments. The analyzes revealed that the carbon distributions of the deposit samples presented a shift toward higher carbon numbers both, with increasing deposition time and Reynolds number,

characterizing the aging process of the deposit. The carbon number distributions were seen to display an asymptotic behavior with Reynolds number, for samples obtained from the final portion of the longer deposition lengths of the annular test section.



## Keywords

Wax deposition; Flow assurance; Interface temperature; Deposit thermal conductivity; Deposit aging;

## Resumo

Veiga, Helena Maria Borja; Azevedo, Luis Fernando Alzuguir. **Estudo de depósitos de parafina em dutos**. Rio de Janeiro, 2017. 190p. Tese de Doutorado — Departamento de Engenharia Mecânica, Pontifícia Universidade Católica do Rio de Janeiro.

O presente trabalho forneceu informações originais para auxiliar o entendimento dos fenômenos básicos que governam a deposição de parafina em dutos. O programa de pesquisa estudou questões relevantes, ainda em aberto na literatura, relacionadas à formação, crescimento e envelhecimento de depósitos de parafina. Com este objetivo, foi desenvolvido um programa experimental seguindo a estratégia de conduzir experimentos simples, empregando seções de teste em escala de laboratório, com condições de contorno e iniciais bem definidas, e empregando fluidos de teste simples e com propriedades conhecidas. As medidas foram realizadas em seções de testes retangular e anular, ambas especialmente projetadas para permitir medidas ópticas da evolução temporal e espacial da espessura dos depósitos. As seções de testes foram equipadas com um sensor de fluxo de calor, sondas de temperatura móveis e janelas para amostragem de depósitos, que permitiram a medição de grandezas importantes como, condutividade térmica do depósito sob condições de escoamento, perfis de temperatura dentro do depósito, evolução da temperatura da interface depósito-líquido, e composição do depósito. A variação espacial e temporal da espessura do depósito foi medida para diferentes valores do número de Reynolds laminar. Excelente concordância foi obtida entre os valores medidos e previsões de um modelo numérico desenvolvido previamente em nosso grupo de pesquisa. Medidas da evolução temporal da temperatura da interface depósito-líquido mostraram que a temperatura da interface evolui de um valor igual à temperatura inicial de aparecimento de cristais da solução, TIAC, até a temperatura de desaparecimento de cristais, TDC, a medida que o depósitos cresce até sua espessura de regime permanente. A sonda de temperatura foi utilizada na medição de perfis transversais de temperatura dentro do depósitos sob condições de escoamento. A comparação destes perfis com soluções teóricas apontaram para a possibilidade de ocorrência de escoamento dentro da matriz porosa do depósitos. As medições da condutividade térmica do depósitos sob condições de escoamento não apresentaram qualquer efeito da taxa de cisalhamento imposta, para a faixa de número de Reynolds investigada. Variações transversais da condutividade térmica do depósitos indicaram a presença de líquido próximo à parede fria. Amostras do depósitos foram obtidas e analisadas por cromatografia gasosa de alta temperatura para a faixa de número de Reynolds laminares investigadas, e para diferentes durações dos

experimentos de deposição. As análises indicaram que as distribuições de carbono das amostras de depósitos apresentaram um deslocamento em direção aos maiores números de carbono com o aumento do Reynolds e do tempo de deposição, caracterizando o processo de envelhecimento do depósito. As destribuições do número de carbono apresentaram um comportamento assintótico com o número de Reynolds, para amostras obtidas dos trechos finais dos comprimentos de deposição da seção de testes anular.



## Palavras–chave

Deposição de parafina; Garantia de escoamento; Temperatura da interface; Condutividade térmica do depósito; Envelhecimento do depósito;

# Contents

# List of figures

# List of tables

*Le mieux serait d'écrire les événements au jour le jour. Tenir un journal pour y voir clair. Ne pas laisser échapper les nuances, les petits faits, même s'ils n'ont l'air de rien, et surtout les classer. Il faut dire comment je vois cette table, la rue, les gens, mon paquet de tabac, puisque c'est cela qui a changé. Il faut déterminer exactement l'étendue et la nature de ce changement.*

**Jean Paul Sartre**, *La nausée.*

# 1
# Introduction

Wax deposition in pipelines is one of the most relevant problems faced by the industry in the task of assuring the continuous flow of petroleum. In subsea production, petroleum flows from the reservoirs at relatively high temperatures into the production lines. The crude is transported in these lines to the platforms or directly to shore. At the large water depths that are common in current offshore fields, the ocean temperature is of the order of $4^oC$. The solubility of the waxy components of the oil decreases with temperature. So, as the oil loses heat to the external cold environment, a critical temperature may be reached and trigger the precipitation of the heavier wax components. These components may deposit on the inner surface of the pipe, leading to increased pressure drop or, in extreme cases, to the total blockage of the line. Remediation costs for blocked pipelines located at large water depths can be of the order of millions of dollars per kilometer, and loss of revenues can be of the order of several million dollars a day, what may severely influence the profitability of a field. As an example, the Lasmo company had to abandon a Staffa Field platform in the North Sea due to wax deposition problems only four years after beginning production, at an estimated cost of more than one hundred million dollars, (Kang and andJ.Lim (2014)). In Brazil, the petroleum production in the pre-salt layer has renewed the interest on the wax deposition problem due to the high wax content found in the crude produced, and also due the relatively lower temperatures of the reservoirs.

The ability to predict whether wax deposition will occur in a certain pipeline installation is of fundamental importance for designers and operators. Indeed, advanced information on the probability of wax deposition and estimates of wax deposit spatial and temporal distributions can be used as input in the pipeline design phase, aiding in the specification of the proper amount of thermal insulation for the line, allowing for pigging, for the injection of chemicals or even for active heating of the line. These design decisions have direct impact on the cost of the installation. For the pipeline operator, the information of the temporal and spatial distribution of the deposit and its chemical composition will dictate the type of pig and frequency of passage to

be employed.

Wax deposition models are valuable tools to aid pipeline designers and operators. Due to the complexity of the wax deposition phenomena, most models available rely, to different degrees, on the use of empirical parameters and correction factors that tune the model to the data of a specific field. Although this procedure may yield relevant information to the particular field from which the data were collected, it does not allow the use of the tuned model to other fields with different characteristics, since the fundamental physics governing the deposition phenomena were not properly understood and modelled.

Wax deposition models have also been developed based on fundamental principles, considering several aspects of the phenomena, such as wax precipitation, crystallization kinetics, convective and diffusive heat and mass transport, and wax removal processes. The thermodynamic prediction of wax precipitation is the main component of a deposition model, and can be incorporated via experimentally determined solubility curves or through elaborated thermodynamic calculations with different levels of complexity.

Wax precipitation is a necessary but not sufficient condition for deposition to take place. Transport of dissolved paraffin and wax crystals will determine if the precipitated paraffin will be driven toward the pipe wall where it can form a solid deposit, or carried along by the flow without contributing to the deposit formation. The study of the mechanisms responsible for wax deposition has been the focus of several research groups along the years. Yet, a definitive understanding of the predominant deposition mechanism has not been achieved.

The present work is part of an ongoing research project aimed at contributing to a better understanding of the physical mechanisms governing the deposition of wax in pipelines. This research line has been pursued at the Fluids Engineering Laboratory of the Mechanical Engineering Department of PUC-Rio for more than a decade. The research work has followed the strategy of conducting simple experiments, employing test sections with well-defined geometries, boundary and initial conditions, and employing test fluids with known properties. The experiments were always sided by detailed numerical solutions, faithfully modelling the test conditions. The comparison between experiments and simulations offer excellent possibilities to test the relative importance of deposition mechanisms and the accuracy of thermodynamic, fluid flow, heat and mass transfer modelling.

A search in the open literature, and our own group past experience, has revealed that there are still several issues related to the understanding

and proper modelling of the wax deposition phenomena that demand further research. Based on this scenario, the present work focused attention on a few of those pending issues.

A completely new designed annular test section was constructed to perform the wax deposition studies that will be reported here. This design is considered a significant improvement over the past rectangular geometries, offering better thermal stability and control of boundary conditions and heat losses. The test section allowed for optical access to the interior of the deposition annular channel space, and included a port for deposit sampling and a traversing temperature probe capable of measuring temperature profiles in the liquid and in the interior of the wax deposit under flowing conditions. A second test section in the form of a rectangular channel was also constructed to conduct experiments on the characteristics of the wax deposits. This test section was equipped with a heat flux sensor and a traversing probe, and also allowed visual access to the interior of the channel. Sampling of the deposits was also possible in this rectangular test section.

A distinct feature of the present research is the care directed to the preparation and characterization of the test fluid employed in the experiments. The fluid was prepared from a pure, single-carbon-molecule solvent and a wax mixture displaying a narrow band of carbon molecules, distributed far from the solvent carbon number.

The experimental studies encompassed measurements of the transient spatial distribution of the wax deposits along the channel length for different values of the laminar channel Reynolds number. Temperature profiles in the liquid phase and within the deposit were obtained with the temperature traversing probe. Samples of the deposit were taken and analysed by gas chromatography and used to study deposit aging. The temperature probe was also employed to measure the deposit-liquid interface temperature during the transient deposit formation. The information obtained contributed to the discussion in the literature regarding the temperature of the interface being the wax appearance temperature, WAT. Measurements of the wax deposit thermal conductivity were performed for flowing conditions using the temperature probe and the heat flux sensor, a piece of information much needed for wax deposition simulation.

As part of the research strategy, numerical solutions of some of the tests conducted were obtained and compared with the experimental results. A numerical model previously developed in our research group was used for this purpose. This model solved the coupled equations governing the fluid flow, heat, mass and concentration fields, together with a multi-solid thermodynamic

model, yielding the spatial and temporal distributions of the components of the test mixture, as well as the deposit thickness, solid fraction, chemical composition, temperature and velocity fields.

This manuscript is divided into ten chapters. This large number of chapters is due to the decision to separate each part of the research conducted to facilitate the understanding, although an exchange of information among the chapters was inevitable.

Chapter 2 presents a brief, historically-oriented, survey of the literature on wax deposition. The more up-to-date and specific topics of the literature were included in the different chapters as needed to support the research conducted and described in these chapters.

Chapter 3 details the design and construction of the two test sections utilized in the studies, namely, the rectangular and the annular test sections.

Chapter 4 describes the properties and characteristics of the solutions employed in the tests.

Chapter 5 conveys the information on the temporal and spatial distributions of the wax deposits measured in the annular test section. A comparison with numerical predictions is also presented.

Chapter 6 is dedicated to the presentation and discussion of the results of the temperature profiles measured in the wax deposit. The issue of diffusion or convection controlling the heat and mass transfer within the deposit is addressed by the analysis of the measured temperature profiles.

Chapter 7 describes the results from the experimental studies conducted on the temperature of the deposit-liquid interface measured as the deposit was formed.

Chapter 8 presents the results for the composition of the deposit samples, relating it to the aging process of the deposit.

Chapter 9 presents and discuss the results obtained for the thermal conductivity of the wax deposit, measured under flowing conditions.

Finally, in Chapter 10, a summary of the main conclusions of the work developed are presented, together with suggestions for further studies.

# 2
# Literature Review

The present literature review is intended to give a brief historical overview of the works conducted in the field of study of wax deposition in pipelines. There are already available in the literature thorough reviews, such as those found in Azevedo and Teixeira (2003), Aiyejina et al. (2011), and in the book by Huang et al. (2015). The more up-to-date and specific topics from the literature related to the subjects treated in each different chapter of the present text are commented in those chapters.

Figure 2.2 shows a non-comprehensive compilation of the journal articles published in the area of wax deposition along the years. Up to the mid-90's there were few publications in the field, typically, one per year. By the end of the 90's a significant increase in the number of yearly publications is verified. That change can be linked to the year offshore production reached the mark of 700 meters of water depth, as can be seen in Figure 1.2 displaying the production records by Petrobras. Other companies in the petroleum industry presented similar production achievements. At this water depth, ocean temperature is constant at approximately $4^oC$, a temperature that can potentially cause severe wax deposition problems. Indeed, the field problems reported at that depth and beyond induced a research effort in the area that reflected in the articles production.

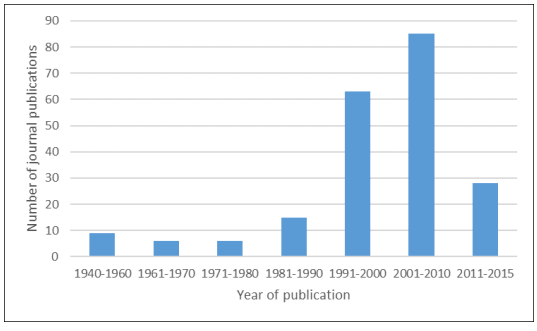


Figure 2.1: Number of journal publications in the field of wax deposition.

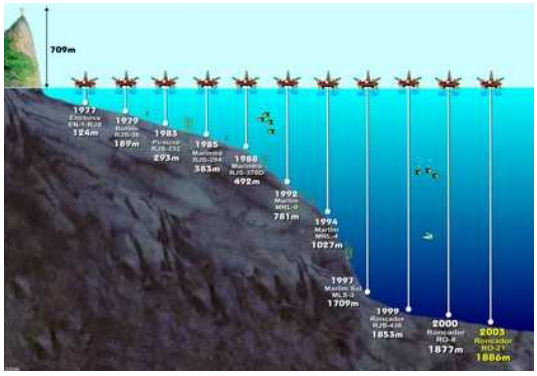


Figure 2.2: Water depth world records established by Petrobras in offshore production.

Problems related to the transport and storage of petroleum caused by wax deposition have been reported as early as 1928 Huang et al. (2015). In the 1940's one of the first patents related to wax deposition was deposited at the US Patent Office. It was related to what is known today as the cold flow technique. The inventor claimed that if the oil would be pumped at a temperature colder than the pipe wall temperature, even if that meant being under the wax appearance temperature (WAT), wax deposition would be retarded or even prevented. Another invention deposited at the US Patent Office, dating from 1942, dealt with a wax crystals modifier injected in the flow for wax deposition control. Neither one of these propositions became a viable product that completely prevented wax from depositing, as can be verified by the fact the topic is still, 80 years later, a current research area of interest.

The first systematic study on wax deposition reported in the literature is the work of Jessen and Howell (1958), where deposition on different metallic and plastic pipe materials was investigated for laminar and turbulent flow conditions. This pioneer work already mentioned several key issues regarding wax deposition in pipes, such as possible deposition mechanisms, hardening of the deposit with increased shear and cooling rates, shear removal of deposited wax, and affinity of the deposit to the pipe surface material. The study proposed that two competing mechanisms were responsible for wax deposition at the pipe wall. One mechanism was related to the diffusive transport of dissolved wax, while the other was based on the deposition of crystals in suspension. The authors stated that the diffusive mechanism is dominant, arguing that experiments with the waxy mixture inlet temperature above the wax appearance temperature, WAT, yielded much thicker deposits than those with the inlet fluid temperature well below the WAT and, therefore, containing wax crystals in suspension. This argument failed to consider the direction of the heat flux from the working fluid to the outside fluid environment, a decisive

factor for deposition to occur Cabanillas et al. (2016). From the description of the experiments conducted by Jessen and Howell it can be inferred that no proper control of the sign of the radial heat flux was maintained and that the experiments displaying suspended crystals were conducted with the working fluid at a lower temperature than the outside environment.

Hunt (1962) conducted adhesion tests of wax deposits to different types of surfaces. In his work, no deposition was verified when the bulk fluid temperature was the same as the wall temperature, what led the author to conclude that molecular diffusion of wax in solution is the controlling deposition mechanism.

Later the work of Patton (1970) investigated the influence of surface roughness on the rate of wax deposit removal from the surface of the pipe. Experimental work was undertaken in a cold-spot tester, similar to a cold-finger apparatus, which is a deposition apparatus used to perform stagnant deposition tests Kasumu and Mehrotra (2015); Correra et al. (2007). The study concluded that, besides the roughness of the surface, the composition of the wax could influence the rate of sloughing. The authors identified that wax composed mainly of low molecular weight normal paraffins would be removed from smooth surfaces much easier than from rough ones. However, high molecular weight waxes with significant amount of non-normal paraffins did not have its rate of removal influenced by surface roughness.

In the late 1970's, the research work was focused towards understanding the basic physical aspects of the wax deposition problem by relating the flow characteristics with the rate of deposition. Bott and Gudmundsson (1977) performed an experimental work on wax deposition using a kerosene and wax solution depositing onto cold pipe surfaces. The authors deduced the rate of wax deposition by measuring the changes on the overall heat transfer coefficient. Significant oscillations on the deposit thickness were reported and were associated with deposit removal from the deposit layers closer to the bulk flow region where a mushy region was observed. The authors also concluded that deposition would be controlled by the cohesive forces of the wax particles formed in the boundary layer and by the number of wax crystals available for deposition in the boundary layer what, at its turn, is dependent on the prevailing thermal and hydrodynamic conditions.

In the 80's there was a research effort directed to the proposition of the possible mechanisms responsible for wax deposition. Before commenting the work of Burger et al. (1981), which was, seemingly, the first to suggest models to incorporate these mechanisms, a brief description will be presented of the mechanisms proposed at that time associated to wax deposition. That

will facilitate the interpretation of some of the models developed along the years.

**Wax deposition by molecular diffusion** When a material containing two or more components with non-uniform composition a composition gradient emerges, generating a tendency of mass transfer leading to uniform composition, which is the basis of diffusion processes. Diffusion is caused by random molecular motion that leads to mixing. Burger et al. (1981) identified two forms of diffusion acting in the transport of waxes, the diffusion of dissolved wax and that of suspended wax crystals. The first caused by a concentration gradient in the oil and the other by a crystals concentration gradient. The molecular diffusion wax deposition mechanism consists of transport of wax in solution from the bulk of the fluid to a region close to the wall. Since the solubility of wax components decrease with temperature, at the colder regions close to the pipe wall wax components might precipitate decreasing the concentration of wax in the solution, provided the wall temperature is below the wax appearance temperature for the solution. Thus, a wax concentration gradient is formed between the solution at the warmer regions and that at the colder regions. This concentration gradient would drive the diffusion of wax toward de cold wall. Fick's law of diffusion is normally used to model this diffusive flux, where the flux is proportional to the concentration gradient. However, Creek et al. (1999) pointed out that the diffusion coefficient in Fick's law is appropriate for binary mixtures. In a multicomponent system it would be more appropriate to use the gradient of chemical potential. Creek et al. (1999) also pointed out that Fick's first law of diffusion describes an isothermal, quiescent process, and it may not be appropriate for wax deposition modelling. It is also common in the literature to find models that split the concentration gradient in a temperature gradient and a variation of the species concentration with temperature, taken from the solubility curve.

Again, criticism is found regarding the use of the chain rule for modelling molecular diffusion in wax deposition. As mentioned before, Fick's first law describes an isothermal quiescent process, the concentration gradient may not be equivalent to the temperature gradient as proposed. Also, the concentration of species is not a unique function of temperature, being a function of pressure and chemical composition. Therefore, discussion exists whether the splitting of the concentration gradient is suitable for modeling the diffusion flux (Hoteit et al. (2008), Creek et al. (1999)).

**Wax deposition by Brownian diffusion** The second type of diffuion identified by Burger et al. (1981) was the diffusion happening by the presence of a gradient of small wax crystals out of solution. Brownian diffusion of solid wax crystals out of solution is a possible mechanism to transport wax molecules to the wall and contribute to the deposit formation. Suspended particles will collide with thermally agitated fluid molecules giving rise to the irregular Brownian motion. In the presence of a concentration gradient of solid crystals, there will be a net transport of these crystals in the direction of decreasing concentration. A Fick's-type law can be used model this flux. In this case a Brownian diffusion coefficient is employed.

**Deposition by gravity settling** Suspended wax crystals could, in principle, settle in a gravitational field and contribute to deposit formation due to differences in the density from the crystals and that from the oil.

**Deposition by shear dispersion** Wax deposition by shear dispersion is a mechanism of cross-stream transport of crystal in suspension. Several studies on the flow of concentrated suspensions indicate that the lateral motion of particles immersed in a shear flow is in the direction of decreasing shear (Segrè and Silberberg (1962); Brenner (1966); Cox and Mason (1971); Ho and Leal (1974)). In a pipe flow, this would lead to motion of particles away from the pipe wall and, therefore not contribute to the deposit formation. Also, Segrè and Silberberg (1962) have shown that particles can migrate to an intermediate region between the pipe centreline and the wall.

Burger et al. (1981) discussed the relative importance of the deposition mechanisms, considering those mentioned above, i.e., gravity settling of wax crystals, molecular diffusion of dissolved wax, Brownian diffusion of wax crystals and shear dispersion of crystals. In their analysis, the contributions of gravity settling, Brownian diffusion and shear dispersion were considered negligible in the presence of molecular diffusion. Since then, the vast majority of the models developed and available in the open literature incorporate molecular diffusion as the only deposition mechanism. Predictions of molecular diffusion-based models were adjusted to available laboratory and field data by the tuning of physical properties. Azevedo and Teixeira (2003) have pointed out that this procedure is probably responsible for the dominance of the molecular diffusion mechanism over other transport mechanism in the available deposition models. In their work, Azevedo and Teixeira (2003) argued that, based on the available data at that time, there was no firm basis to rule out the contribution of particle transport mechanisms, such as Brownian diffusion, to the formation

of the deposited wax layer.

Weingarten and Euchner (1988) have conducted experiments in a test loop under controlled conditions. The tests measured the total deposition by the pressure differential method, and compared it with the expected contribution of molecular diffusion obtained from tests with a cell with stagnant fluid. By this procedure, the authors intended to separate the contributions from molecular diffusion and particle transport. For low shear rates, the deposition rate was greater than that predicted by molecular diffusion only, indicating that other deposition mechanisms could be present. For higher shear rates the deposit grew rapidly at first, approximating the expected diffusion rate, but then the rate began to decrease. At these flow rates, even in laminar conditions, waxes were sloughed when the wall shear stress exceeded the strength of the wax deposit.

Brown et al. (1993) conducted a deposition study based on the mass transfer equation proposed by Burger et al. (1981) to model molecular diffusion and shear dispersion mechanisms. To test the shear dispersion contribution, the flow loop was operated at constant inlet and wall temperatures, for different shear rates. As per Burger's equation, deposition should linearly increase with shear rate, what was not verified. Also, experiments were conducted for the same bulk and wall temperatures presenting no deposition. Based on these findings, the authors concluded that shear dispersion of wax crystals was not contributing to the deposit formation.

Hamouda and Davidsen (1995) conducted experiments in a pipe section divided into three sectors. In the first sector the pipe wall was cooled, while in the second sector the wall was insulated. In the third sector the wall was again cooled. They observed deposition in the first sector, almost no deposition along the insulated pipe sector, and deposition again in the cooled third sector. They concluded that deposition mechanisms based on lateral motion of crystal, such as shear dispersion or Brownian motion, are not relevant, otherwise there would be deposition in the second sector. The authors suggest that sloughing takes place at high shear rates, making it impossible for wax to deposit at the wall.

Creek et al. (1999) did deposition experiments in a flow loop and measured the rate of deposition by means of 5 different techniques. The rate of deposition was shown to be inversely proportional to the flow rate . The initial oil temperature of the system did not alter significantly the steady state thickness of the deposit. It was shown, however, that a greater difference between the oil and the wall temperature produced thicker and softer deposits. Additionally, the deposits were analysed chemically by gas chromatography

at the end of the runs. The results have shown that deposits became more concentrated in the heavy paraffin species with time. It was also found that deposits generated under turbulent flow tests presented significantly more high molecular weight molecules.

A relevant contribution to the understanding of the wax deposition process was made by Singh et al. (2000). They conducted a study on thin wax-oil gels formed at the initial stages of the deposition process. After the initial gel formation, wax molecules continued to diffuse into the gel, increasing its wax content, what is known as the aging of the deposit. Experiments with model oils were performed including the analysis of the changes in deposit composition with time. The authors concluded that the aging of the deposit is a counter diffusive process with a critical carbon number above which wax molecules diffuse into the gel deposit and below which oil molecules diffuse out of the deposit. A mathematical model was developed based on conservation laws and a molecular diffusion deposition mechanism. A solubility curve was used to yield the concentration at the deposit interface. The model was able to predict the rate of the deposit growth and the deposit solid/liquid content. The model required adjusting parameters that were based on the expected aspect ratios of wax crystals.

Bidmus and Mehrotra (2004) and Bhat and Mehrotra (2005) proposed that the wax deposition problem was controlled solely by heat transfer, being modelled as a phase-change, moving-boundary problem. They obtained good agreement with batch experiments. They also performed measurements of the deposit–liquid interface temperature and reported that it evolved at a temperature equal to the WAT of the solution.

Merino-Garcia et al. (2007) stated that the common practice of using fitting parameters to tune models to field data can hide errors associated with the development of models that incorporate incorrect physical mechanisms. The model proposed by Merino-Garcia et al. (2007) was based on gelation and axial transport of waxes. The work suggests that deposition basically occurs by the gelation of wax axially transported into the deposit-liquid interface. Indeed, Merino-Garcia et al. (2007) presented arguments that indicate that radial diffusion rates are much smaller than axial convection rates. Moreover Merino-Garcia et al. (2007) raises questions addressing the deposit-liquid interface conditions. The authors suggest that further investigation was necessary in order to determine the conditions at which deposits ceases to grow. They raised the question whether it is the shear at the interface that precluded further deposition, or it is a matter of the interface temperature reaching the WAT and ceasing the deposit formation.

Banki et al. (2008) proposed a model that treated the liquid region and the deposit as an integrated computational domain without interfaces. The velocity and pressure fields were calculated from the Navier-Stokes equation in the liquid region and from a combined Darcy-type equation and the Navier-Stokes equation in the gel region. The gel region was treated as a porous medium filled with liquid. A source term dependent on the solid–liquid fraction automatically controlled the relative importance of the terms in the Navier-Stokes transforming it into a Darcy-type equation as the solid fraction increased. The energy and concentration transport equations were also solved. The Lira-Galeana et al. (1996) thermodynamic model was used for solid–liquid split calculation. The species concetration fields were determined by convection, molecular diffusion and Soret thermal diffusion. Convection in the porous gel layer was also considered. The deposit thickness was determined as the region in the computational domain where the solid fraction was greater than 2%, a number obtained from experiments reported in the literature by Holder and Winkler (1965) in 1965 and confirmed later by Singh and Fogler (1999). The model was able to produce relevant information regarding deposit composition, solid fraction and thickness, besides velocity, and temperature fields.

Hoffmann and L.Amundsen (2010) did single phase experiments in a flow loop and measured the deposit thickness by means of three methods, including the recently proposed laser based technique. The experimental study explored the effect of three different parameter on wax deposition rates, bulk-to-wall temperature, coolant temperature and the flow rate. The rate of deposition was shown to be directly proportinal to the wax solubility curve when varying the wall temperature and maintaining constant bulk-to-wall difference. For constant coolant temperature, varying the flow rate, the rate of deposition was found not to follow the dissolved wax concentration gradient, driving force for diffusion–based models, specially at higher flow rate. The authors argued that the pure diffusion-based models alone may not be appropriated to describe wax deposition when significant wall shear effects are present. Later, R.Hoffmann et al. (2012) did water–oil stratified flow experiments of wax deposition. The results showed that higher flow rates and lower water cuts induced thinner deposits, richer in heavy components. The authors concluded that in these conditions deposition is dominated by diffusion since gelation is limited to low shear rates.

An interesting finding made by Hoffmann and L.Amundsen (2010) was that the deposits got richer in heavier components with the temperature level, for constant bulk-to-wall temperature. The authors associated that phenomena

with bulk precipitation of heavy components in the lower temperature cases, leaving only lighter components available for deposition by diffusion. Moreover, some comments were made concerning the effects of sloughing at temperature levels close to the WAT.

Huang et al. (2011) developed a model to predict the deposit thickness and solid fraction variation solving the governing equations for momentum, temperature and concentration, for laminar and turbulent flows. They analysed the different approaches to treat wax precipitation, namely, no precipitation of wax in the bulk and instantaneous precipitation. The analysis demonstrated that these approaches form, respectively the upper and lower limits of the deposition rate, thereby over or under-predicting the deposit thickness. In the authors view, there is a region adjacent to the deposit-liquid interface, colder than the WAT, where solid out of solution exist but are not allowed to deposit by the prevailing flow conditions. The authors proposed the use of a precipitation constant to account for the kinetics of wax precipitation imposed by the flow. By properly adjusting this constant, excellent agreement was obtained with laboratory and field data.

The issue of the contribution of the wax precipitated in the bulk of the flow seems to remain unresolved. Usually a simplified approach with respect to the solid existing out of the solid-liquid interface is taken. Either the solid disappears from the calculation domain(Venkatesan and Fogler (2004)), or it is kept fixed at zero velocity (Banki et al. (2008)). No model in the literature was found where the transport of solids is considered. Solids in suspension may alter the apparent viscosity of the solution influencing the velocity field. Also, solids can be transported to regions close to the interface where they can accumulate as shown in the videos of Cabanillas et al. (2016). Precipitated solids can also be transported to regions where the thermodynamic conditions are such that they can be re-dissolved in the solution. This issue deserves further study.

Another issue that still needs further study is related to the time evolution of the deposit–liquid interface temperature. Different research groups treat the interface temperature differently. Models proposed in the literature consider the interface temperature evolves up to a value equal to the WAT when the deposit stops growing. Evidences indicate that the thermodynamic phase change temperature, or the liquidus temperature, is the correct limiting temperature for the interface growth (Bhat and Mehrotra (2004)).

The time evolution of the deposit solid fraction and composition, the aging process, has received attention in the literature. As already mentioned, some authors have suggested that deposits become richer in high molecular weight components with both time and the Reynolds number Creek et al.

(1999); Singh et al. (2000); Banki et al. (2008); Hoffmann and L.Amundsen (2010); R.Hoffmann et al. (2012). However, the explanation to that phenomenon is far from being a consensus.

Bhat and Mehrotra (2008) modelled the aging process as a shear stress based mechanism, where the squeeze of the deposit induced by shear would force the liberation of liquid. The effect of long term shear would be the hardening of the deposit layer. The parameter of adjustment of the numerical data is the tilt caused by shear over the deposit. Singh et al. (2000) however have suggested that a stress mechanism shouldn't be responsible for the aging since experimental data show that aging stops once the temperature gradient across the deposit is reduced. Moreover, Singh et al. (2000) showed experimental results where lower wall temperature caused higher wax content at the deposit, for the same flow rate.

Singh et al. (2001b) has interpreted the aging process in terms of diffusion. For the authors paraffin molecules below the critical carbon number diffuse out of the deposit, while those above it diffuse into the deposit through a counter-diffusion process. It was pointed out that the aging is a strong function of the temperature difference across the deposit, what would indicated a diffusion controlled process.

Other authors have associated the aging process with re-cristalization phenomena (Creek et al. (1999); Silva and Coutinho (2004); da Silva and Coutinho (2007)). In particular Silva and Coutinho (2004) has shown that the enrichment is not a heat induced process. The authors found that aging occurs even for isothermal conditions. They reported enlargement of the x-ray diffraction peaks what indicates increase in the size of the wax crystals. Silva and Coutinho (2004) proposed that a mechanism analogous to Ostwald Ripening could be taking place. Ostwald Ripening is related to a self-organization of molecules caused by excess free energy at the surface of particles, thus it is not a thermally induced mechanism. The authors also suggested that re-crystallization could be an aging mechanism. Recrystallization or secondary crystallization is frequently associated to effects that increase the crystallizing after a first nucleation.

An overview of the extensive body of literature available on wax deposition, of which the present text represents just a brief review, allows one to propose a description of a possible scenario and governing equations for the deposition process.

The momentum equations with appropriate constitutive relations, together with the energy and species concentration equations yield the velocity, pressure, temperature and concentration fields. A thermodynamic model can

then be used to predict the local solid and liquid fractions of each species composing the flowing solution. In the concentration conservation equations both the convective and diffusive terms seem to be relevant to determine the concentration field of each species. Other mechanisms such as, for instance, thermal diffusion could also be relevant and, in that case should be incorporated in the conservation equations. This however, seems to still be an area of current research where no consensus has yet been achieved in the literature.

Once the distribution of solid fraction has been determined, the next issue to be addressed is whether the solids will be driven by the flow or form a fixed, gel-like structure that constitutes the deposit. The relationship of the local solid content and the rheological properties of the gel layer seem to be a key issue deserving further research. The rheological properties of the solution and the gel should affect the velocity field and strongly couple the governing equations. The proper understanding of the gel formation and behaviour will allow one to properly define the deposit layer and replace the empirical information that is used today to define the deposit, as, for instance, the widely used figure of 2% of solids necessary to form a deposit.

The transport by the flow of the solids out of solution that did not form a fixed deposit is another issue that deserves further attention. Solids can be transported to regions where they can be re-incorporated into the solution altering the bulk composition field of the solution. This solid transport may require additional conservation equations that will add to the complexity of the problem.

The scenario just described involves heavy calculations and assumes that properties of the solution components as well as thermophysical properties of the deposit are well known, what it is not always the case. Much research is needed in this field.

Even if one assumes that properties are known, the required heavy calculations might be appropriate for fundamental investigations of the problem, but might not be appropriate to solve field problems where long pipelines and complex mixtures are the usual case. Indeed, there is much needed research in simplified models that capture the essence of the deposition physics without having to solve a complete set of complex, non-linear governing equations. Deposition models that use only diffusion fluxes at the interface, calculated with solubility curves, purely heat-transfer-based-models, rheological gel formation models, among others, should be confronted with the more complete models and with high quality laboratory experiments with the aim of establishing its predicting capabilities and ranges of validity.

The present research aims at contributing to the effort of understand-

ing the underlying physical mechanism of wax deposition by addressing some open issues related to the deposit formation. The work strategy was to conduct simple experiments with low uncertainty level and well defined boundary conditions to form a set of reliable pieces of information aiming to be used in comparison to numerical data. Though based on this general approach, some more specific issues will be addressed by the present work:

- What are the heat transfer mechanism inside the deposit layer ?
- What is the criteria for the formation of an immobile deposit layer ?
- Can aging be captured by measurements of the deposit thermal conductivity ?

# 3
# The experimental apparatus

The wax deposition experiments conducted were performed employing the two different flow loops that will be described in the present chapter. The first loop employed a rectangular test section of dimensions 150 x 40 x 12 mm (length x width x height). This test section was employed in the studies of the deposit–liquid interface temperature, temperature profiles inside the deposit layer, wax deposit composition analyses and deposits thermal conductivity. The second flow loop utilized an annular test section made from two concentric pipes with dimensions 1050 x 34 x 19 mm (length x external diameter x internal diameter). This second flow loop was used to perform experiments on the temporal and spatial growth of wax deposits, to conduct measurements of the deposit–liquid interface temperature, of temperature profiles inside the deposit layer, and to conduct studies of the wax deposits composition. In both cases, the experiments were conducted using a test solution formed by dodecane as the solvent and a special blend of paraffin compounds obtained by distillation in a Gas-to-Liquid operation. The properties of the test solution will be described in Chapter 4.



## 3.1
## Description of the rectangular test section apparatus

### 3.1.1
### General description of experimental setup

A general view of the rectangular experimental apparatus is exhibited in Figure 3.1. The main component is the rectangular test section where wax deposition took place. The test solution was kept in a stainless steel cylindrical tank and maintained at controlled temperature by the heating plate mounted under the tank. A volumetric pump circulated the test solution from the tank, through the test section and back to the tank in a closed circuit. All the lines carrying the test solution were thermally insulated and equipped with heat tracing tapes to maintain the solution temperature at the tank and avoid unwanted wax deposition within the lines. The volumetric pump was also thermally insulated and heated by heating tracer tapes. A PID system

coupled to a solid state relay controlled the energy input to the tracer tapes in order to maintain the temperature of the test fluid at the desired value for the experiments. Two water circulating units, a water bath and a chiller, where employed to set the surface of the test section at the desired temperatures for the wax depositions experiments. One of the baths was maintained at a higher temperature, typically $38^oC$, while the other was maintained at the lower temperature, typically $12^o$. A set of valves was provided so as to allow for the rapid control of the direction of the hot and cold water streams, in order to produce the desired thermal boundary conditions to promote wax deposition. Warm air jets impinging on the test section side walls (not shown in the picture) were provided to avoid unwanted wax deposition on these walls, what, otherwise, would have blocked the visualization of the interior of the channel. A Plexiglas rectangular box covering the test section (not shown in the figure) was used to isolate the test section from the laboratory temperature fluctuations. The components of the experimental apparatus will next be described in more details.



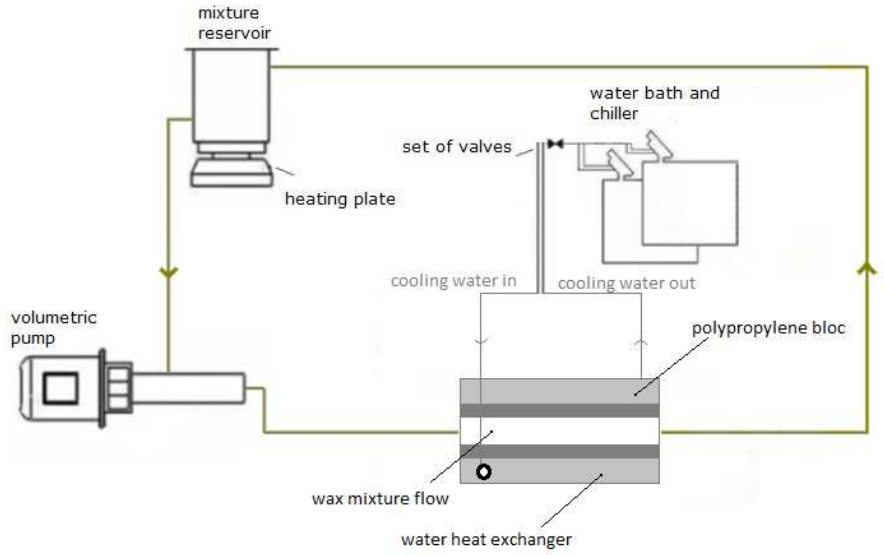


Figure 3.1: Rectangular geometry flow circuit.

### 3.1.2 The test section

A schematic side view of the rectangular test section is presented in Figure 3.2. The rectangular geometry was formed by two main parallel walls with dimensions of 150 x 40 mm (length x width) separated by a 12-mm-thick Plexiglas spacer. The bottom wall was made of stainless steel. The top wall

was made of polypropylene and supported the temperature traversing probe. As seen in the figure, the test solution coming from the pump entered the channel through the Plexiglas spacer right transverse wall, leaving it through the left transverse spacer wall. The bottom stainless steel wall was mounted on a polypropylene heat exchanger. When cold water from the water circulating units was pumped through this heat exchanger, wax deposits formed on the inner surface of the stainless steel wall. The bottom stainless steel wall was instrumented with two thermocouples and one heat flux sensor. The top and bottom walls of the test section are described next.

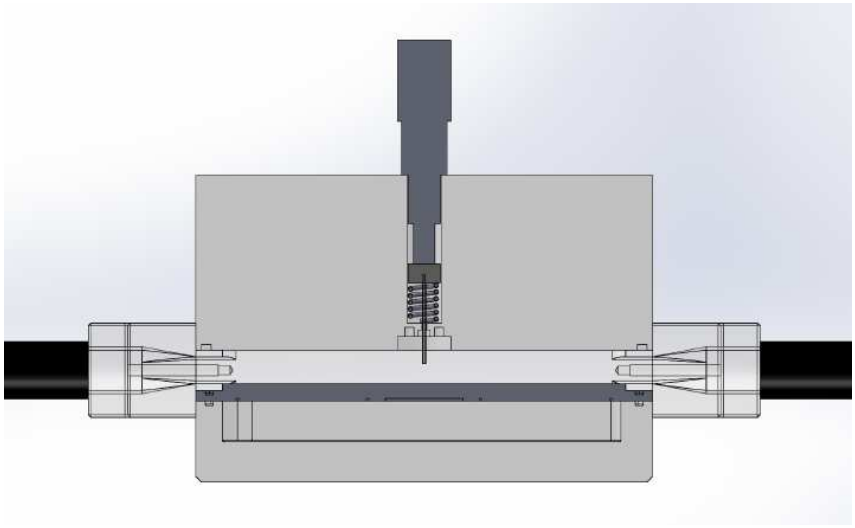

Figure 3.2: Longitudinal view of the rectangular test section.



### The bottom stainless steel wall

The bottom wall of the test section was composed of a stainless steel plate mounted over a water heat exchanger. The water heat exchanger was made of polypropylene, due to its thermal insulation properties. The back part of the stainless steel bottom plate with dimensions of 165 x 65 x 5 mm is illustrated in Figure 3.3. The plate was instrumented with two 0.125-mm-diameter, chromel-constantan thermocouples. The thermocouples were positioned at 0.5 mm from the inner surface of the wall, installed in 1-mm-diameter holes drilled through the back surface of the plate. Thermally conductive resin was used to fix the thermocouples in place.

A heat flux sensor, model Omega-HFS-4, was also installed on the back surface of the plate. A 28 x 35 x 0.2 mm square cavity was machined in the back surface of the plate to house the sensor, as it can be seen in Figure 3.3. Special care was taken in order to minimize errors in the reading of the heat flux by the sensor.

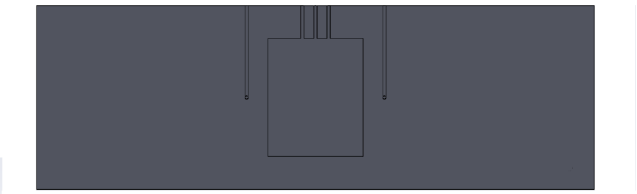

Figure 3.3: Stainless steel plate.

The heat flux sensor is made from an thermally insulating material, presenting a thermal resistance per unit area, of the order $0.0004^{K}m^2/W$. This value is 40 times the thermal resistance of the same thickness of stainless steel. The heat flux having to cross these two different thermal resistances in parallel, will be deviated to the path of less resistance, resulting in an error in the heat flux measured by the sensor. To minimize this deviation of the heat flux, an additional thermal resistance was installed on the back of the stainless steel plate. A 0.5-mm-thick sheet of polyethylene covering the back side of the stainless steel plate was employed for this purpose. Polyethylene presents a thermal conductivity similar to that of the material of the sensor. The sensor was placed at the bottom of the cavity and fixed in position with a layer of thermally conductive resin. On top of the resin, a stainless steel plate completed the cavity. With these layers in place, the heat flux path through the sensor area and outside the sensor area experienced similar thermal resistances, what avoided the distortion of the readings from the sensors. The assembly just described can be better visualized with the aid of Figure 3.4. It should be mentioned that the effectiveness of the thermal compensation proposed and just described was verified by calibration tests conducted by Pimentel (2013). In that work, a similar plate assembly containing a heat flux sensor was placed over a surface producing a known heat flux. The reading of the heat flux sensor embedded in the thermally compensated stainless steel plate agreed with the standard value of the calibration heat flux within the expected uncertainty level, of the order of 3%.

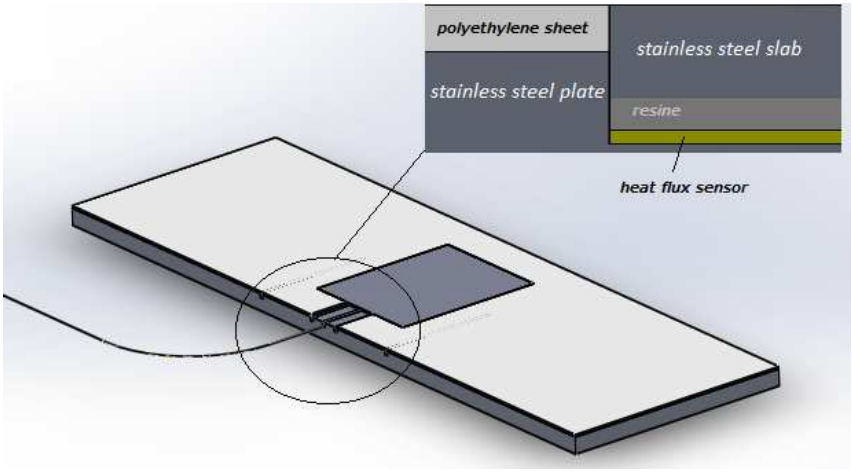


Figure 3.4: Heat flux sensor mounting at the back of the stainless steal plate.

### The top polypropylene wall

The top part of the test section exhibited in Figure 3.2 is a polypropylene block of dimensions 60 x 150 x 45 mm. This block contained a 13-mm-diameter hole in which a thermocouple traversing probe was mounted. This probe consisted of a micrometer head that displaced a disc connected to a thermocouple junction. The rod of the micrometer head when turned clockwise displaced the junction down while deforming a spring. When turned anticlockwise, the rod relaxed the spring that pushed the thermocouple junction up without any backlash. The hole for the traverse probe was drilled not at the center line of the channel, in order to facilitate the visualization of the thermocouple junction through the lateral wall, as indicated in Figure 3.5.

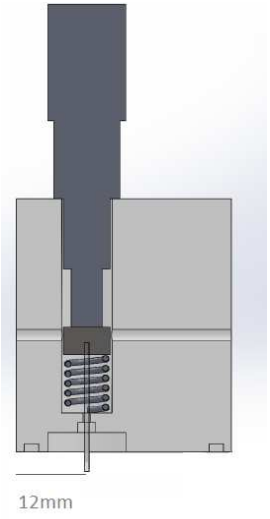


Figure 3.5: Side view of the top part of the rectangular test section.

A detail of the thermocouple junction assembly is shown in Figure

3.6. The thermocouple was made by welding two 0.076-mm-diameter wires of chromel and constantan. The final diameter of the junction after welding was approximately 0.2 mm. The wires were inserted inside a glass needle of 1 mm external diameter. The glass material was chosen to minimize heat conduction from the flow by the tip of the probe.

The location of the zero position of the thermocouple probe representing the bottom stainless steel plate was determined by the following procedure. A wire connected to the stainless steel plate was connected to an ohm meter. One of the wires of the thermocouple probe was also connected to the ohm meter. The probe was carefully lowered toward the stainless steel wall while the reading of the ohm meter was monitored. When the junction touched the stainless steel wall a short circuit was formed and detected by the ohm meter. The reading of the micrometer head was taken as the wall position. The uncertainty associated with this zero positioning procedure was of the order of 0.01 mm.

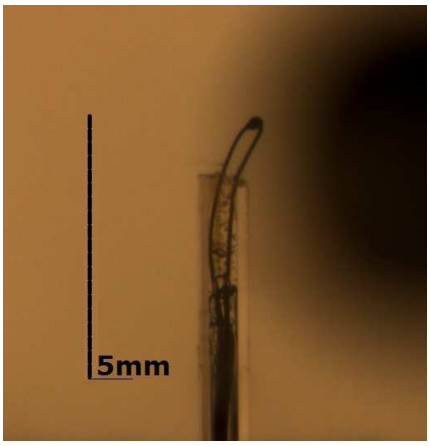


Figure 3.6: The thermocouple probe.



### 3.1.3 Stainless steel tank

The cylindrical stainless steel tank with internal dimensions 220 x 155 mm (height x diameter) is illustrated in Figure 3.7. The tank capacity was of approximately 4.2 L and it was operating very close to its full capacity, at around 4l. During the present experiments the highest wax depletion due to deposition was of 2.6 % of the total wax in solution, which rendered a final wax fraction of 19.6%.

The tank was positioned over a heated plate and wrapped with wool insulation. The heated plate has a magnetic agitator function, so that the fluid was constantly mixed inside the tank. A thermocouple probe was inserted inside the tank to control the mixture temperature.

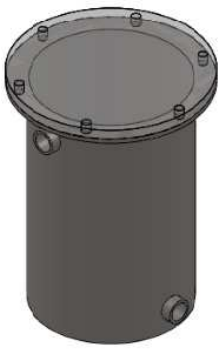

Figure 3.7: Stainless steel cylindrical tank.

### 3.1.4 The volumetric pump

A Netzsch NEMO021 volumetric pump was used to circulate the mixture from the reservoir into the test section. The volumetric pump was wrapped with heating tracer tapes and wool insulation to avoid formation of solid crystals in its cavities. At the outlet of the pump there was a valve that allowed the draining of the test section.

The pump flow rate was controlled by a frequency inverter. The maximum flow rate given by the pump was $0.94 m^3/h$. The calibration of the volumetric pump was performed using a solution of spindle oil with kerosene that matched the viscosity of the wax mixture solution employed in the tests at $40^oC$. The calibration was performed at $40^oC$ and the resulting curve is shown in Figure 3.8. The uncertainty for the calibration procedure was of the order of $\pm$ 3%.

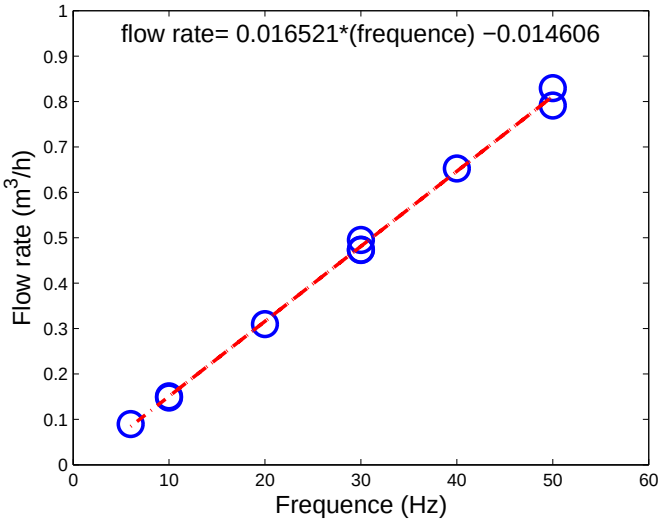


Figure 3.8: Calibration results for the pump used in the rectangular test section apparatus.



### 3.1.5 Heated air jets

Previous flow loop experiments based on visualizations in rectangular geometries have shown that heat transfer between the cold wall and the visualization wall can cause unwanted wax formation over the visualization wall (Cabanillas et al. (2016), Veiga et al. (2012)). In order to avoid this wax formation, a heated air jet was used to maintain the internal wall of the Plexiglass spacer at a temperature over the WAT. Ambient air was driven by a blower through a 50-mm-diameter cylinder equipped with electrical resistances. The heated air was then driven through a tee connected to two jet exits. Each jet was directed to one side of the Plexiglass walls, producing a controlled heating of the frontal and back Plexiglass surfaces. The jets were positioned at a distance of 10 mm from the Plexiglass surface. The air flow rate to the cylinder was adjustable. The electrical resistances were controlled by a voltage regulator with maximum capacity of 1 kW. The resistances were regulated to around 0.2 kW. Two fine gauge thermocouples were installed on the external surface of the Plexiglass spacer wall, with the surface exposed to the air jets. The temperature of the external surface of the Plexiglass spacer was maintained at 40 $^{\circ}C \pm$ 2 $^{\circ}C$.

### 3.1.6
### The polypropylene heat exchanger

Two water temperature controllers were used to control the temperature of the heat exchanger on the bottom part of the test section. A Huber C410 bath circulator, with 15 L volume capacity was used at temperatures higher than the fluid WAT (34.5 $°C$). A M75 chiller from Thermo-Haake was used for colder temperatures. A system of valves was mounted next to the two bath circulator, in a way that the circulation to the heat exchanger could be changed from one equipment to the other just by setting the valves. The chosen cooling ramp was the faster possible with the existing equipment.

### 3.1.7
### The data acquisition system

The data acquisition system employed was an Agilent 34970A with a USB interface used to transfer the data to a Labview software. The data acquisition was used with a 20-channel module, yielding a data rate of 60 channels per second. The module has a thermocouple internal reference. The internal reference was used to read some of the thermocouple information, as for example, the tank and the ambient temperature data. In the case of the plate and the entrance temperatures, an external reference was used. The external reference probe was maintained at zero temperature, inside an ice bath.



## 3.2
## Description of the annular test section apparatus

### 3.2.1
### General description of the experimental setup

A general view of the annular experimental apparatus is exhibited in Figure 3.9. Deposition takes place in the 1-m-long annular test section formed by two concentric pipes, the inner one a copper pipe, and the outer a transparent Plexiglas pipe. The test solution was maintained at controlled temperature in a 30-L stainless steel cylindrical reservoir. A volumetric pump circulated the test fluid from the reservoir, through a filter, through the annular test section, and back to the tank in a closed circuit. The lines carrying the test solution and the pump body were covered with electrical heated tracer tapes and thermal insulation to avoid wax deposition in the lines. A PID system coupled to a solid state relay controlled the heating power to the heated tapes.

Cold or hot water from two circulating baths could alternatively be pumped through the inner copper pipe. Hot water was used to attain a steady state condition prior to the initiation of the deposition tests. Cold water was pumped to initiate the wax deposition process on the outer surface of the inner copper pipe. A set of valves allowed the rapid change from hot to cold water flow in the copper pipe, in order to produce a rapid cooling of the inner wall. The annular test section was immersed in a water tank with its temperature controlled by a circulating unit. This arrangement decoupled the test section from temperature fluctuations of the laboratory space. Thermocouples connected to a data acquisition system measured the temperatures over the external wall of the inner copper pipe, and at the inlet and outlet planes of the test section. A detailed description of the experimental apparatus is given in the following sections.

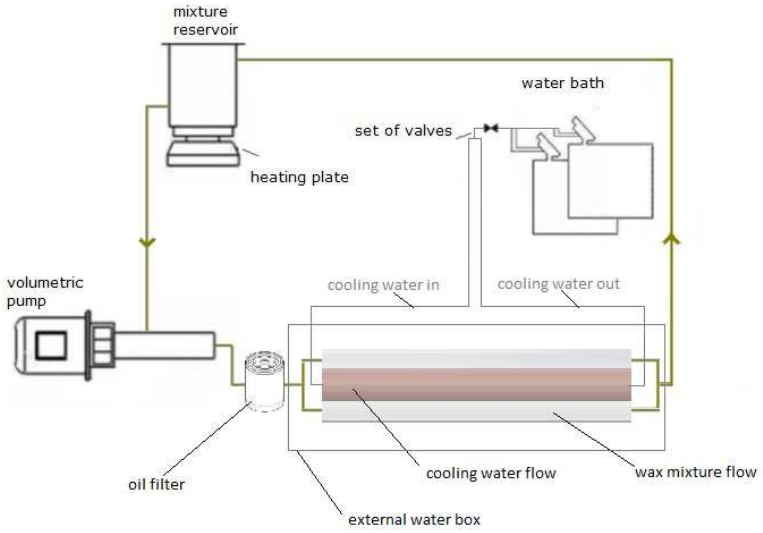


Figure 3.9: Schematic view of the annular test section apparatus.

### 3.2.2 The test section

The annular test section is illustrated in Figure 3.10. The geometry consisted of an internal copper tube, mounted concentrically to a Plexiglass pipe, forming an annular space with 1050 mm of length available for deposition. The internal copper tube had 19 mm of external diameter, while the Plexiglas pipe had 34 mm of internal diameter, thereby forming an annular gap of 7.5 mm. The detail in Figure 3.10 illustrates the annular test section with a wax deposit formed around the inner copper pipe.

A specially designed polypropylene piece was installed at each edge of the test section. These pieces served a dual purpose. They were responsible for holding the two pipes concentrically and also served to duct the test solution and the cooling water, respectively, to the annular space and to the interior of the copper tube. These pieces will be detailed shortly.

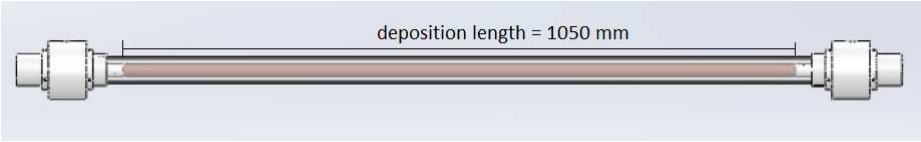


3.10(a):

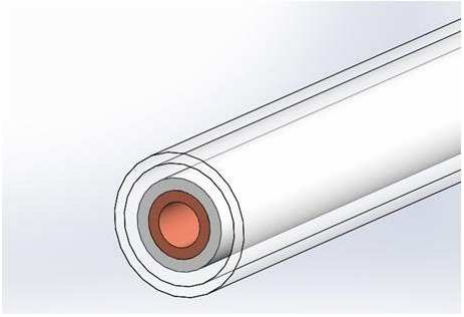

3.10(b):

Figure 3.10: Annular test section geometry (a) front view and (b) cut view.



### The copper tube

The inner copper tube had 19 mm of external diameter and 3.5 mm of wall thickness. Eleven chromel/constantan thermocouples were distributed along its axial length to sense the temperature variation along the length of the deposition surface. As will be seen in the presentation of the results, this is a relevant piece of information for the numerical simulation of the wax deposition process. Figure 3.11 illustrates a transversal cut of the copper tube. In that figure it is possible to see a copper plug insert where a thermocouple junction was installed. The junction was positioned at 0.5-mm from the copper plug surface and fixed in position using thermally conductive resin. The plugs were machined slightly oversized and pressed into holes drilled radially through the copper pipe wall. The tight fit obtained between the plug and the pipe wall guaranteed a good thermal contact. The wires of the thermocouples were guided through the interior of the copper pipe and exited through a water-tight connector. After all plugs were press-fitted into the copper pipe wall, the copper pipe was taken to a lathe where a machining operation removed approximately 0.2-mm of the pipe diameter. With this operation, the protruding tips of the copper plugs were removed and the resulting external surface of the copper tube was smooth, ready to serve as a wax deposition wall. After this successful

machining operation, the copper plug could hardly be seen on the external pipe surface.

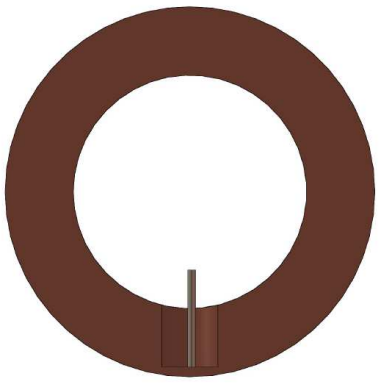

Figure 3.11: Cross sectional view of the cooper pipe. Detail of the thermocouple junction installed in the copper plug.

### The Plexiglass pipe

The external pipe forming the annular section is illustrated in Figure 3.12. It was made of transparent Plexiglas with a length of 1100 mm. Plexiglas was chosen for its transparency, permitting the visualization of the wax deposit layer formed over the inner copper tube. The cross section dimensions of the pipe were 34 mm of internal diameter and 3 mm of wall thickness. There were 4 ports installed on the external wall of the pipe. The two ports at the inlet and outlet of the test section allowed the insertion of thermocouple probes for measuring the bulk temperature of the test solution. The two ports at the central region of the pipe, at 0.70 and 0.80 of the test section length, measured from the fluid inlet plane, were provided to be used as a sample collecting port and as a thermocouple probe port, respectively.

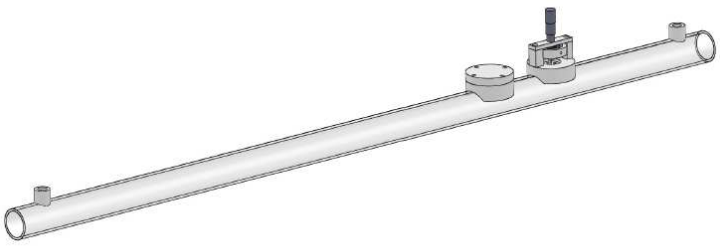

Figure 3.12: Plexiglass external pipe.

Details of the central ports are exhibited in Figure 3.13. The sampling port was made of PVC and it is the first seen on the left side of Figure 3.13.

That port was composed by a support and a cap. The support had 60 mm of external diameter and a 28-mm internal hole. The cap had a tight fit to the support. The internal edge of the cap was machined so as to present the same curvature as that of the internal Plexiglas pipe, so that, once inserted into position, it perfectly matted with the internal pipe curvature, without offering any steps that could disturb the flow of the test solution in the annular space.

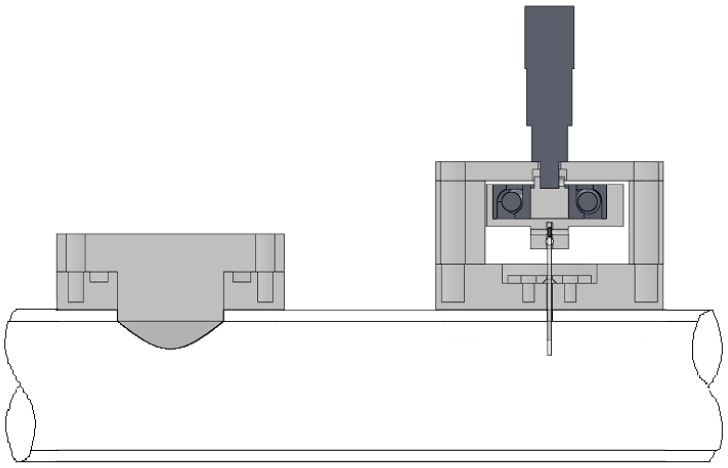

Figure 3.13: Coupling at the Plexiglass pipe.

On the right side of Figure 3.13 it is exhibited the thermocouple traversing probe port. It was composed by a support fixed to the pipe, two polypropylene pillars, a micrometer head and a sliding apparatus connected to a fine-gauge thermocouple probe. The two polypropylene pillars were threaded to the top part of the fixed support. They sustained the micrometer head by means of a rectangular support. When the barrel of the micrometer head was turned clockwise it pushed the sliding apparatus attached to the thermocouple probe and the probe penetrated into the annular space. When the rod was turned anti-clockwise, the thermocouple probe retreated without any detectable backlash. The maximum displacement of the probe was equal to 10 mm which was enough to span the 7.5-mm gap of the annular space.

The thermocouple port illustrated in Figure 3.13 contained an one-roll sealed bearing. The bearing function was to permit a purely vertical movement of the hollow glass tube that supported the thermocouple junction, avoiding that the thermocouple wires turned and broke. When the micrometer head was turned, the internal part of the bearing turned together with it, but not its external part. So, only the vertical movement of the micrometer head was transmitted to the glass tube.

The junction of the fine thermocouple probe has approximately 0.2 mm in diameter. The thermocouple was made by welding two 0.076-mm-diameter

chromel and constantan wires. The wires were inserted and glued into the 1-mm-external-diameter glass hollow tube. The wires together with the tube were fixed to a small polypropylene cylinder attached to the external part of the bearing.

As commented before, the thermocouple probe spanned the gap between the copper tube and the Plexiglass pipe. The zero position of the probe was assigned to the external wall of the inner copper pipe, and it was determined using a procedure similar to that used for the rectangular test section and described before. The electrical resistance of a circuit formed by a wire connected to the copper pipe and to the thermocouple was measured by an ohm meter. When the thermocouple junction touched the copper wall a short circuit was formed and detected by the ohm meter. The zero position of the thermocouple probe was detected with an uncertainty of $\pm 0.01$ mm.

### The water and test fluid distributor

A cross section view of the polypropylene pieces installed at the entrance and exit planes of the annular test section is illustrated in Figure 3.14. As already mentioned, these pieces had the function of holding the inner and outer pipes in a concentric position, and also to distribute the test solution and the cooling water. The distributor was composed of a 163-mm-long central part of and a 78-mm-long outside ring. The copper pipe matted the inner part of the distributor forming a smooth transition from the polypropylene piece to the copper, so that no steps or bumps were present for the flowing test solution in the annular space. Water from the circulating units was ducted through the central part of the distributor and into the copper pipe. An outer rim in the central part was machined to receive the Plexiglas pipe.

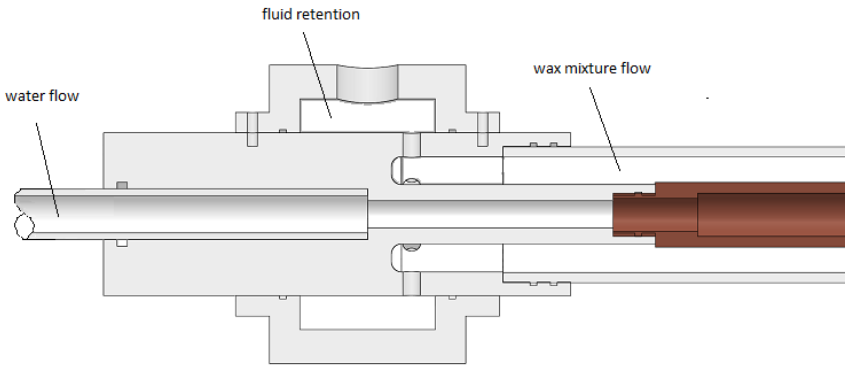


Figure 3.14: Cross sectional view of the water and test fluid distributor.

The outside ring was mounted and fixed over the central part and it

had the function of evenly distributing the incoming test fluid into the annular test space. To this end, the incoming fluid entered an annular chamber formed between de ring and the central part through a single 1/2-inch, NPT-threaded hole. The flow from the annular chamber was guided to the annular space of the test section through six, 9-mm-diameter holes evenly distributed around the central part circumference. A similar distributor piece mounted at the end of the test section ducted the fluid coming from the annular test section to a single hose that was connected to the cylindrical tank reservoir.

### The external water tank

The annular test section formed by the outer Plexiglas pipe and the inner copper pipe, joined together by the two flow distributor pieces was positioned inside a PVC external tank filled with water, as illustrated in Figure 3.15. The objective of the tank was to establish a well-defined thermal boundary condition for the outer pipe and, at the same time, isolate the test section from the laboratory temperature fluctuations. During the tests, the water in the tank was maintained at the same temperature as the temperature of the test solution entering the annular test section. This temperature match guaranteed that there were no heat losses through the outer Plexiglas pipe, a remarkable feature of this test section design.

The tank had dimensions of 1400 x 270 x 200 mm (length x height x width). The front and back windows of the tank were made of Plexiglas to allow visual access to the wax deposition process occurring inside the annular test section. The tank was open at the top, so that it was possible to install an immersion water circulator and temperature controlling unit, that kept the tank water temperature under control.



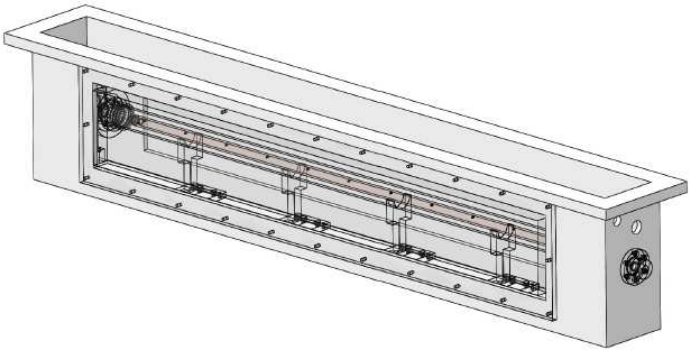

Figure 3.15: Illustration of the test section within the external water tank.

### 3.2.3
### Wax mixture reservoir

The cylindrical stainless steel reservoir used to maintain the test solution is illustrated in Figure 3.16. It had internal dimensions of 340 x 421 mm (diameter x height), and an approximated capacity of 36 l. However, the reservoir was not completely full, under operation, its total solution volume was of 23.2 L. This volume of test solution was determined based on the expected depletion of the solution wax concentration due to the formation of the wax deposit on the inner copper tube. With the solution volume used the maximum wax depletion due to deposition was of the order of 8 % of the total wax amount, which rendered a final was fraction in solution of 18.7%.

The reservoir was positioned over a heated plate, wrapped with heating tracer tapes and covered with wool insulation material. The heated plate had a magnetic agitator function, so that the test fluid was kept agitated inside the tank. Moreover, a 200 mm long stainless steel coil was installed inside the tank. The coil was fed with water from a thermostatic bath, maintained at $40^oC$. The cover of the tank was made of plexiglas, so that it was possible to view the inside of the tank, and check for the existence of solid crystals.

Figure 3.16: Stainless steel cylindrical tank used to store the test solution for the annular test section.

### 3.2.4
### The volumetric pump

A Netzsch NEMO021 volumetric pump was used to circulate the test solution from the reservoir into the test section and back to the reservoir. The pump flow rate was controlled by a frequency inverter, which had a frequency range from 0 to 60 Hz. The maximum flow rate produced by the pump was $2.1m^3/h$. The pump was calibrated by the gravimetric method

employing kerosene at $40°C$. The calibration curve relating the pump frequency of revolution to flow rate is presented in Figure 3.17.

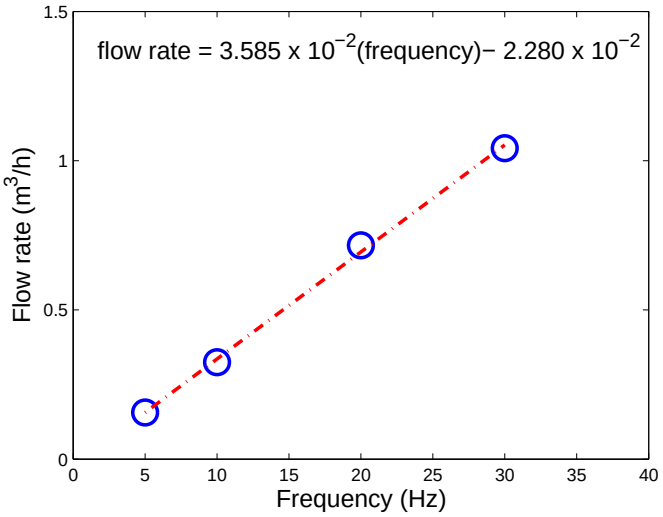


Figure 3.17: The annular test section pump calibration curve.

The pump was involved by heating tracer tapes and covered with wool insulation to avoid wax crystals formation. At the outlet of the volumetric pump a $2\mu m$ oil filter was installed to assure that no solid entered the inlet of the test section. The oil filter was also wrapped with heating tracer tapes and covered with wool insulation.

### 3.2.5
### The temperature acquisition system

The data acquisition system employed was an Agilent 34970A with an USB interface and equipped with a 20-channel module board, yielding an acquisition rate of 60 channels per second. The temperature measurements were obtained using the internal reference of the board. A Labview software was developed to control the data acquisition, and register the data to '.txt' files. The temperature data were treated using Matlab-based routines.

### 3.2.6
### The camera

A 1.4 Mpixel digital camera was employed to acquire side images of the test section while the wax deposition was taking place over the cooper pipe. The camera was a Axiocam MRc from Axio Vision, with time lapse function. The full resolution of the camera was 1388 x 1040, and uses a 2/3"CCD sensor with 6.5 $\mu m$ pixel size. The camera was coupled with a 30-80-mm zoom lens. The camera and lens were mounted in a 3-axis coordinate table with a traveling

range of 1100 x 150 x 100 mm, respectively in the longitudinal, transverse and vertical directions. The positioning resolution of the coordinate table was of the order of 0.1 mm.

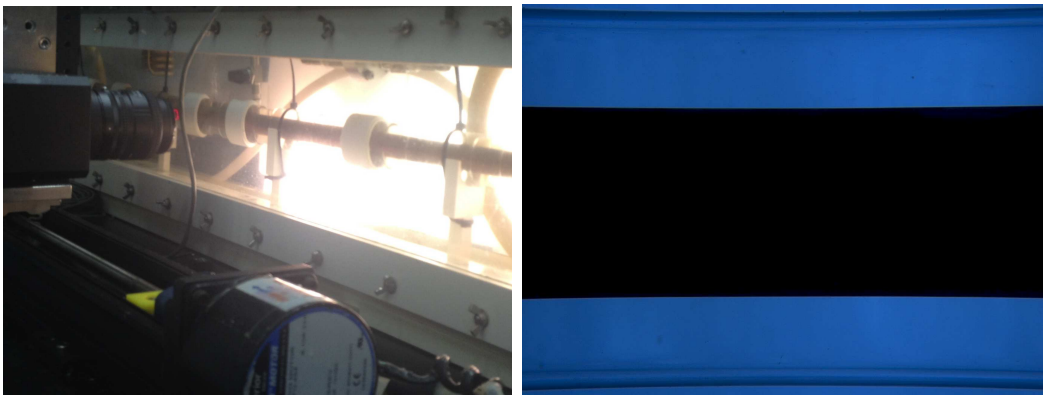

3.18(a): 3.18(b):

Figure 3.18: (a)Backlightening used in the deposition experiments. (b) Typical photo of the test section with the copper pipe in focus.

As it can be seen in Figure 3.18, back illumination was employed to obtain the images of the wax deposits. This illuminating technique produced images that facilitated the processing techniques employed to extract the image geometric characteristics. The back illumination was implemented by a rectangular panel of white LEDs. The low heating produced by this light sources was an interesting characteristic for the deposition experiments conducted.

In Figure 3.18 it is possible to observe an example of an image obtained with the back light illumination employed. The black region observed in Figure 3.18(b) is the image of the clean copper pipe surrounded by the flowing fluid of test. The boundaries of the concentric Plexiglas pipe can be seen at the top and bottom edges of the image. The image of the clean pipe was used to obtain the pixel-to-millimetre calibration value necessary for the measurements of the deposited was thickness. Measurements of the wax deposit thickness registered in each image frame acquired were processed by a specially written Matlab code.

# 4
# Test Fluid Characterisation

In the present chapter the characterization of the test fluids used in the experimental work will be presented. The test fluids were specially prepared to provide the experiments with mixtures that present a distinct separation of the solvent carbon numbers from those of the wax components. Simpler test fluids with well-defined properties also facilitate the numerical simulations of the wax deposition problem, providing a better ground for comparison with the experiments.

The WAT and WDT measurements for the test fluids, as well as the results from composition analyses and property measurements will be described. The paraffin wax used to formulate the test fluid was obtained from distillation of crude oil at the Flow Assurance Laboratory at the Center of Research and Development, Cenpes from Petrobras. The compositional analyses were also conducted at Cenpes. Microscopy WAT and WDT measurements were conducted in the Laboratory of Fluids Engineering (LEF) at PUC-Rio. The rheometry measurements as well as the calorimetry analyses were conducted at Cenpes.



## 4.1
## Test fluid

The test fluid used in the present work was a mixture of $C_{12}$ with 20% in mass of paraffin wax. The paraffin wax was obtained from distillation of a waxy fluid which was then purified. During the test campaign it was necessary to produce an additional batch of test fluid. Although, the objective was to produce a second batch with the same properties, slight differences were found between the first and second batches. The first test fluid was employed in the experiments conducted in the rectangular test section, while the second fluid was employed in the experiments with the annular test section. The properties of both test fluids will be reported here.

The two slightly different paraffin waxes obtained were named WAX1 and WAX2. WAX1 consisted of hydrocarbons ranging from $C_{24}$ to $C_{36}$ with a melting point of $55.2^oC$ and a density of 732.6 $kg/m^3$, at 60 $^\circ C$. WAX2

consisted of hydrocarbons ranging from $C_{24}$ to $C_{37}$ with a melting point of $54.8^oC$ and a density of 732.0 $kg/m^3$, at 60 $^\circ C$. The average molar mass of the waxes were 403.4 and 400.5 $\frac{kg}{kmol}$ which corresponds to a average carbon number of 28 and 29, respectively. The curves of the density variation with temperature of the two wax mixtures, composed by WAX1 and WAX2, are exhibited in Figure 4.1.

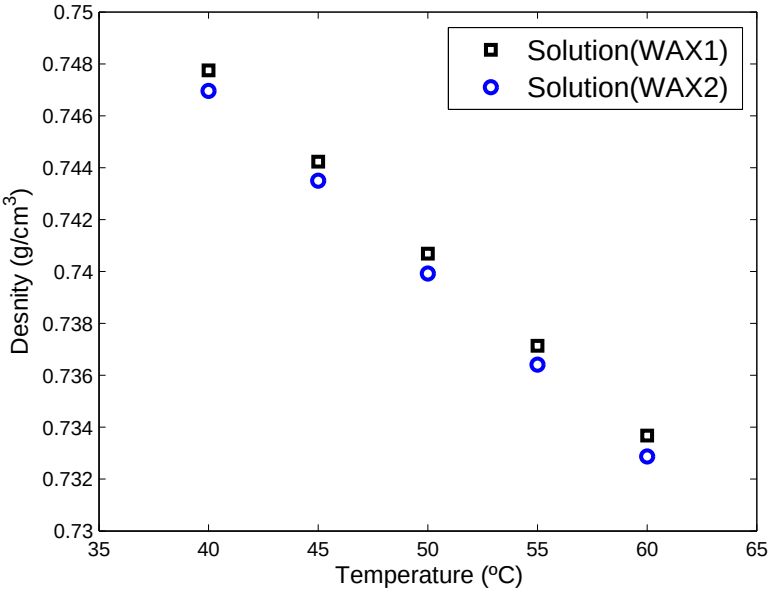


Figure 4.1: Density variation with the temperature of the two mixtures employed as test fluids, based on paraffin WAX1 and WAX2, and solvent $C_{12}$, at 20% in mass of paraffin wax.

The solvent was obtained from Shangai IS Chemical Technology and it consisted of 99% of $C_{12}$, according to the manufacturer specifications. Our test found that the solvent contained 99.4 % of $C_{12}$, 0.5 % of $C_{11}$ and 0.1 % of $C_{13}$. The average molar mass of the solvent was $170.3\frac{kg}{kmol}$. The variation of the solvent density with temperature is exhibited in Figure 4.2.

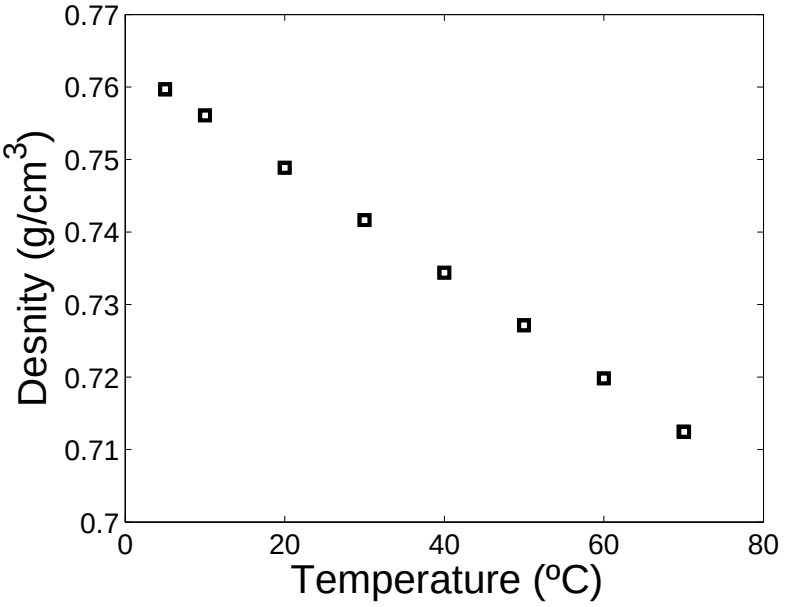


Figure 4.2: Temperature variation of the density of solvent $C_{12}$.



## 4.2 WAT measurements

Waxes are essentially long-chain hydrocarbons with carbon chain lengths ranging from $C_{18}$ to $C_{75}$. Crystalline in nature, waxes tend to solidify from solution below the thermodynamic solidification temperature. Crystallization usually involves two distinct stages, nucleation and growth. As the solidification temperature is approached, the molecular motion energy is reduced, and the randomly chaotic molecules in the melt tend to move closer together and form clusters of adjacently aligned chains. In practice, a certain degree of sub-cooling is needed for the solidification to occur.

Indeed, two distinct critical temperatures define the wax solidification process. The first one is called wax dissolution temperature, WDT. Bhat and Mehrotra (2004) has shown that the WDT approaches the thermodynamic solidification temperature better than WAT. The clusters are only stable below the wax dissolution temperature (WDT), since they are disrupted by thermal motion above this temperature. The second temperature is a sub-cooled temperature in relation to the WDT, which is the wax appearance temperature, WAT. The WAT is process-dependent temperature related to the critical moment where the first clusters appear in the sample. The size of the observed structure depends on the resolution of method of observation. Some methods may detect small clusters, others can only detect big ones. The WAT is usually around 2-3 $^oC$ lower than the WDT. WAT values are dependent upon a number of factors, which include oil composition, cooling

rate, pressure, paraffin concentration, molecular mass of paraffin molecules, occurrence of nucleating materials such as asphaltenes and other nucleation sites, corrosion, water-oil ratio, and shear levels.

The WAT laboratory measurements are sensitive to the experimental technique employed, such as the standard ASTM D2500-88 or IP 219/82 methods, differential scanning calorimetry (DSC), cross polar microscopy (CPM), light transmittance, viscometry, and cold finger, as described by Lira-Galeana and Hammami (2000).

In the present work, the WDT was measured by cross polarised microscopy. The WAT was measured by CPM, DSC and viscosimetry. As mentioned before the methods are distinguished by the sizes of the structures they may detect. The CPM method usually measures a higher value for the WAT than the viscosimetry measurements, since in microscopy the first crystals may be seen before a gel structure capable of producing a detectable viscosity shift, is formed. DSC measurements present usually high levels of experimental uncertainty associated with the determination of the onset of precipitation.



### 4.2.1
### Cross-polarised microscopy measurements

The use of the CPM method for measuring WAT is based on the principle that all crystalline materials rotate the plane of polarization of transmitted polarized light. Hence, by crossing two prisms on opposite sides of the oil sample, all light is initially blocked and the entire field of view appears black. On cooling, the crystallizing material appears as bright spots against this black background. This technique usually provides the most conservative value of the oil WAT.

A Stemi 2000-C, Zeiss microscope equipped with two polarizing filters was used to visualize the sample. A transparent test cell was developed for these measurements, as shown in Figure 4.3. The cell was composed by two blocks of plexiglass with dimensions 75 x 25 x 13 mm. The blocks had rectangular-shaped channels machined along their longitudinal direction. Water from a bath circulator was pumped through the channels, providing thermal control to the cell. A fine-gauge thermocouple was positioned at 0.5 mm from the surface of the bottom channel flow, to measured the sample temperature. The thermocouple was fabricated from 0.125-mm-diameter, chromel and constantan wires. Additionally, a polystyrene jacket covered the microscope sample area to avoid ambient temperature interference.

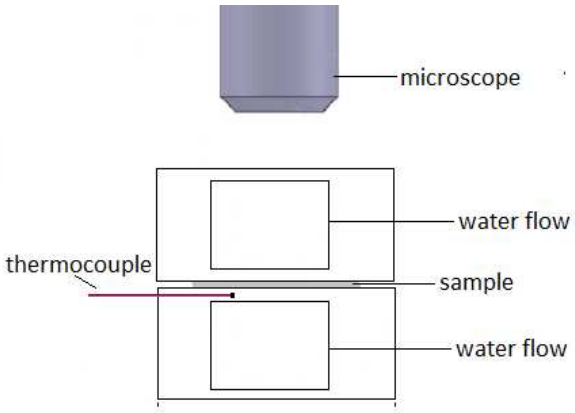


Figure 4.3: CPM experimental apparatus.

The experimental procedure involved preheating the oil to $60°C$ for 30 min, so as to melt the waxes and homogenize the sample. The sample was then cooled to $40°C$ and positioned over the top surface of the lower block. The second plexiglass block was then positioned over the sample. The two blocks were at a uniform temperature of $40°C$ when the sample was first positioned. The set was then homogenized at $40°C$ for 5 minutes more. The sample cooling process was performed in steps of $1°C$, with a cooling rate of $0.2°C/min$, from 40 to $30°C$. Each temperature step level was held for 15 minutes. The temperature at which the first crystal appeared was registered as the wax appearance temperature (WAT). Later, the sample was heated in steps of $1°C$ from 30 to $40°C$, with the same cooling rate. The temperature at which the last crystal re-dissolved into the fluid was registered as the wax dissolution temperature (WDT). The values encountered for the WAT and WDT are presented in Table 4.1. The uncertainty estimative of WAT and WDT measurements using CPM method are of $\pm$ 0.60 and 0.65 $°C$, respectively. The experimental uncertainty reported in the table was based on the thermocouple uncertainty and on the mean deviation observed from replication of the measurements.

Table 4.1: WAT and WDT measurement in the CPM apparatus of the mixture with WAX1.

| **Quantity** | **Value** $°C$ |
|---|---|
| WAT | 34.50 |
| WDT | 36.30 |

### 4.2.2
### Rheometry measurements

The determination of WAT using viscosity measurements uses the change in slope of the viscosity versus temperature curve. When passing from Newtonian to non-Newtonian behaviour, the oil viscosity curve deviates from the Arrhenius curve. The WAT measurements are usually performed under constant shear rate between 30 and 300 $s^{-1}$ (Huang et al. (2015)).

A MCR-301 Anton Paar Physica rheometer with couette geometry and a 1.13 mm gap was used for the WAT measurements. The cooling of the sample was provided by a Peltier cooler device.

The experimental procedure encompassed pre-heating the equipment and the sample to $60°C$ for two hours. Once the sample was positioned in the rheometer and the temperature equilibrium attained, the sample was cooled from 60 to $30°C$, at a cooling rate of 0.5 $\frac{°C}{min}$. After preliminary tests, the shear rate chosen for the measurements was of 120 $s^{-1}$.

The average curve for the viscosity variation with the temperature of WAX2 is exhibited in Figure 4.4. From that figure it is possible to notice that around 35 $^oC$ there is a jump in the viscosity value from around 1 $mPa.s$ to around 48 $mPa.s$ at 30 $^oC$. The results are presented in Table 4.2. The uncertainty estimative of WAT measurements using rheometry is of $\pm$ $0.6°C$. The uncertainty calculation was based on the resolution of the temperature measurement from the Peltier device, combined with the resolutions of the cooling ramp.

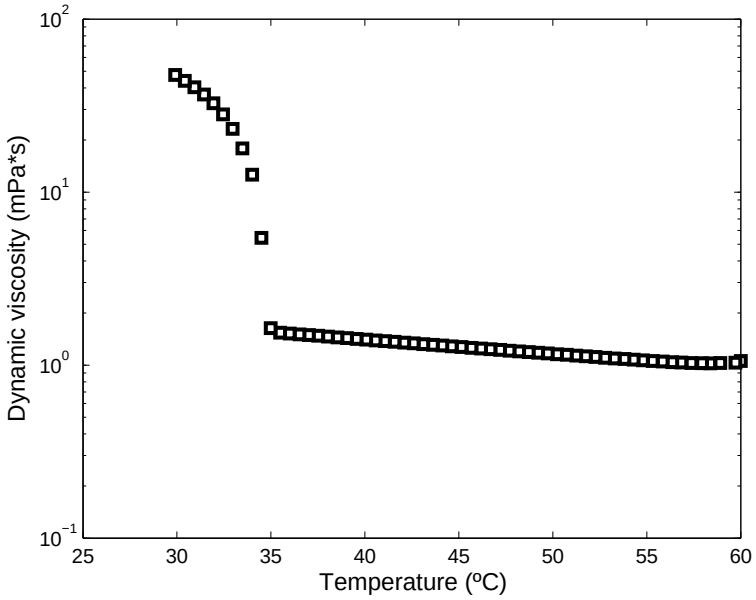


Figure 4.4: Temperature variation of the viscosity of the wax mixture prepared from WAX2.

Table 4.2: WAT measurement by rheometry of the two mixtures with waxes: WAX1 and WAX2.

| **Wax on mixture** | **Value** $°C$ |
|---|---|
| WAX1 | 33.80 |
| WAX2 | 34.50 |

### 4.2.3 DSC measurements

In differential scanning calorimetry, the heat flux that crosses the sample is estimated as a function of the temperature. The principle is to measure the difference in the heat flux that crosses the sample and the one that crosses a reference sample. The heat flux is inversely proportional to the thermal resistance of the system. The equipment is largely used to study phase change, since it allows the detection of the latent heat of phase change. The measurement of WAT with the DSC consists of identifying the onset of crystallization based on a exothermic pick that appears while cooling the sample. However the detection of the onset of heat flux shift is a source of experimental uncertainty.

In the present analyses, the samples were scanned from 50 to 0 $°C$. The thermograms are exhibited in Figure4.5. Table 4.3 presents the WAT measuements based on DSC data. The uncertainty estimative of WAT measurements using DSC method is of $\pm$ 1$°C$.

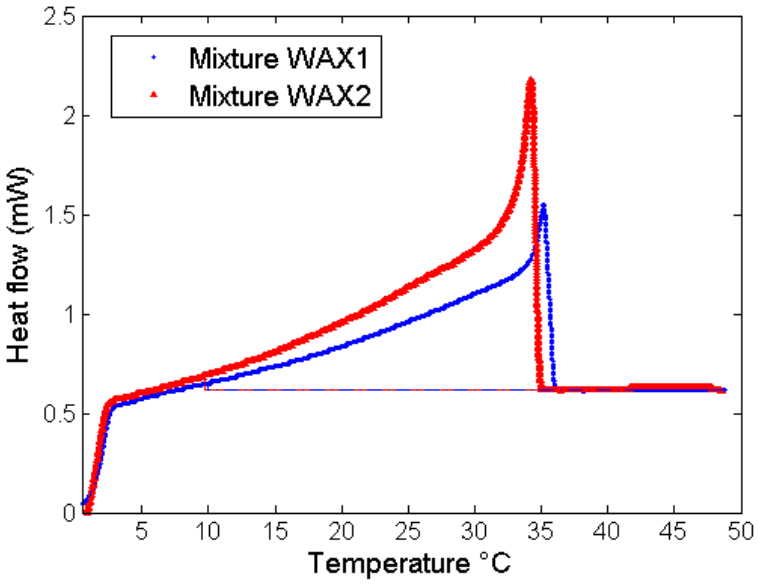


Figure 4.5: DSC thermogram.

Table 4.3: WAT measurement by DSC of the two mixtures with waxes: WAX1 and WAX2.

| **Wax on mixture** | **Value** $°C$ |
|---|---|
| WAX1 | 35.94 |
| WAX2 | 35.11 |

## 4.3 Chromatography

Chromatography is a separation technique, through which the components present in complex mixtures are resolved. Once separated, these components are analyzed, allowing the determination of the original composition of the sample. There are many chromatography methods available and the choice of the method is determined by the sample itself, from properties like its physical state (gas, liquid or solid) and the nature of the analyte. In the present case, the chosen method was the High Temperature Gas Chromatography, or just HTGC.

The HTGC method is regularly applied to complex mixtures of hydrocarbons, like crude petroleum samples, as it allows the simulation of the distillation curve of the original sample. It consists of a short 5 meters steel column, which can stand high temperatures, 450 $°C$, reached at the end of the temperature ramp of the method. The injector used is normally an on-column injector, with no split rate, to guarantee the total injection of the sample in the chromatographic column. The sample is injected with helium as the mobile phase. The detector at the end of the column is a Flame Ionization Detector, or FID. The original fuel for the flame is hydrogen. When some molecules different from hydrogen are burned an increase in the flame conductivity is detected. The role of the detector is to determine the mass of the sample being burned. Thus, the flame conductivity is calibrated versus the mass of the sample. The method is further described in the ASTM D7169 standard.

To calibrate the elution time, an injection of the Sigma-Aldrich standard mixture Polywax 500 diluted in carbon disulphide should be performed at every five sample injections. The calibrated retention times allow the discrimination of the paraffins in the sample. The HTGC equipment is presented in Figure 4.6.

Figure 4.6: HTGC equipment.

The chromatogram of the original mixture with WAX1 is presented in Figure 4.7. The composition of the sample is obtained from the integration of the peeks found in the chromatogram in Figure 4.7. The integration of one peek is directly proportional to the mass content of a corresponding molecule in the sample. The mass in percentage versus carbon number of WAX1 and WAX2 solution are exhibited in Figures 4.8 and 4.9.

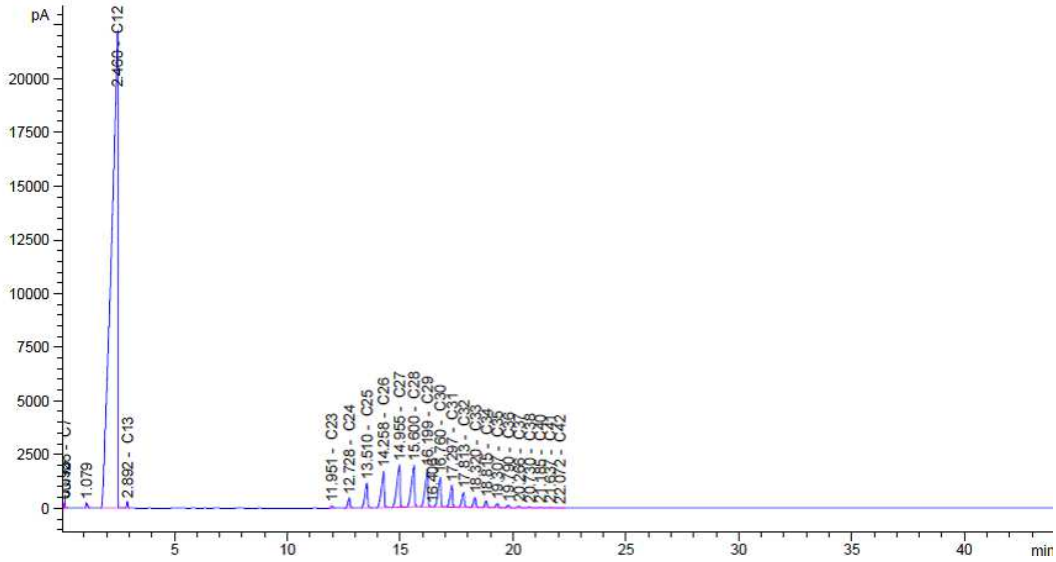


Figure 4.7: Chromatograph of original mixture with WAX1.

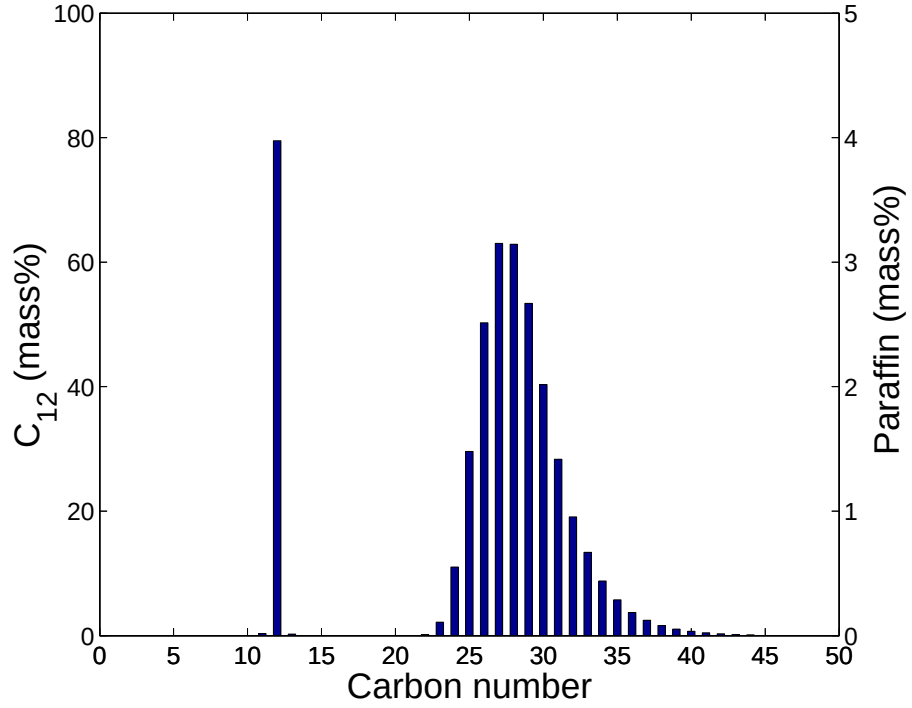


Figure 4.8: Mass based chromatograph of original mixture with WAX1.



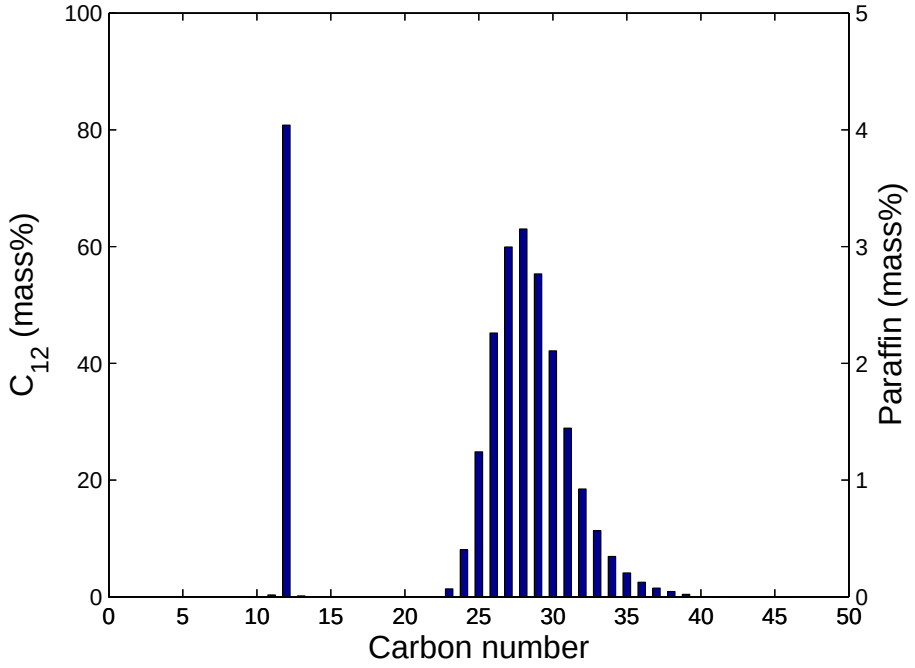


Figure 4.9: Mass based chromatograph of original mixture with WAX2.

# 5
# Deposition Measurements

This chapter presents the wax deposition results obtained from the experiments conducted in the annular test section described in Chapter 3. The main objective of the experiments was to provide quality data on the temporal and spatial evolution of the wax deposits, obtained for a well-defined geometry and for well-controlled boundary and initial conditions. The fluid employed in the tests was the wax mixture with WAX2, presenting a clear distinction between solvent and wax components, with composition and thermo-physical properties properly characterized, as described in Chapter 4. The annular test section employed offered excellent control of heat losses, a problem that affected the tests on previously employed rectangular test sections. All these features confer to the deposition data obtained a unique level of quality that make them suited to serve as a data bank for testing simulation models, and also to contribute to the understanding of the underlying phenomena associated with the complex deposition process.

A literature search reveals several methods for measuring the wax deposit thickness during flow loop experiments. Among them are the pressure differential methods (Matzain (1999); Brown et al. (1993); Singh et al. (2001a)), the heat transfer methods (Bott and Gudmundsson (1977); Creek et al. (1999); Matzain (1999)), the spool piece methods (Burger et al. (1981); Creek et al. (1999); Matzain et al. (2002)), the laser based methods (Hoffmann and L.Amundsen (2010); R.Hoffmann et al. (2012)) and the visualization methods (Weingarten and Euchner (1988); Tinsley and Prud'homme (2010); Veiga et al. (2012)). The pressure differential are one of the most used methods due to its capacity of generating on-line data of deposit thickness. The pressure drop in the flow loop is correlated to the variation in pipe diameter by a hydrodynamic friction factor. This method provides an average thickness information that, however, may be associated with high levels of experimental uncertainty. In particular, for turbulent flows, sloughing may cause variation in the deposit roughness. As it is known, the friction factor is a function of the deposit roughness, for turbulent flows. This may cause elevated experimental uncertainty in the use of this method. The spool piece method has also been

largely employed, usually together with other methods, for validation purposes. In this method, the flow in the deposited pipe is ceased and the test section is emptied. The mass of wax deposit is then inferred by volume change or weight measurements. Deposit thickness data were reported to vary up to 1500% from one method to the other (Creek et al. (1999); Matzain (1999)), indicating that high uncertainties are associated in most methods. Some improvement has been proposed recently, with the laser-based method. In this method the flow also has to be interrupted for the measurement to take place, but a deposit distribution in the pipe can be obtained. Experimental error of the order of 20% have been associated with the use of such method R.Hoffmann et al. (2012).

Visual methods present the lowest experimental uncertainties, together with the capability of providing spacial and temporal information on the deposit thickness. Moreover, experimental uncertaintys of less than 5% may be obtained. Its limitation is, obviously, the need of optical access to the interior of the flow region. Usually the walls of the test section are made in a transparent material that permits visual access to the inner part of the test section where wax deposition takes place. Rectangular geometries were the most commonly employed with visual methods(Weingarten and Euchner (1988); Tinsley and Prud'homme (2010); Veiga et al. (2012)). However, the control of heat losses from these geometries is not always a straightforward task. For instance, in the work of Veiga et al. (2012) a rectangular geometry was used in flow loop experiments. The test section presented undesired heat transfer between the transparent walls and the body of the heat exchangers responsible for inducing deposit formation in the test section. The wax formation on the transparent walls reduced the visual access to the interior of the test section, increasing the experimental uncertainty on the deposit thickness measurements. Also, the uncontrolled heat transfer to the ambient could not be properly accounted for by the simulation models that attempted to calibrate its predictions using those experimental data.

The annular geometry test section designed and employed in the present work offered some advantages over rectangular geometries regarding the control of the experimental conditions. As described in Chapter 3, the annular test section was immersed in a water tank with controlled temperature, what provided total thermal decoupling from the laboratory temperature variations. Also, the possibility of setting the temperature level in the water tank allowed for the minimization of heat losses from the test fluid flowing in the annular channel to the ambient, through the Plexiglas outer pipe wall. Indeed, the tests were conducted with the temperature of the water in the tank set at the same level as that of the bulk flowing solution. With this

configuration, all the heat lost by the solution, and responsible for the wax deposition process, was taking place under controlled and known conditions.

Another relevant feature of the annular test section employed was the monitoring of the spatial distribution of the copper wall temperature during the deposition experiments, by the fine thermocouples embedded in the copper tube wall. This is a relevant piece of information for the proper modelling of the experiments.

The experiments in the annular test section were performed under three flow rates, representing three Reynolds number, namely, 743, 1440 and 2073. The channel flow Reynolds numbers were calculated based on the average velocity of the flow, the hydraulic diameter and on the properties of the wax solution, as described in Equation 5-1.

$$Re = \frac{\rho \bar{V} D_h}{\mu} = \frac{\rho \; Q/A \; (D_o - D_i)}{\mu} \tag{5-1}$$

where $\rho$ and $\mu$ are the density and dynamic viscosity of the wax solution based on WAX2 at $38^oC$, based on the data presented in Chapter 4. $\bar{V}$ is the average velocity calculated as fraction of the flow rate for the cross–sectional area; where $Q$ is the flow rate and $A$ is the area of the cross–section. The hydraulic diameter is defined as $D_h = 4A/P$ where $P$ is the wetted perimeter of the cross–section. In annular geometries that quantity is reduced to $(D_o - D_i)$, which is the subtraction of the inside from the outside diameter of the annular space.

The annular test section was designed to provide fully developed velocity profiles at a distance from the entrance of approximately 40% of the total test section length. Although neither pressure drop or velocity profile measurements were performed to confirm that flow condition, we believe that the measured small temperature variations in the bulk fluid, between the entrance and exit sections, did not produce property variations that would significantly alter the attainment of the hydrodynamically fully developed condition. The velocity profile at the entrance was not determined experimentally, a piece of information that is certainly useful for numerical modelling the flow. An unheated developing length was unfortunately not included in the design of the test channel and it is certainly a good suggestion for inclusion in a future test section design.

## 5.1
## The experimental procedure

At the beginning of the deposition experiments the desired solution flow rate was set at the pump controller, and the whole flow loop was maintained

in thermal equilibrium at $38°C$ ($\pm 0.2°C$), which is a temperature $3.5°C$ higher than the WAT for the test solution employed. As cited before, wax solution based on WAX2, with properties described in Chapter 4, was employed in the annular test section experiments. To obtain thermal equilibrium, water from one of the bath circulators was pumped through the cooper pipe while the mixture was flowing in the annular space, both at $38^oC$. Another bath circulator was already set to $12^oC$ and ready to be used. To initiate the experiments, a rapid valve setup change at the cooling circuit was implemented in such a way that the $12^oC$ water from the standby circulating unit was directed to the interior of the copper pipe of the test section. That procedure produced the fastest cooling rate that the test section could produce, reducing the copper pipe temperature from the initial $38^oC$ to $12^oC$. Detailed data on the cooling of the wall is presented in section 5.1.1.

After the cooling of the wall started, a wax deposit gradually formed over the cooper pipe. The transient evolution of the deposit distribution along the pipe was measured optically by the procedure that will now be outlined.

The digital camera mounted on a rail was positioned so as to provide a side image of the annular test section, as indicated in the sample image presented in Figure 5.1. The field of view of the camera was of the order of 48 mm, insufficient to image the full 1-meter length of the test section. To circumvent this limitation, a pseudo-transient procedure was employed. In this procedure, the camera was positioned at the beginning of the test section, imaging the first 48 mm of its length. The camera recording was started with the test section still at the hot steady state temperature. The wall cooling was initiated and the wax deposit formation was recoded until the desired steady state condition for the wax deposit was achieved. The experiment was then interrupted by circulating hot water through the copper pipe, removing the deposited wax. The camera was moved to a new axial position, while the attainment of a new hot temperature steady state was observed. At steady state, the cooling of the wall was again initiated and the wax build up registered by the camera. This procedure of forming and removing the deposit and moving the camera was repeated until all the desired axial positions along the test section had been visited. At each axial position, three replications of the experimental procedure were performed. It was verified, that a deviation of less than 5% was obtained in the measured deposit thickness, what was considered satisfactory.

Deposit images were obtained with back light illumination, what produced good contrast and facilitated the use of digital techniques to extract the desired geometric features of the image. Figure 5.1 represents a pair of

sample images captured by the camera. In image (a) the deposition process was not started and the clean copper pipe and the outer Plexiglas pipe can be clearly visualized. This image of the clean pipe was used as part of the image calibration procedure. Image (b) was captured at about 2 minutes after the initiation of the cooling of the wall and show the wax deposit formed.

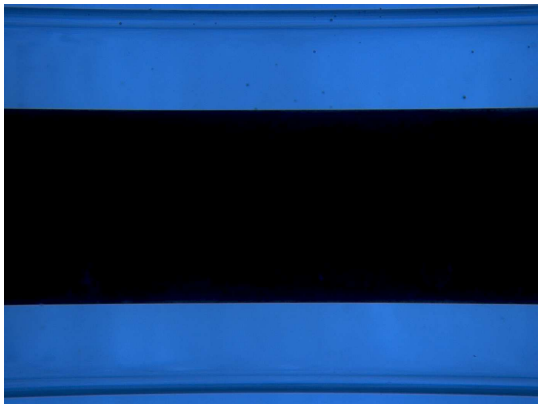

5.1(a):

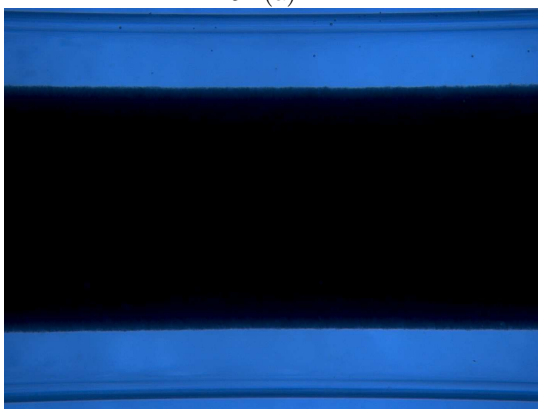

5.1(b):

Figure 5.1: Images captured at position 4 = 333 mm, Re=2073: (a) initial image of the clean cooper pipe and (b) image after two minutes of cooling.

The images captured from a complete experiment were loaded to a Matlab image processing code. Due to the good quality of the images captured, only simple processing operations were necessary to extract the information of the deposit thickness evolution. The edges of the image were clipped off and the images were made binary. Then, at each axial position in each image, the black pixels corresponding to the deposited wax were counted by the software. This procedure was repeated for each image corresponding to a particular time. The images of the clean pipe were employed to determine the pixel-to-millimetre relation at each axial position of the images. This calibration procedure used the known dimension of the copper pipe diameter. A typical calibration value employed was 26.5 pixel/mm. This procedure was repeated for seven axial

positions of the camera along the test section length, as indicated in Figure 5.5.

### 5.1.1 Temperature data

As described in Chapter 3, the copper pipe was instrumented with 11 fine thermocouple probes axially distributed along the pipe length. These probes were designed so as to position the thermocouple junction at about 0.5 mm from the copper pipe surface giving, thereby, an excellent assessment of the deposition surface temperature. Each thermocouple probe was connected to the data acquisition system that acquired data at a rate of 1 Hz. Thus, the axial and temporal distributions of the deposition wall temperature were measured and available to be used as boundary conditions for the simulations process. The inlet and outlet bulk temperature of the solution were also measured along the experiments at the same 1-Hz rate. A traversing probe was also employed to measure temperature profiles across the liquid and the deposit and at the deposit–liquid interface. These measurements will be commented in Chapters 6 and 7.

All experiments were repeated at least three times, in order to assess the level of repeatability. A time-averaged temperature for each position of the pipe was calculated based on the data of the experiments replication. As will be demonstrated shortly, the spatial variation of the wall temperature along the pipe length was not significant. Thus, a spatially–averaged temperature was calculated for each time instant, so as to allow an assessment of the rate of cooling of the wall. These results are shown in Figures 5.2 and 5.3.

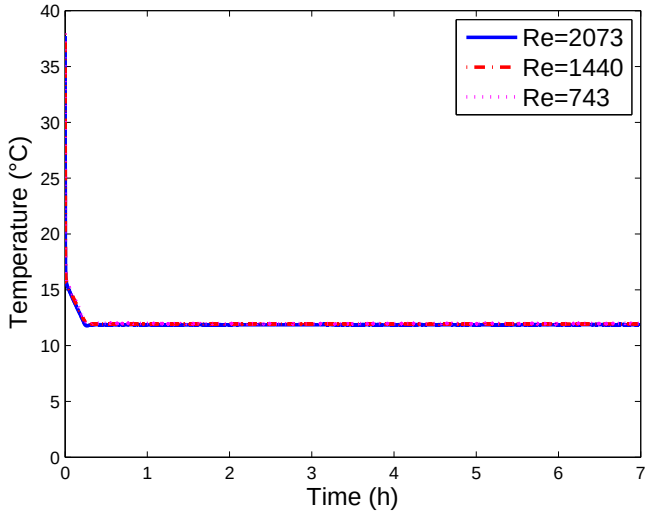


Figure 5.2: Temporal variation of the spatially–averaged pipe wall temperature for Reynolds numbers 743, 1440 and 2073.

As can be seen from figure 5.2 the wall temperature variation was virtually the same for the three values of the Reynolds numbers tested. This is a good feature of the test section, indicating that the cooling capacity of the circulating bath is able to stand the different thermal loads, and that all depositions tests could be performed under the same cooling conditions, irrespective of their Reynolds number values. Figure 5.3 is an expanded view of the previous figure where the initial cooling transient can be better appreciated. Also, it can be seen that in the early stages of the cooling there is virtually no Reynolds number effect. In the first 40 seconds the wall temperature drops from $38^oC$ to $15.5^oC$, what represents a cooling rate of the order of $32^oC/min$. After this initial period, the cooling rate drops to $0.25^oC/min$ for nearly 15 minute, when the temperature finally stabilizes at $12^oC$. The temperature was maintained at $12^oC$ during the rest of the experiments for all the Reynolds number evaluated.

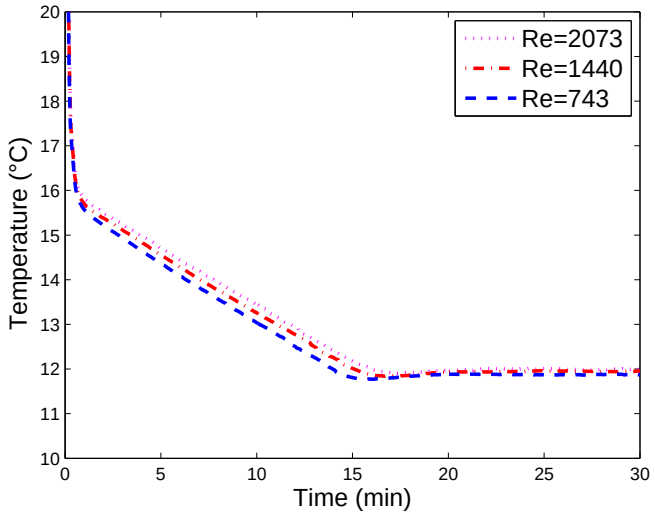


Figure 5.3: Expanded view of the initial stages of the spatially–averaged pipe wall temperature transient for Reynolds numbers 743, 1440 and 2073.

As mentioned before, the axial variation of the pipe wall temperature was negligible for all Reynolds number, as can be seen in Figure 5.4. It is important to notice that the inlet and outlet temperatures were maintained at $38°C$ ($\pm 0.2°C$) during the whole experiments, for all Reynolds numbers, which is an indication that no axial heat loss was taking place though the plexiglass pipe.

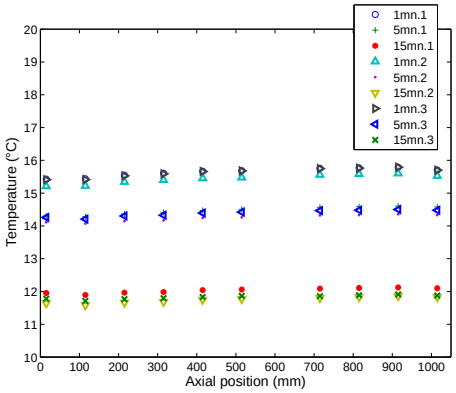


5.4(a):

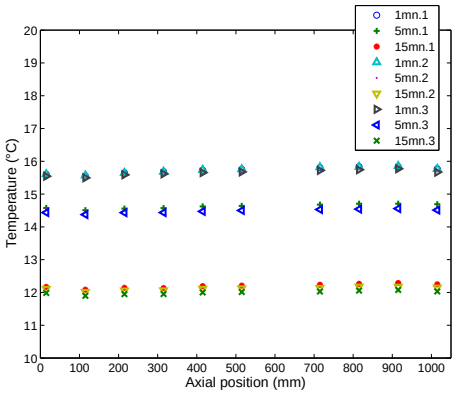


5.4(b):

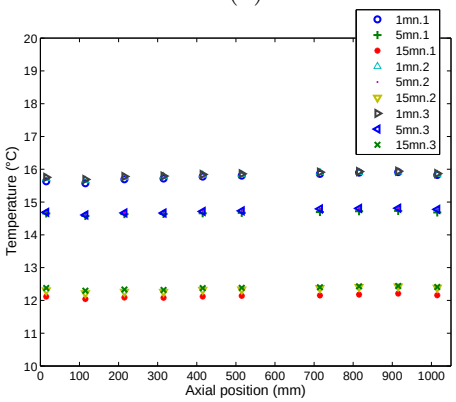


5.4(c):

Figure 5.4: Temporal and axial variation of the copper pipe wall temperature for (a) Re=743, (b) 1440, (c) 2073, and three repetitions test, 1, 2 and 3.

### 5.1.2 Image acquisition

Image acquisition of the transient deposit formation along the annular test section length was performed at different rates. At the early stages of the deposition process, the growth rate of the deposit is fast. So, in the first two minutes, images were acquired at a rate of one image per second. The frequency

of image acquisition for all tests is exhibited in Table 5.1. Tests durations of one, four and seven hours were undertaken, as it will be clarified latter.

Table 5.1: Image acquisition data.

| | | **Acquisition** | |
|---|---|---|---|
| | | duration | image interval |
| **One hour test** | | | |
| | video 1 | 2 min | 1 sec |
| | video 2 | 5 min | 10 sec |
| | video 3 | 55 min | 5 min |
| **Four hour test** | | | |
| | video 1 | 2 min | 1 sec |
| | video 2 | 5 min | 10 sec |
| | video 3 | 55 min | 5 min |
| | video 4 | 3 h | 10 min |
| **Seven hour test** | | | |
| | video1 | 2 min | 1 sec |
| | video 2 | 5 min | 10 sec |
| | video 3 | 55 min | 5 min |
| | video 4 | 6 h | 10 min |



The growth of the deposit thickness was registered by the camera at 7 positions axially distributed along the channel length, as illustrated in Figure 5.5. The field of view of the camera had a length of approximately 52 mm in the axial direction, but since each image was clipped during the processing operations, the actual image length was smaller, about 46 mm for positions one to five and seven, and 19 mm for position six. At position 6, the camera imaged the deposit at the space between the sampling port and the temperature probe, and that was the reason for the narrower field of view at this position. The camera viewing positions were not equally distributed along the length of the channel due to the more pronounced variations of the deposit thickness at the first part of the channel. The location of each viewing position is described in Table 5.2, where the beginning of the cooper pipe was used as the reference point.

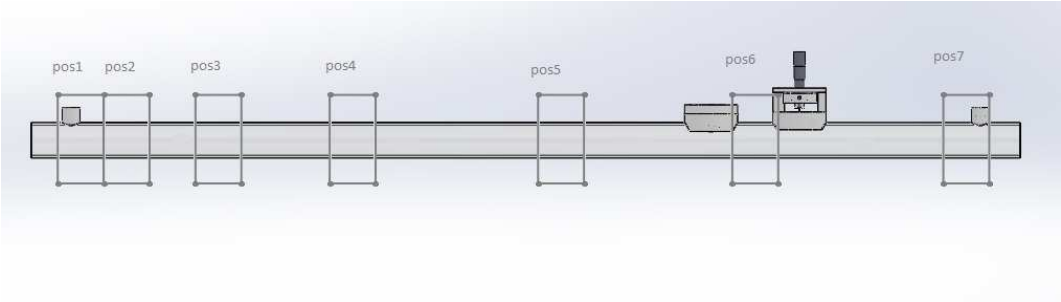


Figure 5.5: Camera axial field of view for the deposit visualization.

Table 5.2: Coordinates of camera positions.

| **Position** | **Initial coordinate (mm)** | **Final coordinate(mm)** |
|---|---|---|
| 1 | 4 | 50 |
| 2 | 66 | 112 |
| 3 | 176 | 222 |
| 4 | 310 | 356 |
| 5 | 544 | 590 |
| 6 | 766 | 785 |
| 7 | 951 | 997 |



## 5.2 Deposition results

### 5.2.1 Early stages of deposition

Before presenting the quantitative results for the spatial and temporal evolution of the deposit thickness, some images of the early stages of the deposition process will be presented. In the videos it was possible to see wax crystals appearing very close to the pipe wall, and initially being carried along by the flow. Then, the number density of crystals reaches a value that induces the formation of a thin immobile layer over the pipe surface.

Figure 5.6 was prepared to aid in the presentation of some deposit images. It presents the time evolution of the deposit thickness measured at an axial station located at 75% of the channel length. The data are presented for the three values of the Reynolds numbers investigated. The evolution of the wall temperature is also presented in the figure for reference purposes. It can be observed in the figure that the rates of deposition are inversely

proportional to the Reynolds number at the begging of the deposition process. For longer times, the thickness of the deposits tends to higher values for the lower Reynolds number.

Capital letters from A to L were inserted in Figure 5.6 to indicate the time instant and Reynolds number values at which the images of Figure 5.7 were taken.

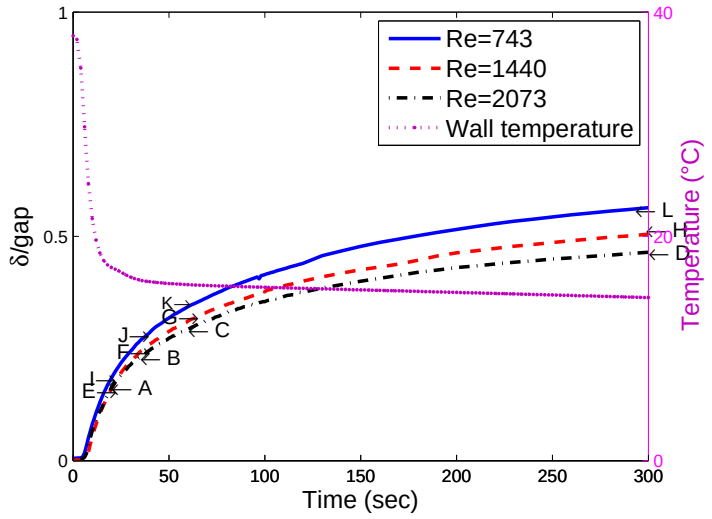


Figure 5.6: Dimensionless wax deposit thickness measured at position 6 (750 mm) for the initial stages of the deposition process, at Reynolds number 743, 1440 and 2073. Time variation of the pipe wall temperature also shown and referenced to the right ordinate.

A careful analysis of the images in Figure 5.7 shows that, at 20 s, for the Reynolds number equal to 2073, a dense cloud of flowing crystals is observed in image A. For Reynolds number equal to 1440 the denser cloud of flowing crystals appears a little later, at about 35 s, image F. The denser cloud is observed between 35 and 60 s, for the lowest Reynolds number investigated, 743. This observed behaviour can be linked to the behaviour of the thermal boundary layer that is thinner the higher the Reynolds number. Since the wall temperature is the same for all Reynolds number values, the thinner the thermal boundary layer the higher the concentration of wax crystal in the region limited by the wall temperature and the WDT, the higher temperature the solid phase can exist.

Since the wax crystals may only exist in temperatures under the wax dissolution temperature, WDT, the cloud of crystals may be a good indicative of the WDT isotherm in the thermal boundary layer.

The fact that the cloud of crystals in only observed at the very early stages of deposition may indicate that, at the very beginning of the cooling process, a large number of wax crystals are formed but do not constitute a fixed

deposit. Only when a certain value of the wax crystals saturation is attained, the solid deposit is formed. This critical saturation value may depend on the prevailing flow conditions.

After the cloud of crystals disappear, the interface of the deposit presents a somewhat rough appearance. For longer cooling periods, the deposit surface becomes smoother. This can be observed for the three values of the Reynolds number by following the time evolution of the interface images shown in Figure 5.7.

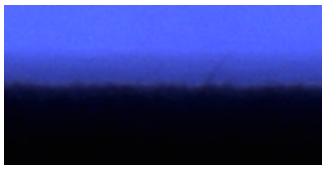

5.7(a): Image A, 20 seconds Re= 2073.

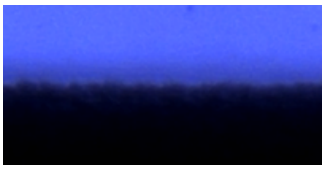

5.7(b): Image B, 35 seconds Re= 2073.

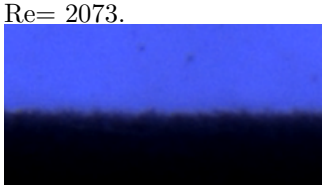

5.7(c): Image C, 60 seconds Re= 2073.

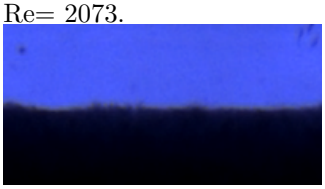

5.7(d): Image D, 300 seconds Re= 2073.

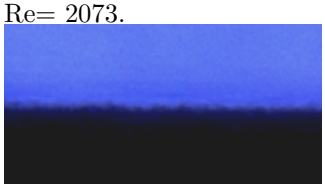

5.7(e): Image E, 20 seconds Re= 1440.

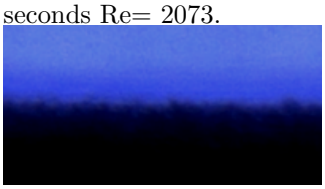

5.7(f): Image F, 35 seconds Re= 1440.

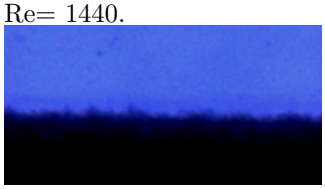

5.7(g): Image G, 60 seconds Re= 1440.

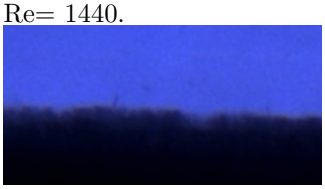

5.7(h): Image H, 300 seconds Re= 1440.

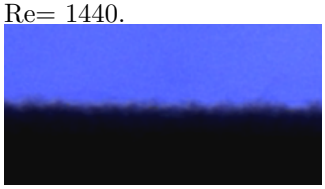

5.7(i): Image I, 20 seconds Re= 743.

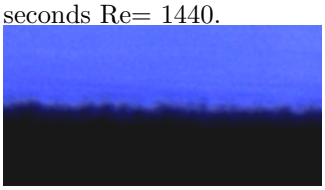

5.7(j): Image J, 35 seconds Re= 743.

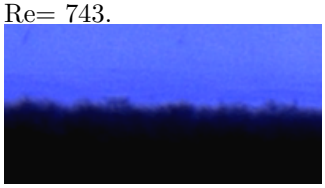

5.7(k): Image K, 60 seconds Re= 743.

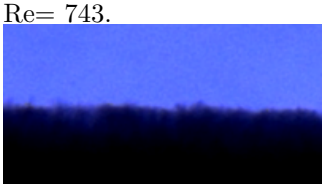

5.7(l): Image L, 300 seconds Re= 743.

Figure 5.7: Deposit–liquid interface images for 20, 35, 60 and 300 seconds after initiation of the deposition experiments. Reynolds number of 2073, 1440 and 743.

### 5.2.2
### Deposit thickness in the annular geometry

In this section the quantitative results for the measured spatial and time evolution of the wax deposits will be presented. As already mentioned the deposition experiments had three durations, one, four and seven hours. The growing of the deposit thicknesses were followed during one hour at positions one to five and seven, according to the diagram of Figure 5.1. During the seven hour tests the camera was at position 6. Three experiment replications were made for each position. The four and seven hour tests were performed with the objective of studying the aging of the deposit, therefore samples of the deposit were taken at specific times, namely, one, four and seven hours. Three samples of each case studied were taken in order to test the repeatability of the samples. The results for the aging studies will be presented in Chapter 8.

#### Steady state regime

In order to determine the steady state regime for the growth of the deposit thickness, the data from long experiments was analysed in three different axial positions of the pipe, for the three Reynolds number studied. The results are shown in Figure 5.8.

As can be verified in the figure, the deposit thickness virtually stopped growing at around 30 minutes for all Reynolds number in positions downstream of 30% of the pipe length. For these cases, with one hour of tests, at least 98% of the final deposit thickness had already been attained. However, for position one, representing only 2% of the pipe length, it is possible to verify in Figure 5.9 that the final thickness is only attained within four hours of test. After one hour of test, for the higher Reynolds number, 87% of the final thickness of the deposit had been attained at position one.

The Reynolds number was calculated based on the hydraulic diameter of the annular geometry. Since the deposit over the internal pipe grows and changes both, the annular space dimensions and the flow average velocity, the Reynolds number also changes during the experiments. Table 5.3 presents the initial and final values of the Reynolds number for each Reynolds number tested. The results of the table show that, although the hydraulic diameter has experienced a significant 66% decrease, the Reynolds number only decreased about 15% from the start to the end of the deposition experiments. A decrease in Reynolds number along the experiments that were initially laminar maintains the flow in the laminar regime. A regime transition during the experiments would certainly turn the interpretation of the results a more complex task.

All the results on the temporal and spatial growth of the deposit thickness that will be presented in the next sections were obtained from experiments with durations of 1 hour. Since a complete experiment involved measurements at seven axial stations with replications at each station, longer deposition experiments, with 4 or 7-hour duration, would be too time consuming, and would make it virtually impossible to conclude this research within a reasonable time frame. The results just presented indicating that at 1 hour a steady state condition had been achieved, supported this decision. However, it should be noted that deposits formed close to the entrance section of the channel still presented variations of the order of 10% at the first hour. Longer experiments were only made for studies related to the deposit aging.

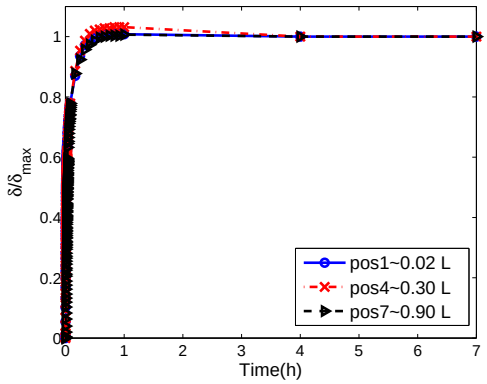


5.8(a):

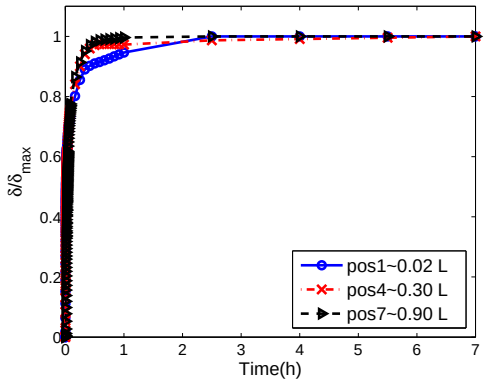


5.8(b):

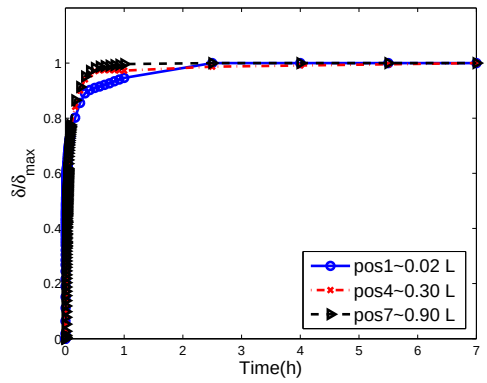


5.8(c):

Figure 5.8: Time evolution of the non-dimensional thickness of the deposit for three Reynolds numbers, (a) Re=743, (b) Re= 1440, (c) Re=2073, at three axial positions.

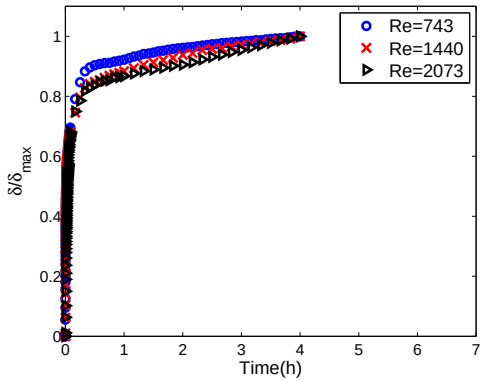


Figure 5.9: Time evolution of the non-dimensional thickness of the wax deposit for Reynolds numbers: Re=743, Re=1440, Re=2073.

Table 5.3: Reynolds number variation.

| **Initial $D_h$** | **Initial Re** | **Final $D_h$** | **Final Re** |
|---|---|---|---|
| 15 | 743 | 5 | 625 |
| 15 | 1440 | 6 | 1231 |
| 15 | 2073 | 6.4 | 1783 |



### Circumferential variations of the deposit thickness

Before the presentation of the results for the time evolution of the deposit spatial distribution a comment on the circumferential symmetry of the measured deposits is necessary.

The images of the deposit formation on the outer surface of the inner copper pipe of the annular test section allowed the simultaneous measurement of the top and bottom parts of the deposit. Indeed, since the image of the clean pipe surface had been captured before the start of the deposition process, the images of the growing deposit and those at steady state, allowed the determination of the top and bottom thicknesses of the deposit. The results of these measurements indicated that the thickness of the deposit was non-uniform, with the bottom deposit being always thicker than the top deposit. Figures 5.10 and 5.11 show the transient evolution of the dimensionless deposit for measurements made at position 6, for Reynolds numbers equal to 743 and 2073, respectively. In each figure, three replications of the experiments are plotted, labelled as top and bottom, 1,2 and 3, respectively. As can be seen in both figures, the deposits are thicker at the bottom part of the pipe. The magnitude of the non-uniformity, defined as $\Delta = \frac{(\delta_{top} - \delta_{bottom})}{\delta_{mean}}$ is of the order of

15%. In Figure 5.12 the axial variation of the deposit non-uniformity is plotted for the three values of Reynold numbers investigated. As can be verified in the figure the magnitude of the non-uniformity does not seem to be a function of the Reynolds number, but a spatial variation is observed in the non-uniformity. Indeed, as it can be noticed from Figure 5.13, there is a reproducible tendency of spatial oscillation of the non-uniformity. This may indicate that there is a possible flow-induced effect influencing the deposition rate. Moreover, from Figure 5.14 it is possible to see that the magnitude of the non-uniformity decreases with time for all the Reynolds number studied.

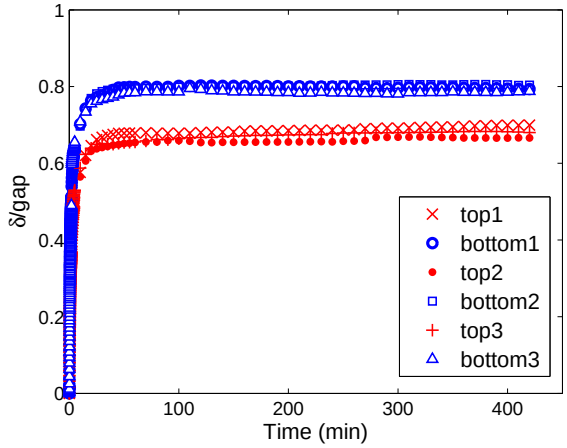


Figure 5.10: Time evolution of the non-dimensional thickness of the deposit during tests with Reynolds number = 743.

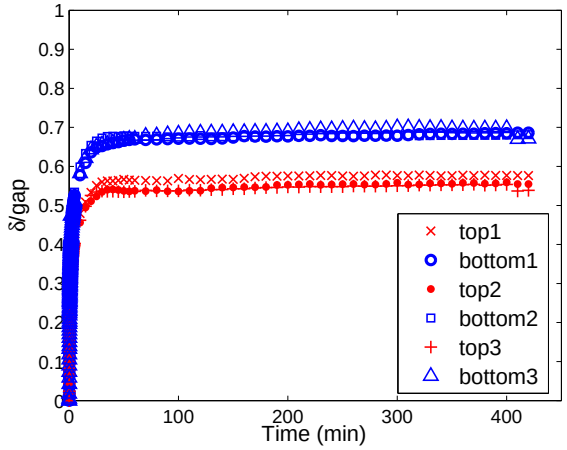


Figure 5.11: Time evolution of the non-dimensional thickness of the deposit during tests with Reynolds number = 2073.

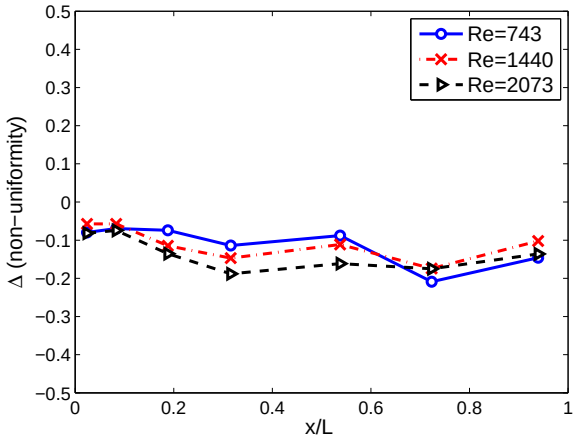


Figure 5.12: Axial variation of the deposit non-uniformity for the Reynolds numbers investigated.

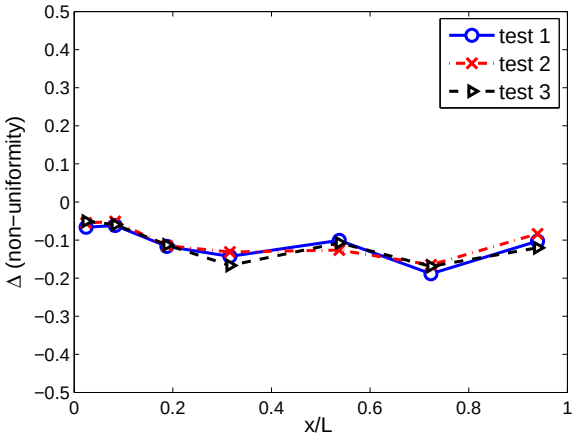


Figure 5.13: Replication tests of the axial variation of the deposit non–uniformity for Reynolds number equal 1440.

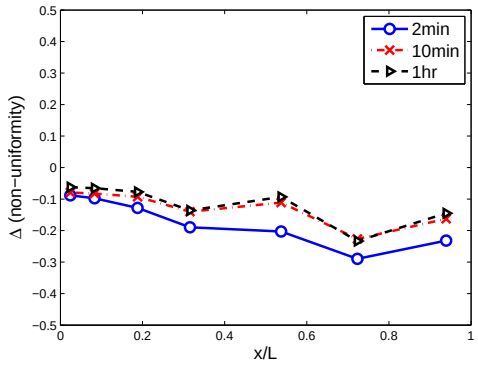


5.14(a):

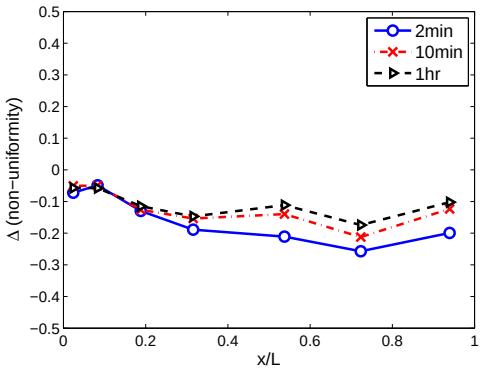


5.14(b):

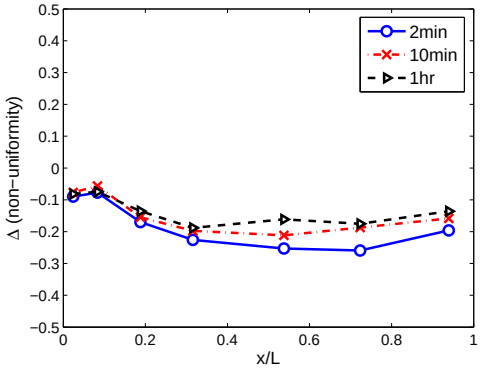


5.14(c):

Figure 5.14: Time evolution of the axial distribution of the deposit non-uniformity for (a) Re= 743, (b) Re= 1440, (c) Re= 2073.

In order to investigate the possible reasons for the observed non-uniformity, additional tests with the camera viewing the test section from the top were conducted. In the current setup, the deposit thickness was measured from the sides of the copper tube. In other words, recalling that the test section is positioned horizontally, these additional measurements yielded information on the deposit thicknesses measured at the East and West positions, that could be compared with the original measurements at the North and South positions. The results from these additional measurements have shown no

difference between the East and West deposit thicknesses. This information is an indication that gravity effects could be playing a role in the North-South non-uniformity observed.

Two possible explanations could be proposed for the gravity-driven non-uniformity. It is conceivable that, at the early stages of the deposition process, the crystals being dragged by the flow close to the pipe wall experience some gravitational effects, once they tend to be denser than the liquid. In this case, at the early stages of deposition, the crystals could slide down along the wall as they were carried by the flow. At latter times, the deposit would present a structured form and the effect would no longer occur. That explanation goes along with the results of Figure 5.14 where the non-uniformity on the deposit thickness is shown to decrease with time.

Another plausible explanation for the deposit non-uniformity is related to natural-convection-induced flow within the annular cross section of the test section. The temperature difference between the colder inner copper pipe and the hotter outer Plexiglas pipe will induce a buoyancy-driven flow formed by two classical counter-rotating, kidney-shaped circulations regions, one at each side of the annular cross section. These recirculation regions will produce a thermal stratification in the annular cross section, with the top portion of the section being warmer than the bottom part. This thermal imbalance could produce a thicker deposit at the colder bottom part of the inner pipe.

Usually when analysing the combined effect of natural and forced convection, as it is the case of the present experiment, the relation between Grashof number and the square of the Reynolds number appears as the relevant dimensionless parameter. When the fraction $\frac{Gr}{Re^2}$ grows natural convection may dominate over forced convection.

The data on Table 5.3 can be used to support the hypothesis of a natural convection effect on the deposit non-uniformity. It was shown in Figure 5.14 that the non-uniformity effect decreased with time for all Reynolds numbers tested. In the table it is shown that there is a small variation in Re from the start of the experiment to the steady state condition. On the other hand, a large variation was observed on the hydraulic diameter of the cross section due to wax deposition. In the Grashof number, the flow properties remain constant along the experiments. The characteristic wall-to-wall temperature difference suffers a small decrease since the initial temperature difference is between the cold copper wall and the hot Plexiglass wall. As the deposit is formed the characteristic temperature difference is between the deposit interface, at the WDT, and the Plexiglass wall. However, the hydraulic diameter drops from 15 to 6 mm, typically. Once the characteristic dimension appears in the Grashof

number raised to the third power, the resulting effect on $\frac{Gr}{Re^2}$ is a typical 20-fold decrease from start of the experiment to the attainment of steady state. The variation of $\frac{Gr}{Re^2}$ relation with time is exhibited in figure 5.15, where it is possible to observe a 600% variation in the relation from 5 minutes to 7 hours. That observation is in agreement with the result of Figure 5.14.

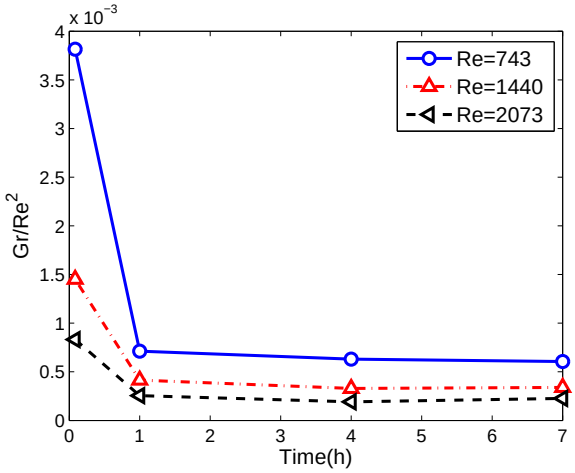


Figure 5.15: Time evolution of the $Gr/Re^2$ relation for Reynolds numbers 743, 1440 and 2073.

It would have been interesting to have flow visualization and quantitative flow measurements to confirm the presence and relevance of the natural convection motions within the annular test section. However, the geometric characteristics of the test section did not allow that these tests were conducted within the available time for this research project. This is a relevant suggestion for further study.

It is worth noting that no mention to these circumferential variations of the deposit thickness was found in the literature, even though several studies have used deposition loops with pipes in the horizontal position and presenting temperature differences between the deposit surface and the bulk fluid of the same order as those employed in the present experiment. The reason for this lack of information may be related to the fact that the techniques used to measure deposit thickness in the studies from the literature were not able to detect circumferential variations of the deposit.

In view of the circumferential variations observed, the results for deposit thicknesses that will be reported next were calculated as an average between top and bottom measurements. This allows the comparison with numerical simulations that used the axi-symmetric hypothesis to solve the relevant governing equations.

### Temporal evolution of the axial deposit distribution

In this section the temporal evolution of the axial distribution of the deposit thickness along the annular test section is presented for the three values of the Reynolds numbers investigated. As already mentioned, these results serve as a data bank for comparisons with simulation models. The low uncertainty levels with which the data were obtained, the good characterization of the simple fluid solution employed, together with the well-defined boundary and initial conditions, make these data a unique source for model testing. Also, other chapters provide additional information on the deposit composition and on the temperature profile within the deposit, that can be used, in conjunction with the thickness data provided here, to form a set of useful information obtained simultaneously from the same experiment source.

Figures 5.16, 5.17 and 5.18 present the measured axial distribution of the deposit thickness for various time instants, ranging from 1 minute to 1 hour. In the figures, the ordinate is the deposit thickness given in dimensionless form relative to the annular gap space,*gap*. The abscissa is the axial coordinate, made dimensionless by the use of the total annular channel length, $L$. Each data point in the figures represents an average value calculated from three replications of the experiments. The error bars, associated with the data points, were estimated based on the uncertainty due to experiments replications, combined with the uncertainty associated with the image processing procedure, employed to determine the deposit thickness from the acquired images.

A general observation of the axial distribution of deposit thickness, for the three Reynolds numbers, show a common trend. Indeed, for the three Reynolds numbers, the growth rate of the deposits is rather fast, with 85% of the steady-state thickness being achieved in the first 10 minutes of the deposition process. This trend is a consequence of the elevated temperature difference between the entering fluid and the cooling wall. This temperature difference was set at approximately $26^oC$, a value much higher than the typical temperature differences encountered in subsea petroleum production systems, where lower deposit growth rates are encountered and reported. Studies on wax deposition under lower bulk-to-wall temperature differences were initiated at the time of the preparation of the present text and were not included here due to time constraints.

The joint observation of the figures reveals the trend of decreasing the deposit thickness with Reynolds number. This trend is well documented in the literature and is a result of the thinning of the thermal boundary layer with increasing Reynolds number. The thinner the boundary layer, the closest is WDT from the cold wall, what limits the deposit thickness, since the WDT is

the maximum temperature at which a solid phase can exist.

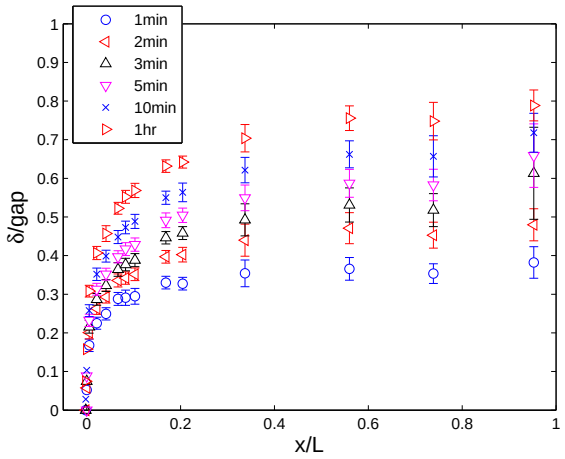


Figure 5.16: Time evolution of the distribution of the deposit thickness for the Reynolds number 743.

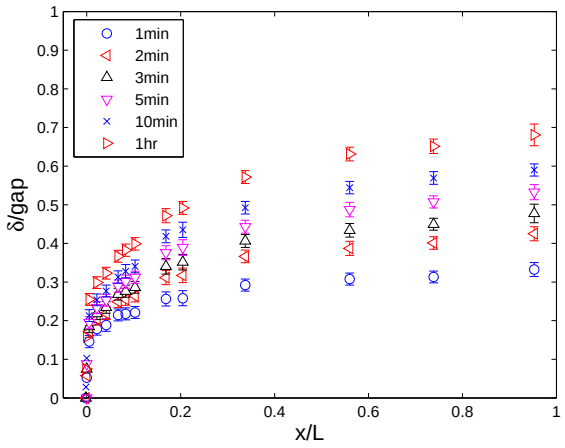


Figure 5.17: Time evolution of the distribution of the deposit thickness for the Reynolds number 1440.

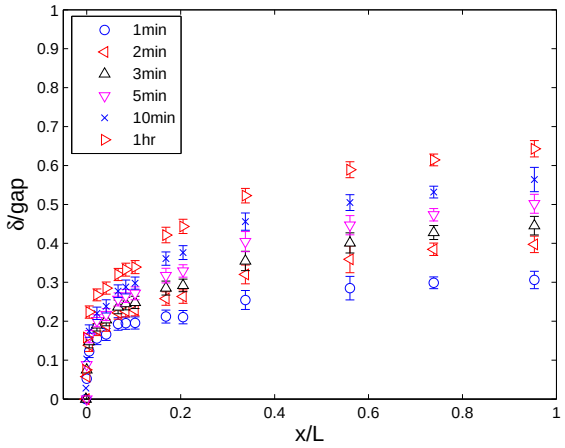


Figure 5.18: Time evolution of the distribution of the deposit thickness for the Reynolds number 2073.

For the lower Reynolds number, Figure 5.16, the deposit thickness is observed to reach a constant thickness at approximately the middle of the channel length, around x/L = 0.50. This developed thickness is reached at the first minute of deposition and is maintained until steady state. As the Reynolds number increases, Figures 5.17 and 5.18, the deposits do not reach the constant developed thicknesses within the available length of the annular channel. This is an expected behaviour, since hydrodynamic and thermal developing lengths are known to increase with Reynolds number.

It should be mentioned, that the smooth variations observed in the curves for the spatial distribution of the deposit thickness are an indication that no shear removal effects occurred during the experiments, for the laminar Reynolds numbers investigated. In fact, a careful observation of deposits individual images confirmed that no wax removal, due to flow shear effects, occurred.

### Comparison between experimental and numerical evolution of the axial deposit distribution

The experimental data, obtained by the present work, was compared to the predicted results from the numerical model, described in Appendix A, and developed by Souza (2014). In the model, the Navier-Stokes equation was employed in the determination of the flow field. One of the main features of this model was the unified treatment of the computational domain, without any separation from liquid flow and solid deposits. As detailed in Appendix A, the momentum equation incorporates a source term controlled by the local value of the solid fraction, what allows the calculation of the flow fields in the bulk, as well as within the porous deposit. By this approach, the flow within

the deposit progressively becomes a Darcy's-type flow, as the solid fraction increases.

Once the model produced solutions for the velocity, temperature, concentration fields, as well as, for the chemical composition and solid fraction fields, the position of the deposit–liquid interface was determined as a post-processing operation, by choosing a specific value for the solid saturation, above which the solution is considered as an immobile deposit layer. In the work by Souza (2014) a value of 2% solid fraction was proposed. This value was based on experimental observations by Holder and Winkler (1965) and Singh and Fogler (1999). The value of 2% was also used in the present work.

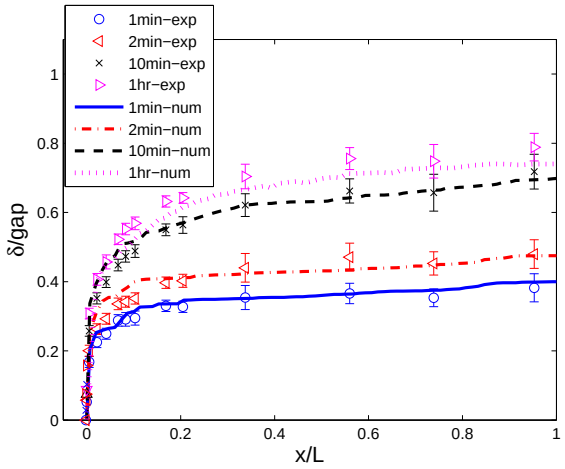


Figure 5.19: Comparison of numerically and experimentally determined time evolution of the axial distribution of the deposit thickness, for Reynolds number of 743.

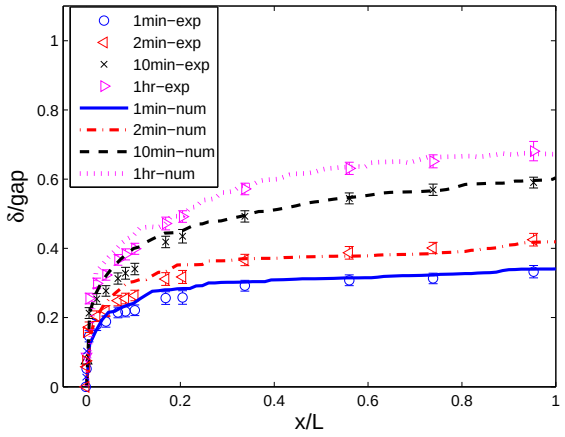


Figure 5.20: Comparison of numerically and experimentally determined time evolution of the axial distribution of the deposit thickness, for Reynolds number of 1440.

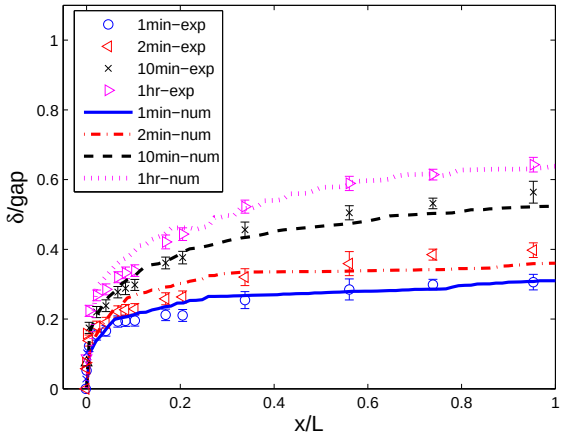


Figure 5.21: Comparison of numerically and experimentally determined time evolution of the axial distribution of the deposit thickness, for Reynolds number of 2073.

Figures 5.19 , 5.20 and 5.21 illustrate the comparison of the experimentally and numerically determined deposit thickness data. The axis used for the figures are similar to those of Figures 5.16, 5.17 and 5.18 - the abscissa represents the axial coordinate made dimensionless by the pipe length and the ordinate is the deposit thickness made dimensionless by the annular gap. The error bars represent the estimate for the experimental uncertainties, as detailed before.

A general observation of the results presented in Figures 5.19 to 5.21 show an excellent agreement between measured and predicted deposition thicknesses. The excellent agreement is observed since the beginning of the deposition process, until steady state is achieved, for all three values of the Reynolds numbers investigated. This level of agreement is remarkable and has never been achieved between our previous experiments, that employed rectangular test sections, and the numerical models employed, that based the growth of the deposit on a molecular diffusion flux calculated at the interface.

Several aspects should be mentioned as being, possibly, responsible for the attained level of the agreement.

Firstly, the quality of the data obtained from the annular test section is considered superior to that of the previous experiments. As already mentioned, the initial and boundary conditions were well defined and controlled, and could be faithfully reproduced in the computational model. In fact, preliminary comparisons were made with the measured cooling history of the wall not being perfectly reproduced in the model. The resulting predictions for the early deposition times did not agree well with the measured data. After that, the modelling of the transient evolution of the wall temperature was improved,

especially at the initial transient, yielding the excellent results for the early times that can be observed in the figures just commented. This fact is an indication of the importance of heat transfer to the deposition process.

The negligible heat losses from the annular test section were also considered as having influenced the quality of the agreement. Heat losses in previous employed rectangular test section were not negligible and difficult to be properly modelled. Also worth mentioning is the simple test solution employed with well-characterized properties, what allowed the use of more accurate correlations in the simulation.

Finally, the numerical model employed in the present study is considered more sophisticated than the previous ones. The thermodynamic calculation incorporated in the model is a significant improvement over the models that consider phase equilibria via an experimentally determined solubility curve, valid only for the initial composition. However, a definitive assessment of the performance of different thermodynamic calculations and deposition models, using the good-quality data presented here, is yet to be performed and is a suggestion for future work.



It should be mentioned that the numerical model developed and used in the present comparison incorporates two parameters that require adjustment to the data. The first of them is the threshold solid fraction value that defines the deposit–liquid interface boundary. As mentioned previously, the value of 2% of solid fraction was considered as a proper limiting value based on information from the literature. An interesting observation is that the same value of solid saturation, 2%, yielded excellent agreement with the experimental data in the transient, as well as in the steady state regime for all flow conditions tested. As stated before, in the beginning of the deposition process, wax crystals appear close to the cold pipe, but they do not form a deposit until a certain solid saturation is attained. It is interesting to note that the same critical solid saturation is valid for different wall shear conditions, represented by the channel Reynolds number. This result indicates that, for the range of Reynolds numbers investigated, the critical solid saturation is not a function of the prevailing flow conditions as suggested before.

The second parameter incorporated into the model is related to the packing of the deposit. In the model by Souza (2014), a morphology coefficient was employed in the source term of the Navier-Stokes equation, controlling the effect of the solid saturation on the momentum equation, leading to a Darcy's flow in the porous deposit. The morphology parameter was adjusted to the experimental data, yielding a value of $C = 10^9 m^{-2}$. In the work of Hoteit et al. (2008), however, the adjustment of this parameter to the experimental

data yielded a value of $C = 10^6 m^{-2}$. This difference may be attributed to the different cooling rates employed in the two studies. While in the present study a steady state deposit thickness was obtained after about 1 hour, in their work 24 hours were required. Higher cooling rates tend to form smaller crystals and, since $C$ is inversely proportional to the size of the crystals, a higher value of $C$ is expected to fit the data obtained under higher cooling rates, which is the case of the present work. Further studies on the value of this morphology parameter seem to be necessary.

## 5.3 Conclusions

The present chapter presented results from deposition experiments conducted in the annular test section, under laminar flow conditions.

The careful design of the test section and the use of a simple and well characterized test solution yielded quality data for the transient evolution of the wax deposit thickness axial distribution. Three different values of the Reynolds number were tested. Results were obtained since the early stages of the deposition process, until steady state conditions of the deposit thickness were reached.

Qualitatively, observations of the early stages of the deposit formation were made, indicating that wax crystals first appear close to the cold surface of the pipe when the surface reaches the WAT, and are convected by the flow. An immobile deposit layer is formed once a certain wax crystals solid saturation is attained. A cloud of flowing crystals still existed over the deposited layer at the first instants of the immobile layer formation. It was observed that the crystals cloud was denser for higher values of the Reynolds number, which could indicate an effect of the thinning of the thermal boundary layer between the liquid–deposit interface temperature and the WDT isotherm.

Experimental results for the deposit thickness temporal and spatial evolutions were compared with the predictions of the computational model, developed in a previous study. The comparisons yielded an excellent agreement, from the early stages of the deposition process to the attainment of steady state. The numerical model employed two adjusting parameters, maintained constant for all cases tested.

The experimental results obtained in the present work will serve as a data bank to test different deposition models and their building hypothesis. There are several available models that can benefit from the high-quality data presented here. Comparisons with these models is part of an ongoing work in our group.

# 6
# Temperature profile within the wax deposit

The experimental setup constructed as part of the present research program allowed obtaining information on the temperature distribution within the wax deposit. Measurements of temperature profiles within the wax deposit seem to be an original contribution to the literature on wax deposition. Not only this information might be useful to validate simulation models that account for heat and mass transfer within the deposit, but could also be used as an indirect tool to access the nature of the transfer processes, within the deposit, as will be shortly described.

The process of growth of the wax deposit layer has been described by several authors (Burger et al. (1981); Singh et al. (2000, 2001a); Venkatesan et al. (2005); Merino-Garcia et al. (2007); Banki et al. (2008)). Typically, it is assumed that, as the temperature is lowered, wax molecules form stable crystals that will eventually pack, forming a structured gel that becomes immobile while growing. In the work of Holder and Winkler (1965), it was shown that wax crystals that precipitate out of solution form thin plates that overlap and interlock, entrapping a considerable amount of liquid. Indeed, some authors state that as little as 2% of solid wax is necessary to form a gel (Holder and Winkler (1965); Singh and Fogler (1999)). Based on this observations, the wax deposit has been described as a porous medium, with the liquid phase filling the pores (Burger et al. (1981); Singh et al. (2000); Merino-Garcia et al. (2007); Banki et al. (2008)).

The knowledge of the controlling heat and mass transfer processes, within the porous deposit, is still a subject of study. A better understanding of the transfer mechanisms controlling heat and mass transfer in the deposit is important to properly model the deposit growth and aging. The majority of the models available in the open literature consider that heat and mass transfer in the deposit are governed solely by diffusion. According to this assumption, molecular diffusion transports the lighter molecules present in the liquid phase out of the deposit and the heavier wax molecules into the deposit (Singh et al. (2000)). Seemingly, Banki et al. (2008) were the first to model the flow inside the deposit, while describing it as a porous medium. The authors stated that

a convection radial flux could play an important role in the deposit formation. Bidmus and Mehrotra (2004) have also suggested that flow of liquid wax could be present within the deposit layer, decreasing the resistance to the passage of a heat flux, when compared to that offered by pure conduction.

The measurement of the temperature profiles across the wax deposit may be a way of indirectly accessing the relative importance of the transfer mechanisms in the deposit. Pure conductive heat transfer in the deposit is associated with a linear temperature profile, in case of a one-dimensional heat transfer in a Cartesian geometry. Logarithmic temperature profiles are expected if pure conduction prevails in a one-dimensional cylindrical geometry. Deviations from these expected purely conductive temperature profiles could be associated with the presence of liquid flow within the deposit induced by the bulk flow of the solution over the deposit interface. Buoyancy-induced flows in the porous deposit are also a possibility due to the temperature gradient imposed on the wax deposit layer.

In the present study, measurement of the temperature profile across the wax deposit were undertaken in both, the rectangular and annular, test sections described in chapter 3.



## 6.1 Results for the temperature profile: rectangular channel test section experiments

The experimental procedure employed for the temperature profile measurements, in the rectangular test section, was similar to that employed for measuring wax deposit thicknesses, in the annular test section, described in Chapter 5.

In preparation for a deposition experiment, the desired flow rate was set at the pump controller, while the flow loop was maintained in thermal equilibrium at $38^oC$ ($\pm 0.2^oC$), by circulating warm water, from the thermostatic bath through the heat exchanger, under the lower wall of the test section. The solution in the test tank was maintained at $38^oC$ by the heated plate and homogenized by the magnetic agitator. The heating tapes, mounted around the hoses conducting the solution, were activated in order to keep them warm and avoid wax deposition. A standby chiller had its water in equilibrium at $5^oC$. To start the deposition experiment, a fast change in the the valves of the water circuit was made, so that water from the standby chiller replaced the hot water stream, in the heat exchanger. This procedure generated a fast reduction of the bottom wall temperature until its surface attained $12^oC$, a temperature that was maintained up to the end of the deposition experiment.

The cooling ramp obtained for the rectangular test section experiments is exhibited in Figures 6.1 and 6.2. The cooling ramp exhibited in the figures is an average ramp for at least three experiment replications. The average uncertainty in the wall temperature results based on the experiments replication was $\pm 0.25^{o}C$. It is possible to verify that the cooling ramps are very similar for the two lower Reynolds numbers, but for the highest one a somewhat higher deviation is observed. The highest average difference between the curves is of $\pm 0.35°C$. It is important to recall that the cooling system was operating at its limit, i.e. at the higher cooling rate possible.

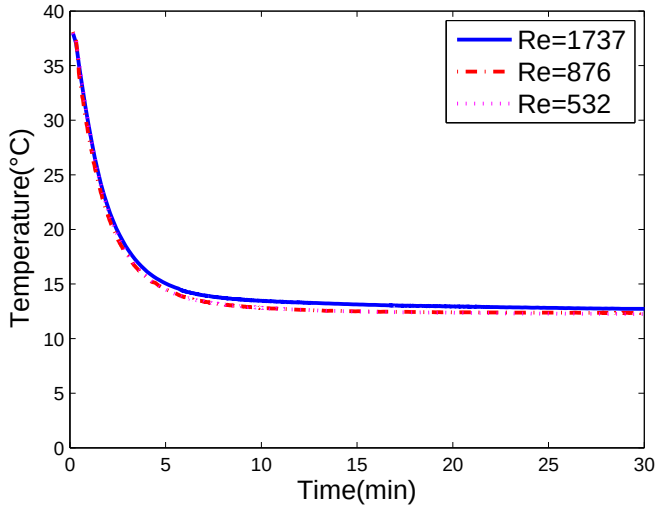


Figure 6.1: Cooling ramp imposed in the deposition experiments performed with the rectangular test section.

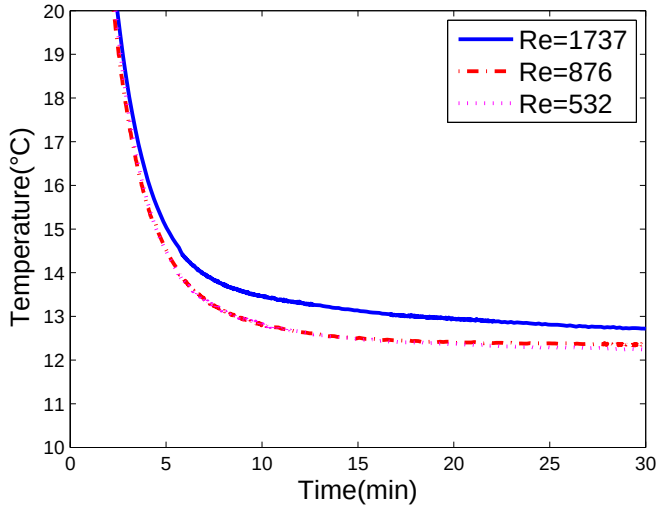


Figure 6.2: Expanded view of the time variation of the stainless steel wall temperature.

The Reynolds numbers calculation, made for the rectangular test section, was similar to the one employed in the annular test section, described in Chapter 5. The calculation was based on the average velocity of the flow, on the hydraulic diameter and on the properties of the wax solution, as exhibited in Equation 6-1.

$$Re = \frac{\rho \bar{V} D_h}{\mu} = \frac{\rho \; Q/A \; (2wh/(w+h))}{\mu} \tag{6-1}$$

where $\rho$ and $\mu$, are the density and dynamic viscosity, at $38^oC$, of the wax solution, based on WAX1, obtained from the data in Chapter 4. $\bar{V}$, the average velocity, is the flow rate divided by the cross–sectional area; where $Q$ is the flow rate and $A$ is the area of the cross–section. In rectangular geometries, the hydraulic diameter is reduced to $2wh/(w+h)$ where $w$ is the width of the channel and $h$ is its height.

At specific time instants - five minutes, one, four and seven hours from the beginning of the cooling process - the traversing thermocouple probe was used to measure both, the thickness of the deposit and the temperature profile inside the wax deposit layer.

As described in chapter 3, the top part of the rectangular test section was equipped with a traversing thermocouple probe. A schematic view of the probe is reproduced in Figure 6.3 to facilitate the description and interpretation of the temperature profile results, that will be presented shortly. The range of displacement of the probe was of 13 mm, which was enough to span the height of the test section.

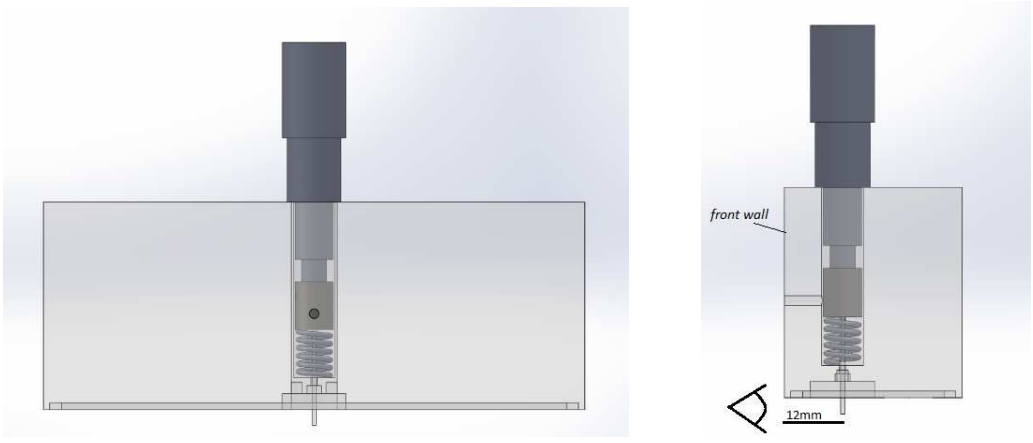


6.3(a): 6.3(b):

Figure 6.3: (a) Front and (b) lateral views of the traverse thermocouple probe mounted in the top wall of the channel.

At the beginning of the experiment, the probe tip was retracted and positioned flush with the upper wall of the channel, in order not to disturb the flow in the channel. After five minutes from the start of the

cooling process, a visible deposit was formed on the bottom wall of the test section. The temperature probe was then quickly lowered, by manually turning the micrometer head screw until the sensing thermocouple junction reached the deposit–liquid interface position. The interface position was detected by visually verifying that the thermocouple junction had just disappeared inside the deposit. From Figure 6.3 (b) it is possible to notice that the probe was installed off-center, at only 12 mm away from the front wall of the test section. That distance was chosen to be sufficiently far from the side wall hydrodynamic effects and to allow a good visual access to the thermocouple junction position through the channel side wall.

As the probe was being lowered, its temperature data was registered by the data acquisition system. From the deposit–liquid interface, the probe was inserted inside the deposit layer in steps of one probe diameter - 0.2 mm. The probe was maintained at each vertical position for 10 s. During that time interval, 10 temperature measurements were acquired, since the data acquisition rate was set at 1 Hz. Temperature profile measurements for deposition times less than 5 minutes were not attempted, due to the fast growth rate of the deposit thickness verified at this early stages of the deposition process.

The spatial position of the probe junction, at each step of the temperature profile measurement, was registered by reading the micrometer barrel. The first measured position, at the deposit–liquid interface, was used as a measurement of the deposit thickness. The last position was obtained when the the thermocouple junction touched the lower wall. As already explained in chapter 3, the touching of the wall was detected by sensing an electrical short between the thermocouple junction and the wall surface.

The possibility that warm liquid from the flowing bulk solution entered into the deposit, as the thermocouple probe penetrated the deposit, was considered. To analyse this possibility, samples of the deposit, at the region where the probe penetrated, were removed after four intrusions of the probe. These samples were analysed by HTGC and compared with samples of the deposit, obtained from experiments without the intrusion of the probe. The analysis indicated the presence of 3% more solvent in the case of the samples obtained after the intrusion of the probe. However, these results should be compared with the experimental uncertainty level for the analysis of the samples, which was estimated to be of the order of $\pm 7\%$. The sampling analysis uncertainty was estimated based on the removal of five samples from seven-hour deposits formed in a flow with Reynolds number 1737. The uncertainty was calculated based on the mean deviation of these data. The

results indicate that the difference found in the deposit composition with and without the presence of the probe was smaller than the estimated sampling analysis uncertainty, leading to the conclusion that the introduction of the probe was not associated with an undesired inflow of warm liquid solution.

An alternative way to assess the possible intake of hot fluid while inserting the thermocouple probe is to look at the temperature probe raw time data. These data were registered as the probe was being inserted into the deposit. As already mentioned in the experimental procedure, the probe was inserted and maintained for 10 seconds at any particular positions, and then inserted by an additional amount. Typical temperature records obtained for three values of the Reynolds number and three deposition times are displayed in Figure 6.4. The observation of the temperature records show horizontal lines representing constant temperature at the 10-seconds waiting period, before the probe was moved further down into the deposit. Had warm liquid been admitted during the probe insertion, a temperature raise would have been observed. These results confirm that the probe insertion procedure did not admit a significant amount of warm fluid. As will be commented in the presentation of the results, for some operational conditions of the annular test section, unexpected results were obtained and attributed to flow-induced motion of the temperature probe.



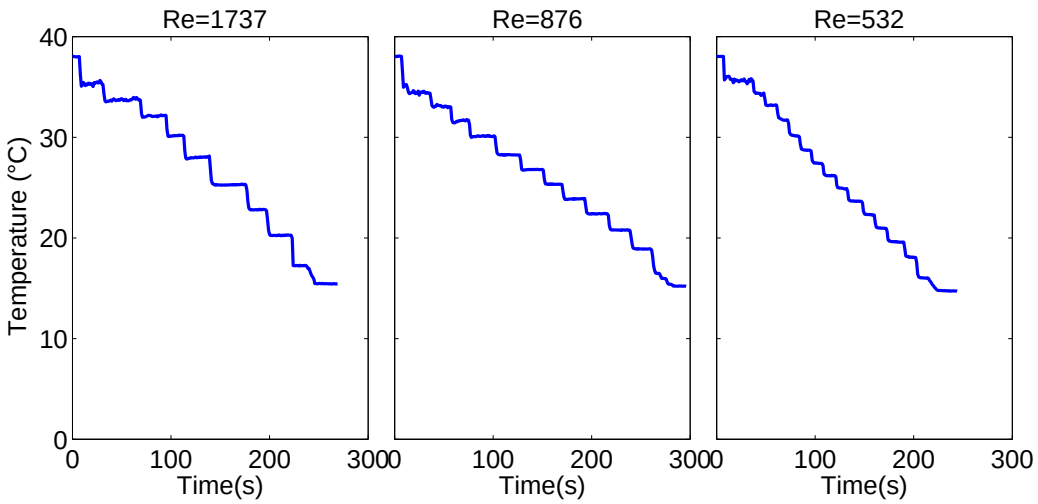


Figure 6.4: Time variation of the temperature measured by the thermocouple probe as it was inserted into the wax deposit. Data for five minutes tests for the three Reynolds number: 532, 876, 1737.

Measurements of temperature profiles within the deposit were made for three flow rates, corresponding to Reynolds numbers of 532, 876, 1737, and for four time intervals counted from the initiation of the deposition, namely,

five minutes, one, four and seven hours. For every case, a repetition of at least three experiments was undertaken, to assess the repeatability of the data.

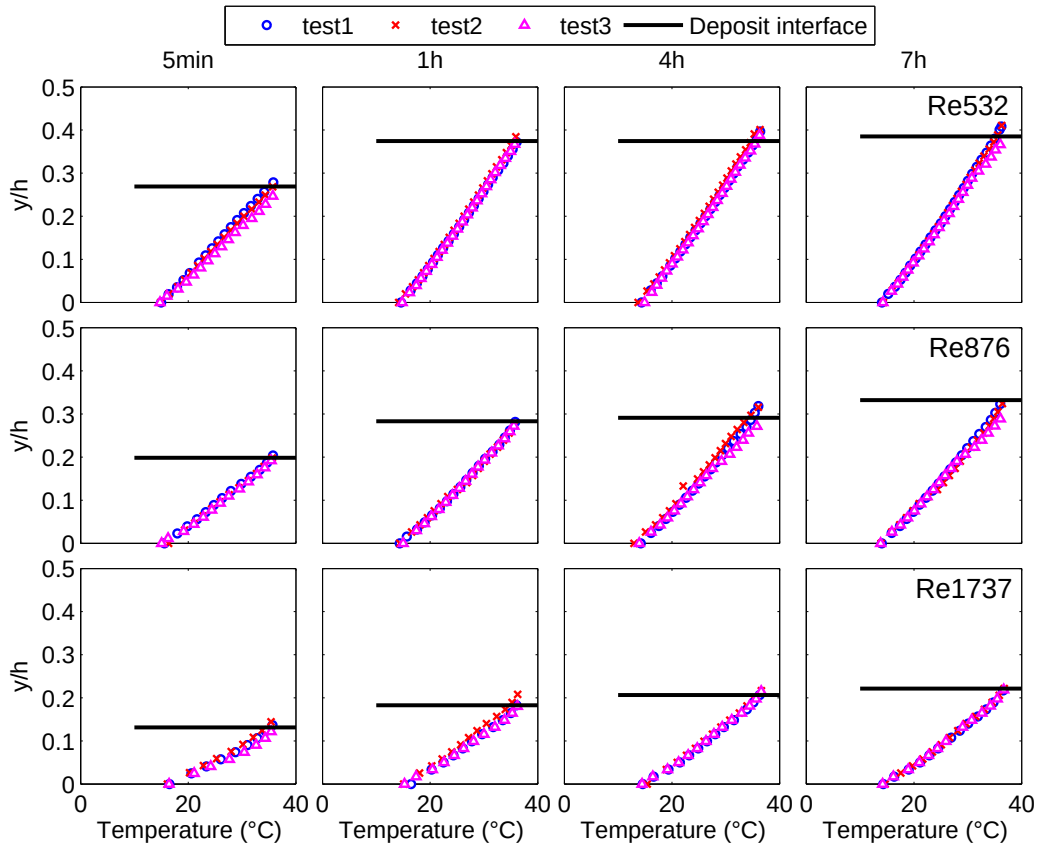


Figure 6.5: Temperature profiles inside the deposit layer from the rectangular test section experiments, for three Reynolds number: 532, 876 and 1737.

An overall view of the measured temperature profiles is presented in Figure 6.5. In the figure, the temperature profiles for each Reynolds number are presented along the horizontal lines, with the value of the Reynolds number indicated in the right-most plot. The time intervals in which the profiles were measured are in the vertical columns. In each plot, the ordinate is the transverse coordinate made dimensionless by the channel height, $h$, while the abscissa is the temperature in $^oC$. The zero vertical position is at the lower wall. In each plot, the solid line represents the position of the interface, measured by registering the position of the thermocouple junction when it touched the interface, as already explained. The symbols with different colors are related to the three replications conducted for each experiment, and are labelled as test 1, 2 and 3.

Although this joint presentation of the results, for all measured times and Reynolds numbers, offers a good general view of the temperature profiles relatively to the deposit thicknesses, it does not allow a detailed analysis of their behaviour and comparison with the purely-conductive analytic solution.

To facilitate the analysis, the results of Figure 6.5 are plotted again in Figures 6.6 to 6.11 using an enlarged scale, for each Reynolds number and time of measurement.

Figures 6.6 and 6.7 display the results for Reynolds number 532 and for the four time intervals after the initiation of the wall cooling, 5 min, 1, 4 and 7 hours. The data are presented in dimensionless form, with the abscissa representing the difference of the measured temperature in the deposit in relation to the wall temperature, normalized by the interface-to-wall temperature difference. The ordinate is the transverse coordinate made dimensionless by the channel height. Each graph corresponds to the time interval indicated. The different symbols are related to the three replications of the experiments, as already commented. Also plotted in the graphs, are lines representing the linear temperature profiles obtained from the analytic solution of the one-dimensional Cartesian heat conduction equation. The linear profiles were calculated considering a constant value for the thermal conductivity inside the deposit layer, and using the deposit–liquid interface and the wall temperatures as boundary conditions. The calculation was also made using a linear variation of the deposit thermal conductivity with temperature, based on available n-alkane data, and no significant differences in the temperature profiles were observed between the two approaches. Based on this analysis, the constant thermal conductivity assumption was employed.

The data from different experiments replications plotted in Figs 6.6 and 6.7 present a very good level of agreement, indicating that the results obtained have a good level of repeatability. Estimates of the uncertainty levels associated with the temperature measurements were obtained by combining the thermocouple calibration uncertainty, with the standard deviation of the temperature records, and the uncertainty associated with the probe size. This last component of the uncertainty was the dominant one, even though the probe could be considered small with a size of approximately 0.2 mm. The highest estimated total uncertainty on the temperature profile measurements was of $\pm 14\%$ for the highest Reynolds number case.

An analysis of the results presented in Figs 6.6 and 6.7, for Reynold number equal to 532, show that the measured temperature profiles for all times are in good agreement with the linear profile, predicted by the purely-conductivity solution. This is an indication that no noticeable convective transport is induced by the bulk flow on the porous deposit, for this lower value of the Reynolds number investigated.

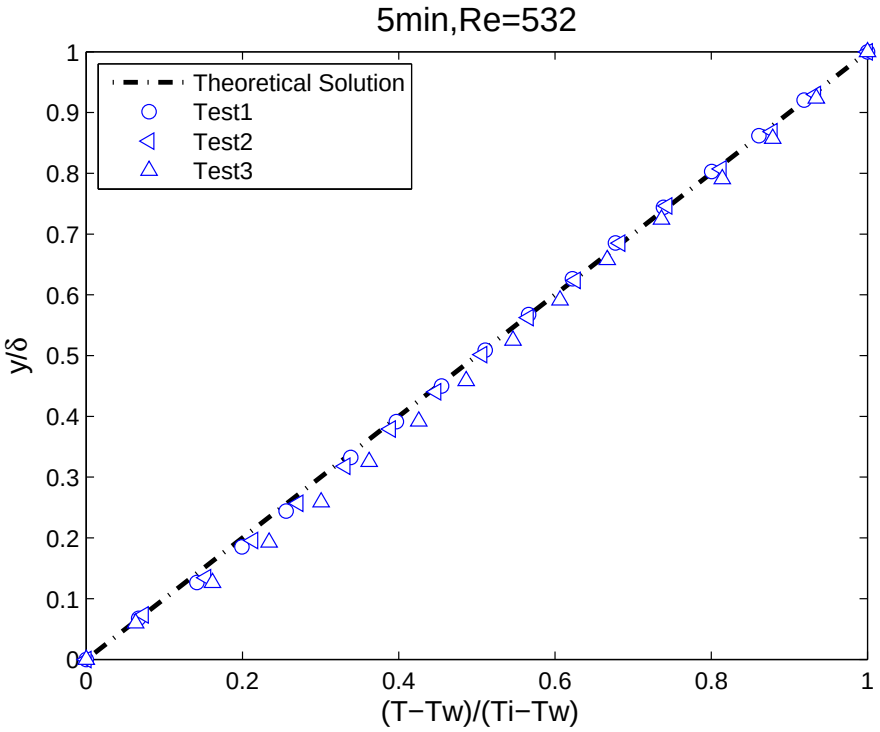


6.6(a):

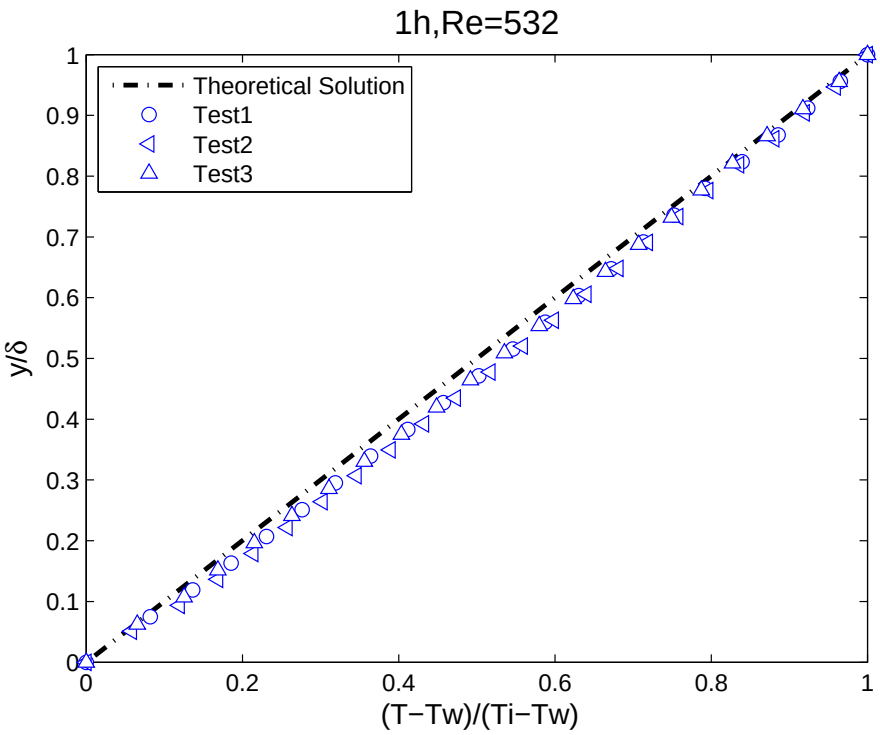


6.6(b):

Figure 6.6: Dimensionless temperature profiles measured during flow with Reynolds number equal to 532, at (a) 5 minutes and (b) one hour from the beginning of cooling.

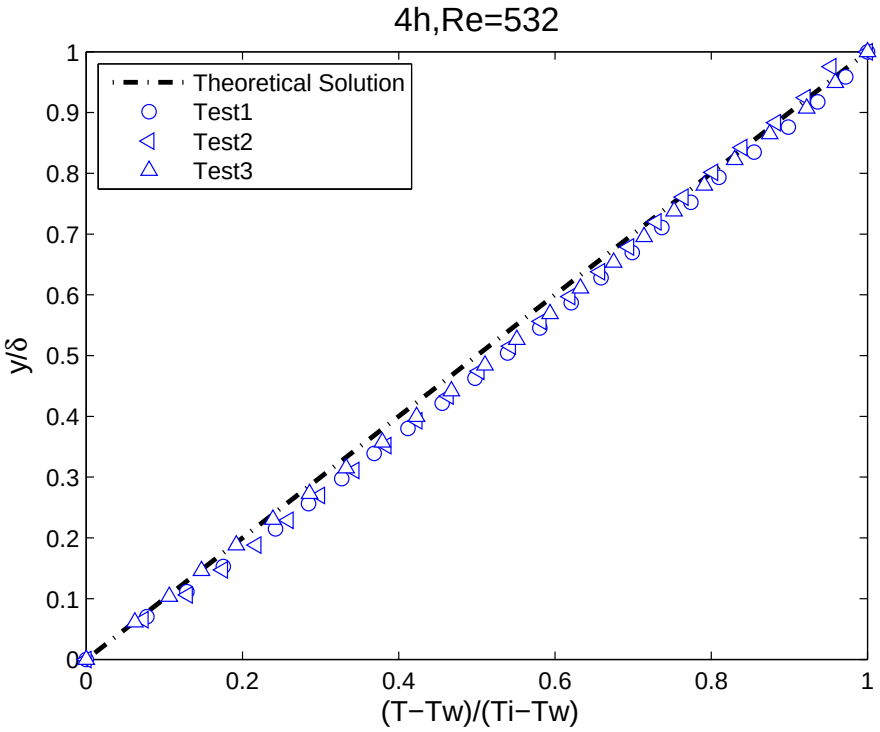


6.7(a):

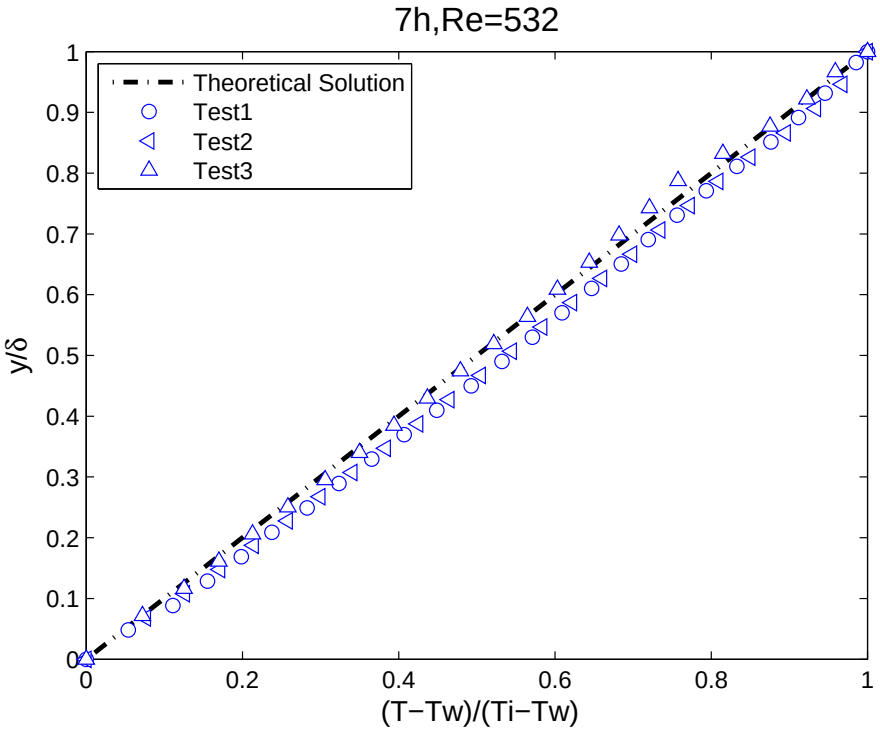


6.7(b):

Figure 6.7: Dimensionless temperature profiles measured during flow with Reynolds number equal to 532, at (a) four hours and (b) seven hours from the beginning of cooling.

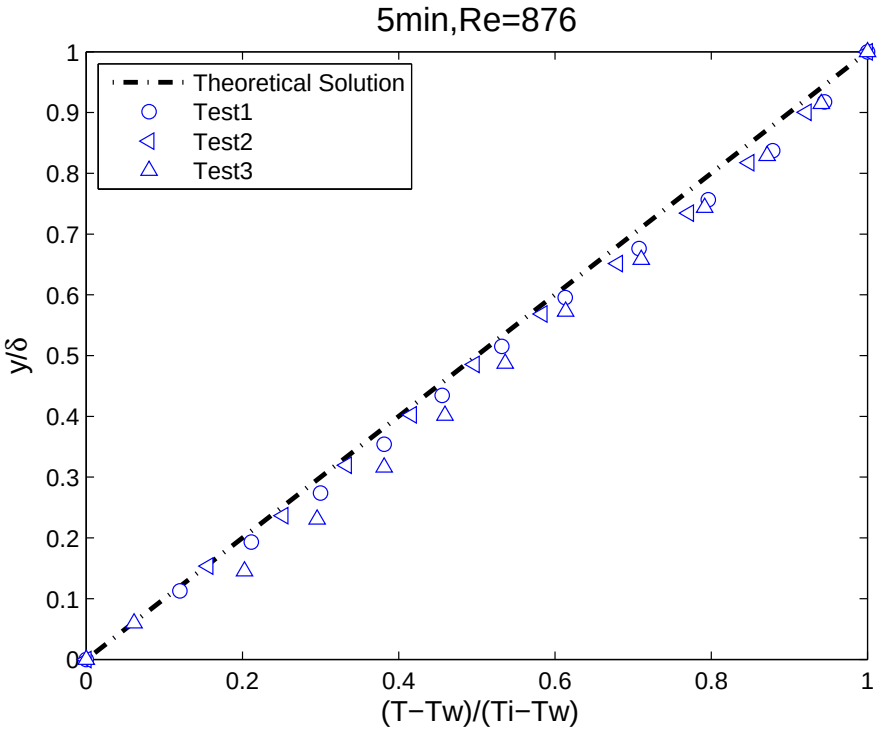


6.8(a):

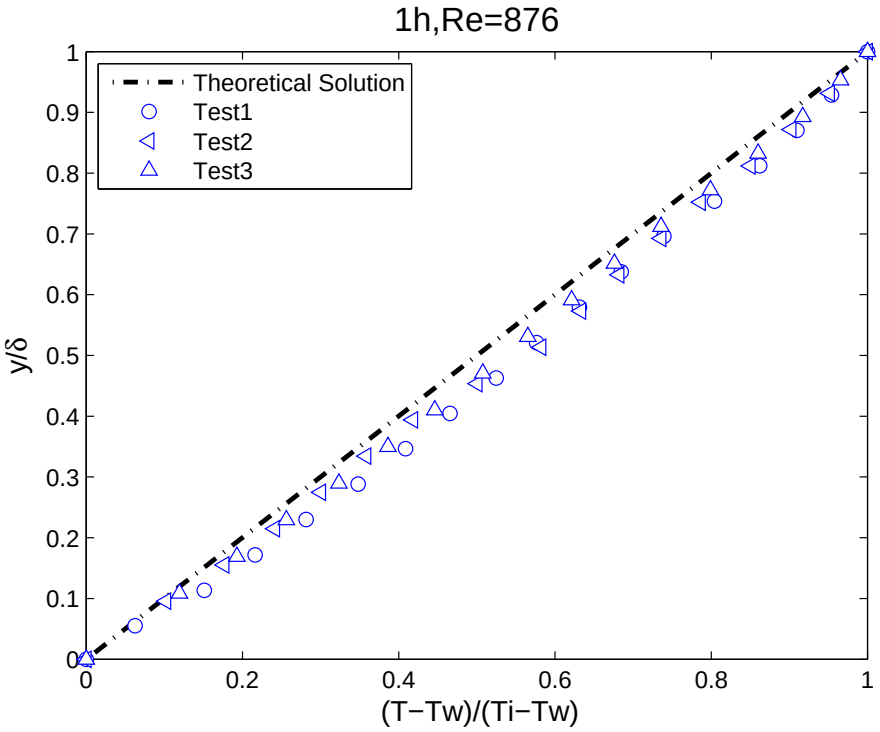


6.8(b):

Figure 6.8: Dimensionless temperature profiles measured during flow with Reynolds number equal to 876, at (a) 5 minutes and (b) one hour from the beginning of cooling.

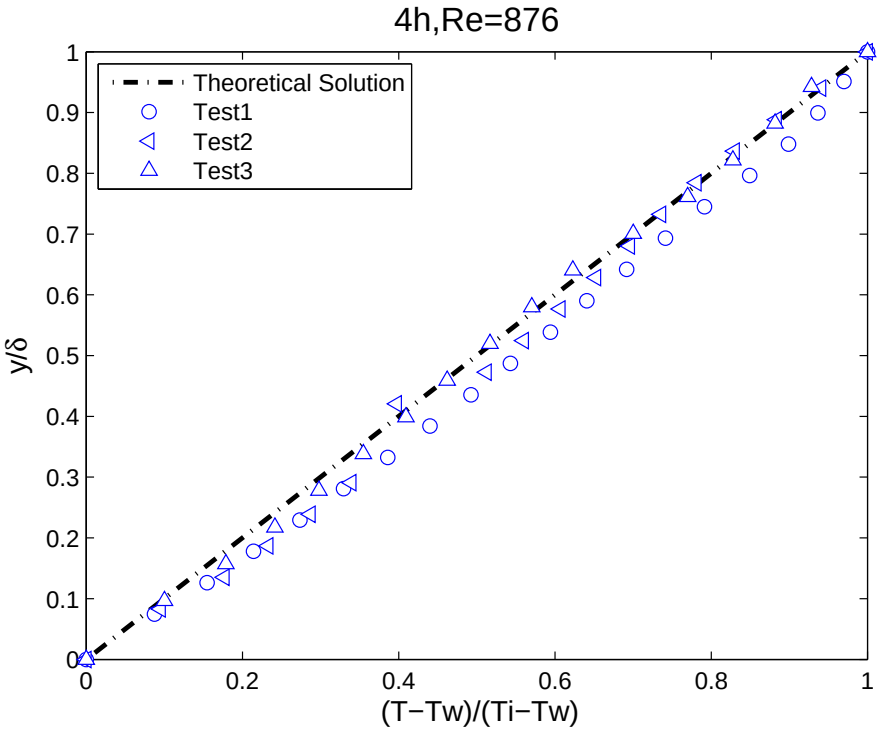


6.9(a):

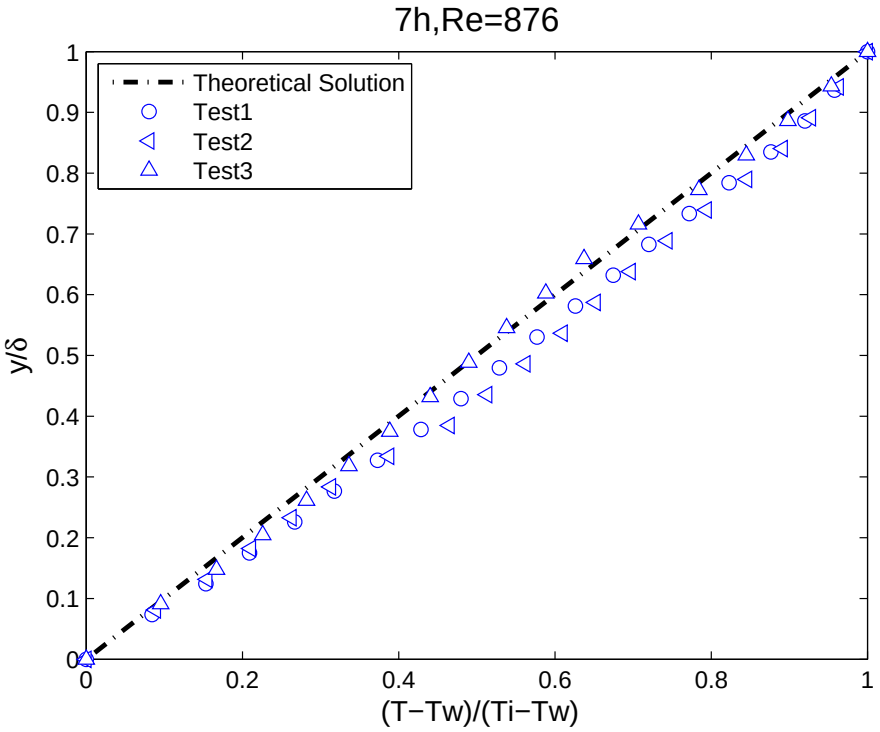


6.9(b):

Figure 6.9: Dimensionless temperature profiles measured during flow with Reynolds number equal to 876, at (a) four hours and (b) seven hours from the beginning of cooling.

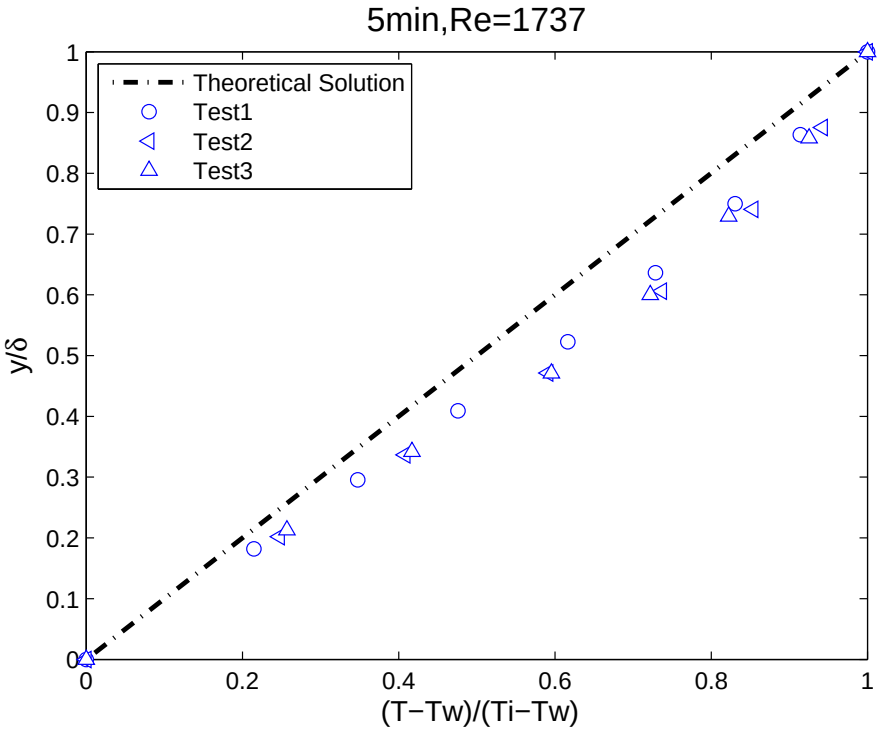


6.10(a):

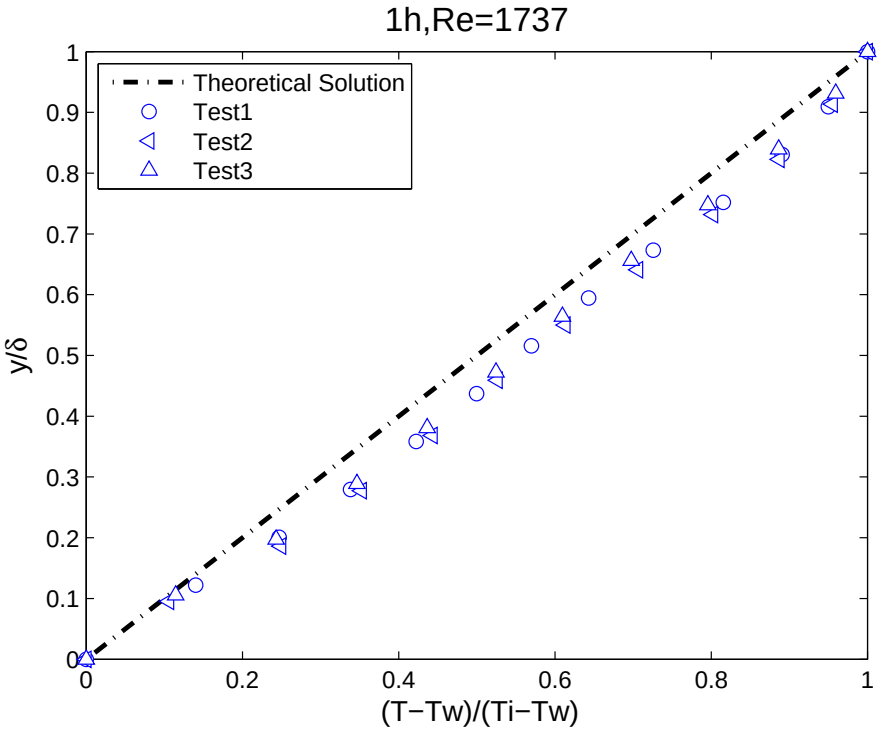


6.10(b):

Figure 6.10: Dimensionless temperature profiles measured during flow with Reynolds number equal to 1737, at (a) 5 minutes and (b) one hour from the beginning of cooling.

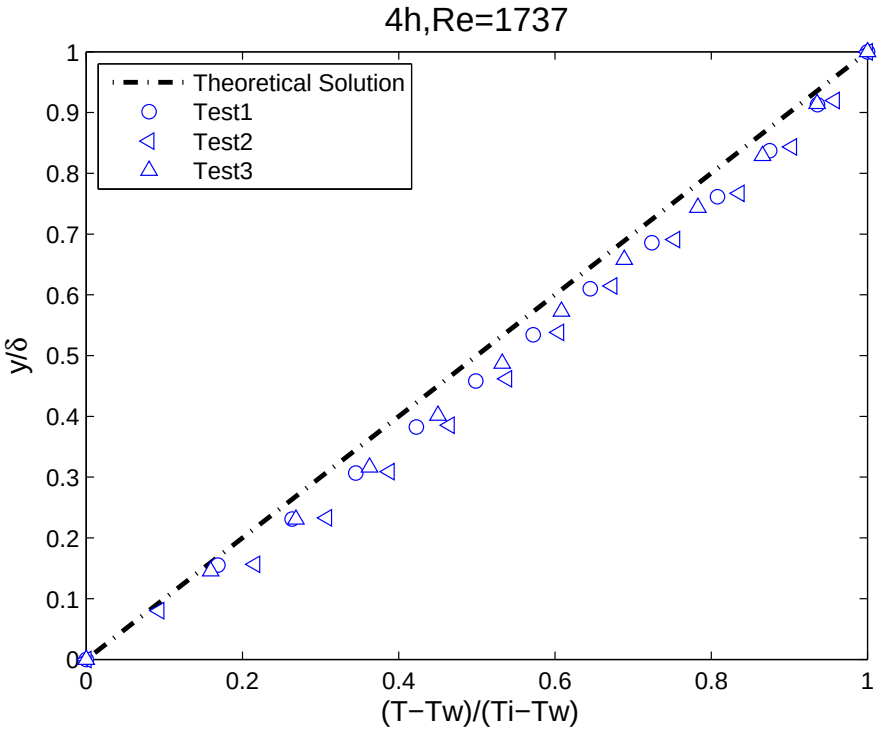


6.11(a):

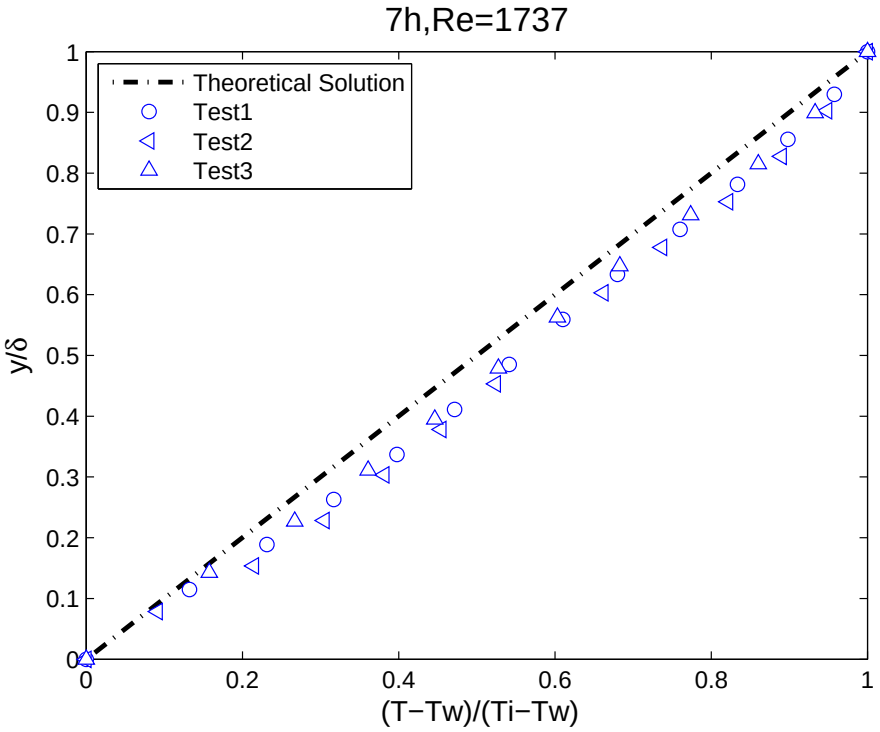


6.11(b):

Figure 6.11: Dimensionless temperature profiles measured during flow with Reynolds number equal to 1737, at (a) four hours and (b) seven hours from the beginning of cooling.

However, as the Reynolds number is increased to 876 and 1737, a

departure from the linear behaviour is observed in the temperature profiles. This departure is more pronounced for the early deposition times and higher values of the Reynolds numbers, as can be verified by a careful observation of the results of Figs 6.8 to 6.11. Indeed, it can be seen that the measured temperature data points closer to the interface display a temperature above that predicted by the linear profile, obtained from the conduction solution. These warmer regions can, conceivably, be associated with liquid flow in the porous deposit matrix induced by the bulk flow shear at the deposit interface. As the deposition time is increased, the deposit is expected to be less permeable, offering a higher resistance to the shear-induced flow at the interface and, as a consequence, the temperature profile returns to the linear conductive solution. Or, as it is going to be mentioned in chapter 9, these differences may be associated to a non-uniform thermal conductivity inside the deposit layer.

As mentioned in the introduction paragraph of the present chapter, the results presented here seem to be the first investigation on the temperature profiles, within the wax deposit, measured under flowing conditions. The results indicate the possible contribution of convective transport to the deposit formation and aging. The conclusions drawn from the results obtained for short deposition time experiments might have been influenced by the higher levels of experimental uncertainties, that prevail at these early deposit stages, when the thickness of the deposit is small compared to the size of the temperature probe. Also associated to the short deposition times, the uncertainties due to the transient process must be considered, since the deposit was still growing at these early stages. Further investigation employing other methodologies, specially conceived for the transient times, are recommended as a future line of research.

For completeness, the time evolutions of the deposit thicknesses are presented in Table 6.1. These thickness data were obtained by imaging the position where the thermocouple junction just entered the liquid–deposit interface. As can be verified in the table, the deposit thickness grows rapidly with time, with approximately 40% of the deposit thickness been achieved in the first 5 minutes of deposition. Also, the deposit thickness, for the lower Reynolds number, was found to have reached its steady state thickness, with a difference of only 0.5% between the values measured at 4 and 7 hours. For higher values the Reynolds number, slight variations of the order of 3 and 7% were measured between the 4 and 7-hour thicknesses, respectively for Reynolds 876 and 1737. However, it should be mentioned that these variation are of the order of the experimental uncertainty found for the data. Table 6.1 also

presents the expected uncertainty in the thickness data. The uncertainty levels were estimated based on the probe resolution, given by its diameter, and on the mean deviation observed in the replication of the data.

Table 6.1: Time evolution of the deposit thickness measured in the rectangular test section.

| | Time instant | Deposit thickness (mm) | Uncertainty ($\pm mm$) |
|---|---|---|---|
| **Re=532** | | | |
| | 5 min | 3.28 | 0.16 |
| | 1 h | 4.57 | 0.15 |
| | 4 h | 4.72 | 0.14 |
| | 7 h | 4.70 | 0.25 |
| **Re=876** | | | |
| | 5 min | 2.42 | 0.14 |
| | 1 h | 3.45 | 0.14 |
| | 4 h | 3.92 | 0.19 |
| | 7 h | 4.05 | 0.31 |
| **Re=1737** | | | |
| | 5 min | 1.60 | 0.23 |
| | 1 h | 2.23 | 0.30 |
| | 4 h | 2.52 | 0.17 |
| | 7 h | 2.70 | 0.28 |



## 6.2
## Results for the temperature profile in the annular channel test section

The idea for measuring profiles in the annular test section was motivated by the fact that the annular test section was more carefully designed, and presented a better control of thermal and hydrodynamic conditions, as compared to the rectangular test section. Unfortunately, as will be commented shortly, the performance of the temperature traversing probe, installed in the annular section, was unexpected for certain values of the Reynolds number. These unexpected behaviours did not allow a proper assessment of the possible presence of flow, within the deposit porous matrix, induced by the shear from the bulk flow, at the interface. Nevertheless, it is believed that the present results offer an interesting topic for discussion.

The experimental procedure for the temperature profile measurements, in the annular test section, was the same as that described in Chapter 5, for

the deposition experiments. Briefly, before the initiation of a data run, the flow loop was maintained in thermal equilibrium at $38^oC$ ($\pm 0.2^oC$),by circulating the warm solution through the annular section and maintaining the water in the outside tank, involving the test section, at the same temperature. After thermal equilibrium was attained, a data run was initiated by changing the settings of the valves, controlling the flow of water, in such a way as to direct cold water to the interior of the inner copper pipe, forming the annular channel. The surface temperature of the copper pipe was reduced to $12^oC$, following the cooling ramp presented in figure 5.2. Wax deposition was then initiated on the copper surface.

At specific time instants - five minutes, one, four and seven hours - the traversing thermocouple probe was used to measure the temperature profile inside the deposit layer.

The thermocouple traversing probe port is exhibited again in Figure 6.12 to facilitate the description and interpretation of the results. The probe port was positioned at 0.8 of the tube length, measured from the fluid inlet plane, as mentioned in Chapter 3. The digital camera that recorded the time evolution of the deposit thickness, inside the annular channel, was positioned at 50 mm upstream from its center, so as to image a region adjacent to the probe holder. Previous deposition experiments have demonstrated that at this axial position, far from the entrance plane, the deposit interface was horizontal, within experimental uncertainty. That fact guaranteed that the deposit thickness, measured by the digital camera, was the same as that at 50 millimetres downstream, where the thermocouple probe was located and not visible by the camera. It should be mentioned, however, that the test section was originally designed to allow for the visualization of the junction of the thermocouple probe by the digital camera, in a similar way as it was done for the rectangular test section. Unfortunately, due to construction limitations, the material employed to hold the traversing probe, around the Plexiglass pipe, could not be fabricated from a fully transparent material, what precluded the imaging of the thermocouple junction.

At the beginning of the experiment, the thermocouple probe tip was retracted and positioned flush with the outer wall of the annular channel, so as not to disturb the flow. When the deposit was formed, at the four specific time instants mentioned before, the micrometer barrel was manually turned, lowering the probe thermocouple junction toward the deposit interface. The reading of the thermocouple was monitored while the probe was lowered and the first deviation of $38^oC$, from the bulk flow temperature, was taken as indication of the approaching interface. After this point, the thermocouple

probe was lowered in steps of one probe diameter - 0.2 mm.

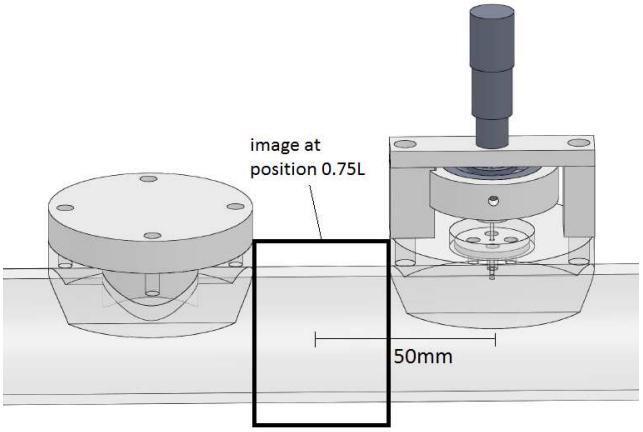


Figure 6.12: Camera field of view adjacent to the thermocouple probe for measuring the deposit-liquid interface temperature in the annular test section.

At least 10 temperature points were taken for each position of the probe, which took at least 10 seconds at each position, since the reading frequency was of 1 Hz.

The zero position of the probe - when it touched the external surface of the inner copper pipe - was set by sensing an electrical short between the probe and the wall, as described before in chapter 3.

The temperature profile inside the deposit layer was measured for three Reynolds number, 743, 1440, 2073 and four time instant: 5 minutes, one, four and seven hours. At least three repetitions of each case were performed, in order to test the data for repeatability.

Figure 6.13 shows the results of the temperature profile across the wax deposit layer, measured in the annular test section. In the figure, the time instants of measurement are indicated on the top of each column of plots, while the different Reynolds numbers are organized by lines and are indicated in the right-most plots. In each plot of the figure, the solid line represents the position of the deposit interface at that specific time instant. The dashed line represents the temperature profiles obtained by the exact solution of pure conduction, across the annular geometry. The analytical solution is a logarithmic-type solution, considering constant thermal conductivity, and using the deposit–liquid interface and the wall temperatures as boundary conditions.

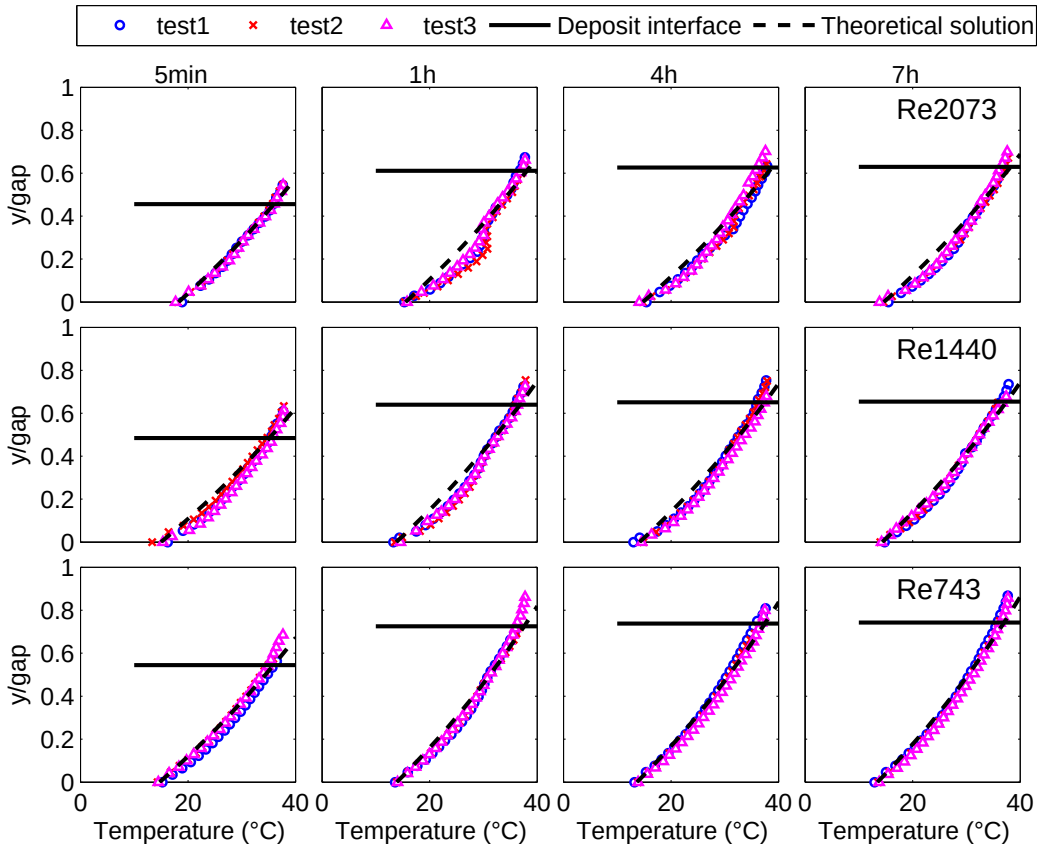


Figure 6.13: Comparison of experimental and theoretical temperature profile measured in the annular test section.

An overall inspection of the experimental data, plotted in Figure 6.13 for all time instants and Reynolds numbers investigated, show an excellent agreement between data from different replications of the experiments. This is an indication of the good repeatability of the data.

For the profiles measured at five minutes after the initiation of the wax deposition, the presented results show an excellent agreement with the theoretical solution profiles for all values of the Reynolds numbers. As already mentioned, the logarithmic profiles derive from the exact purely-conductive solution, so that the agreement between the measured and predicted profiles indicate that conduction dominates the heat transfer process within the wax deposit, and that convective transport does not seem to play a significant role, for this early stages of deposition. In fact, the good agreement between experiments and the purely-conductive logarithmic solution is verified for Re = 743 for all times.

Attention is now turned to the analysis of the data for 1 hour after the initiation of the deposition and for Reynolds number equal to 2073. The measured profile in the deposit displays an unexpected S-shaped profile, with a sharp change in inclination at about the mid-deposit-thickness position.

Several replications of this experiment were conducted yielding the same shape of the profile with a high degree of reproducibility. This unexpected change in the inclination of the temperature profile is also found for other times and Reynolds number values, although less pronounced.

The reasons for these anomalous behaviours could be attributed to flow induced in the deposit, but also to some problems with the performance of the temperature probe, installed in the annular test section.

The temperature probe is a 1-mm-diameter cylinder fixed at one end to the micrometer head, and with the other end, the measuring junction, penetrating into the deposit. The probe cylindrical glass stem is subjected to a cross flow induced by the bulk flow in the annular channel. The mean velocity of the bulk flow increases with time as the deposit thickness increases and partially blocks the annular cross section. Cylinders in cross flow are known to be subjected to flow-induced vibration for certain ranges of the cylinder-based Reynolds number. According to Williamson (1988) and Fey et al. (1998), the range of Reynolds numbers where vortex shedding is significant is from 50 to 180. The Reynolds numbers based on the probe diameter were estimated for the different values of the annular channel Reynolds numbers investigated. It was found that for the annular channel Reynolds number of 743, the probe Reynolds number varied from 36.7 to 30.4, bellow the vortex shedding regime. However, for the 1440 and 2073 Reynolds number cases, the probe Reynolds number varied from 71.1 to 59.9 and 102.4 to 87.3, respectively, values well within the range where vortex shedding is expected.

In case the probe oscillated laterally due to vortex shedding, warm fluid could, conceivably, penetrate into the deposit, occupying the space on the deposited wax, opened by the motion of the probe, generating the distortion observed in the temperature profile. The intensity of this effect would be controlled by several parameters, such as the bulk flow velocity and the stiffness of the probe. The stiffness of the probe would depend on the exposed length of the probe and on the resistance offered by the deposit to be dragged by the probe tip. Aged deposits would hold the probe junction better. Under the proposed scenario, the experimental conditions formed by Reynolds equal to 2073 and a deposit formed after 1 hour seem to maximize the probe motion. Unfortunately, due to constructive limitations, the test section did not allow the direct visualization of the probe tip by the digital camera, what would demonstrate if the probe was indeed undergoing lateral motion. At the time of the preparation of the present text, a new test section was being constructed, with a design that will allow the direct visualization of the probe tip.

Due to the possible problems presented by the temperature probe, the

analysis of the relative importance of conduction and convection within the deposit, based on the comparison of experiments and the exact logarithmic solution, could not be properly conducted. This analysis was delayed until this issue is resolved.

## 6.3 Conclusion

The present chapter described experiments where, seemingly for the first time, temperature profiles were measured within the wax deposits under flowing conditions. Experiments where conducted employing two different test section geometries, rectangular and annular.

The results for the rectangular test section indicated the possibility of flow within the porous deposit matrix, induced by the bulk flow shear at the deposit-liquid interface. This conclusion was reached by comparisons between the measured profiles and the linear temperature profiles expected for a purely-conductive heat transfer regime in the deposit. Departures from the linear profile were more pronounced for higher values of the Reynolds number, but also in regions close to the interface and at the early stages of deposit formation.

The experiments employing the annular test section were not conclusive due to an anomalous behaviour, found in the measured temperature profiles for certain operating conditions. This behaviour was attributed to a problem with the temperature probe performance, due to flow induced vibration. Further studies need to be conducted to settle this issue and to allow the proper interpretation of the results, for the temperature profiles, within the deposit formed in the annular test section.

# 7
# Deposit–liquid interface temperature

## 7.1
## Introduction

A relevant piece of information, for understanding and modelling the wax deposit formation process, is related to the temperature of the deposit–liquid interface. The models available in the open literature differ significantly in the treatment given to the interface temperature. Even if, these differences may not lead to significant quantitative differences in the predicted deposit thickness, they are associated with fundamental physical issues that remain unresolved.

The most widely employed deposition model is the diffusion-based model. There are research groups that believe there is already sufficient evidence to consider molecular diffusion of wax in solution as the dominant deposition mechanism. For instance, a author states that *among these mechanisms, molecular diffusion has been shown to be the dominant process in wax deposition* (Huang et al. (2011)). In our view, however, there is not enough evidence to support such conclusion, and there is still need for further research in the field.

With different degrees of simplification in the governing equations, the diffusion-based models solve the mass, momentum, energy and species concentration equations for the flow in a pipe (Banki et al. (2008); Huang et al. (2011)). The inlet fluid is generally warmer than the outside cold environment, leading to heat transfer from the fluid to the ambient, through the pipe wall. If the temperature of the wall is lower or equal to the WAT, there will be crystal nucleation at the wall. The crystals grow and interlock forming a gel-like structure that constitutes the initial stage of the wax deposit. The energy equation is solved, taking into account the additional thermal resistance imposed by the presence of the deposited layer, and the temperature at the deposit–liquid interface is calculated. The equilibrium concentration of the solution, at the interface, is determined with the knowledge of the interface temperature and the solubility curve for the solution. This value, of the solution

concentration at the interface, serves as boundary condition for the solution of the species concentration equations, leading to the species concentration fields. At this point, in the calculation procedure, an important and controversial hypothesis is made: if the temperature of the interface is below the WAT, the diffusion flux at the interface is calculated by Fick's first law, based on the gradient of the concentration field at that location. This diffusion flux of dissolved wax is then part converted into an increment to the deposit thickness and part diffused into the deposit, increasing its solid content, by means of a counter-diffusive process, whereby light components diffuse out of the deposit, characterizing what is known as the ageing process. The calculation procedure just described is repeated for subsequent time instants, until the deposit–liquid interface temperature reaches the WAT. At this time, the deposit growth is stopped, reaching its steady state thickness axial profile. Although the deposit has reached its steady state thickness configuration, diffusion of wax components through the deposit may continue, as the deposit ages.

Bhat and Mehrotra (2004) proposed a model, for predicting the wax deposit evolution, assuming that the deposit growth was controlled solely by heat transfer. It is basically a phase change model where the energy equation is solved for the fluid, deposit and pipe wall resistances. In this model, the interface temperature is assumed to be always equal to the WAT, and an energy balance at the interface controls the deposit growth by considering the solidification enthalpy. The fact that the deposit–liquid interface evolves at a constant temperature equal to the WAT is supported by experiments conducted by the same group (Bidmus and Mehrotra (2008a,b)). This fact is used by the authors as an argument to criticize the diffusion-based models, which consider that the deposit–liquid interface temperature increases constantly during the deposition process, reaching the WAT only when the deposit reaches its steady state configuration.

In the present studies, deposition experiments were conducted under controlled conditions, with the objective of contributing to the study of the deposit–liquid interface temperature. The interface temperatures were measured for both the rectangular and annular test sections, for three values of the solutions Reynolds number and for a single value of cooling rate.

## 7.2 Measurements of WAT and WDT for flowing conditions in the rectangular channel test section.

Prior to presenting the results for the deposit–liquid interface temperature, it is interesting to report the observations performed in the rectangular

test section, regarding the temperature of appearance of the first crystal and the temperature of disappearance of the last wax crystal, on the deposition wall, i.e., the WAT and the WDT. These observations were made for different values of the Reynolds numbers and compared with the values obtained from the CPM measurements, reported in Chapter 4.

Optical measurements of the WAT and WDT are normally performed with a small sample of the solution, positioned on a microscope table, with temperature control capability. The sample is housed in a small glass holder and the detection of the temperature of appearance of the first crystal or disappearance of the last crystal is made under static or no-flow condition.

The rectangular test section developed for the present study allows the measurement of the WAT and WDT for the situation where the solution in flowing. To this end, the following procedure was employed.

The solution was pumped through the rectangular test section with a flow rate that would produce the desired value of the Reynolds number for the test to be performed. The temperature of the solution and that of the bottom wall of the channel were set at the same values, above the expected WAT for the solution. The attainment of the steady state condition was monitored by the readings of the thermocouples, installed in the wall and in the bulk of the fluid, as described in Chapter 3. After steady state, cold water was pumped through the heat exchanger, attached to the bottom channel wall, producing the lowering of the wall temperature at a prescribed cooling rate.

The transparent side walls of the rectangular test section allowed for the visual observation of the wall surface. As the wall temperature dropped, the first crystal appearing on the surface could be easily identified by visual observation, in the form of a small bright spot on the surface. At the moment of observation, the reading of the wall temperature was registered at the data acquisition system. As the wall continued to cool, several other crystals appeared covering the surface. At this point, the flow of cold water to the heat exchanger was reverted to hot water, initiating the heating phase of the wall. Visual observation allowed spotting the last shinning crystal on the wall. The temperature of the disappearance of the last crystal was registered at the data acquisitions system. These two temperatures were associated to the WAT and WDT, respectively.

These observation experiments were conducted for three values of the Reynolds number, namely, 532, 1737 and 3632. Three replications were performed for each test condition conducted.

Table 7.1 presents the results obtained from the experiments conducted and just described. The temperature experimental uncertainties reported in

the table were estimated by combining the uncertainty associated with the calibration of the thermocouples, with that associated with the standard deviation of the temperature time series, registered by the data acquisition system. An analysis of the result presented in the table indicates that, within the estimated uncertainty levels, there is virtually no effect of the Reynolds number on either the temperature of appearance or disappearance of the crystals.

Table 7.1: Fist appearance and last dissolution temperatures measured during flow.

| Re | First appearance ($°C$) | Last dissolution ($°C$) |
|---|---|---|
| 532 | 34.24 ±0.20 | 36.25 ±0.31 |
| 1737 | 34.35 ±0.26 | 36.16 ±0.24 |
| 3632 | 34.55 ±0.36 | 36.86 ±0.25 |

The results from Table 7.1 are plotted in Figure 7.1. In this figure the values for the WAT and WDT measured under static conditions using the microscope are also plotted as solid lines. Dashed lines in the figure indicate the expected uncertainty levels for these measurements. As can be seen in the figure, for the levels of uncertainties associated with the experiments, the crystal appearance and disappearance temperatures measured for different Reynolds numbers coincide with the WAT and WDT measured under static conditions in the microscope.

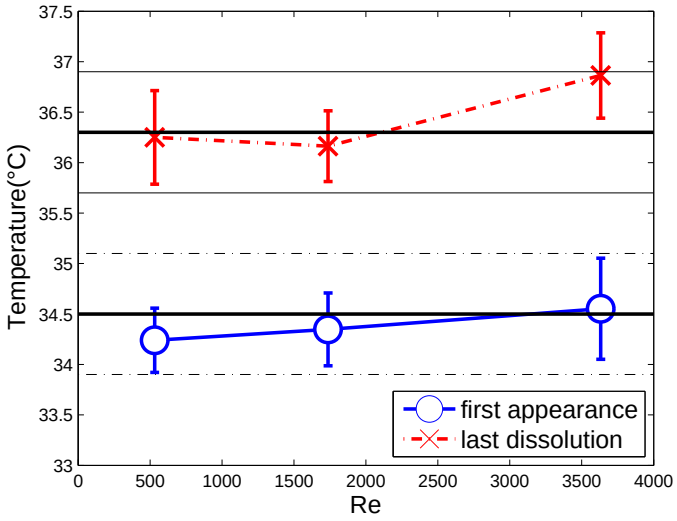


Figure 7.1: Temperatures for appearance of the first crystal and dissolution of the last crystal measured under flowing conditions for different Reynolds numbers.

Since the WDT is believed to represent the thermodynamic phase change temperature, the *liquidus* temperature, it is reasonable to expect a constant value, irrespective to the hydrodynamic conditions of the experiment, as observed. However, the WAT is associated with the degree of sub-cooling necessary to form the first crystal and could be influenced by different levels of shear stress imposed by the flow. The insensitivity to Reynolds number observed in the experiments is an interesting finding. It should be mentioned that the experiments were conducted at cooling rates varying from 8.5 to 10 $°C/min$, calculated based on the first minute wall cooling ramp. Other cooling rates may present different dependence of the WAT with the Reynolds number, however they were not tested in the present work due to time limitations.

## 7.3 Results for the deposit–liquid interface temperature: rectangular channel test section experiments

We now turn our attention to the experiments conducted for measuring the deposit–liquid interface temperature. The experimental procedure employed in the experiments will now be described.

The temperature probe, described in Chapter 3, was employed for measuring the interface temperature. At the beginning of the experiment, the probe tip was retrieved, positioned flush with the upper wall of the channel. The flow rate of the solution was set at the pump controller to yield the desired value for the Reynolds number. The inlet temperature of the solution and the lower wall temperature were set to equal values above the WAT, namely $38°C$. After attainment of the steady state condition, cold water was pumped through the heat exchanger attached to the lower wall, initiating the cooling of the wall. After five minutes from the starting of the cooling of the lower wall, a visible deposit was formed. The probe was then quickly lowered, by manually turning the micrometer screw, until the probe sensing tip reached the interface position. The positioning of the probe at the interface was determined by visually verifying that the thermocouple tip had just penetrated the interface. The temperature of the probe was constantly been registered by the data acquisition system. The probe was left at the interface position for 10 s and then quickly removed to its rest position at the upper wall of the channel. During the time interval that the probe was at the interface, 10 temperature measurements were acquired, since the data acquisition rate was set at one measurement per second. Interface temperature measurements for times less than 5 minutes were not attempted due to the fast growth rate of the deposit thickness verified at this early stages of the deposition process. A different experimental technique

was devised to study the interface temperature at these early stages, whereby the thermocouple tip would be positioned at a fixed distance from the wall and the deposit would sweep through it as it grew. Camera images and temperature measurements would be registered simultaneously in a synchronized mode. This alternative technique was not implemented in the present work due to time constraints.

The procedure just described of probing the interface temperature and retrieving the thermocouple probe was repeated for different times after the initiation of the wall cooling, namely, 5 min, 1, 4 and 7 hours.

The configuration of the temperature probe employed could potentially lead to temperature errors, since it is basically a cylinder in cross flow, exposed to a hot stream, that could conduct heat to the thermocouple probe tip, positioned at the interface. An estimate of this systematic error was performed employing the analysis based on the work by Hennecke and Sparrow (1970). As can be seen in the sample calculations presented in Appendix B, the estimate for systematic errors yielded negligible values for the Reynolds numbers employed in the rectangular test section.

Interface temperature values were obtained for the time instants mentioned above, for three values of the Reynolds number based on the clean channel hydraulic diameter, namely, 532, 876 and 1737. The cooling ramp imposed is exhibited in Figure 6.1. The average cooling rate at the first five minutes was of $4.5°C/min$. The solution with a WAT of $34.5°C$ entered the channel with a temperature of $38°C$, while the lower wall was cooled down to $12°C$.

Table 7.2 presents the interface temperature data, measured for the four time instants, and for each value of the Reynolds number. The table also displays the estimated uncertainty on the interface temperature measurements. These estimates were obtained by combining the thermocouple calibration uncertainty, with the standard deviation of the temperature records. It should be mentioned that each temperature value reported in the table represents an average value, from 6 replications of each deposition experiment.

Table 7.2: Time evolution of the deposit–liquid interface temperature for different Reynolds numbers for the rectangular channel test section.

| | **Interface Temperature** | | |
|---|---|---|---|
| | Time instant | Temperature ($^{\circ}C$) | Uncertainty ($\pm^{\circ}C$) |
| **Re=532** | | | |
| | 5 min | 35.68 | 0.79 |
| | 1 h | 36.05 | 0.58 |
| | 4 h | 36.19 | 0.57 |
| | 7 h | 36.35 | 0.56 |
| **Re=876** | | | |
| | 5 min | 35.48 | 1.00 |
| | 1 h | 35.67 | 0.94 |
| | 4 h | 36.15 | 0.94 |
| | 7 h | 36.26 | 0.98 |
| **Re=1737** | | | |
| | 5 min | 35.45 | 1.64 |
| | 1 h | 36.00 | 1.07 |
| | 4 h | 35.32 | 1.07 |
| | 7 h | 35.44 | 1.07 |



The results presented in Table 7.2 can be better interpreted in graphical form. Figure 7.2 presents the deposit–liquid interface measured for Re equal to 532. The interface temperatures are reported for 5 min, 1, 4 and 7 h after the initiation of the deposition experiment. Also presented in the figure are the deposit thicknesses, measured at the same time instants for which the interface temperature measurements were taken. The temperature values are referenced to the left ordinate, while the deposit thickness data are referenced to the right ordinate, given in terms of a fraction of the channel height, $h$. Also shown in the graph for reference purposes are two horizontal lines representing the values of the WDT and WAT measured for the solution using microscopy.

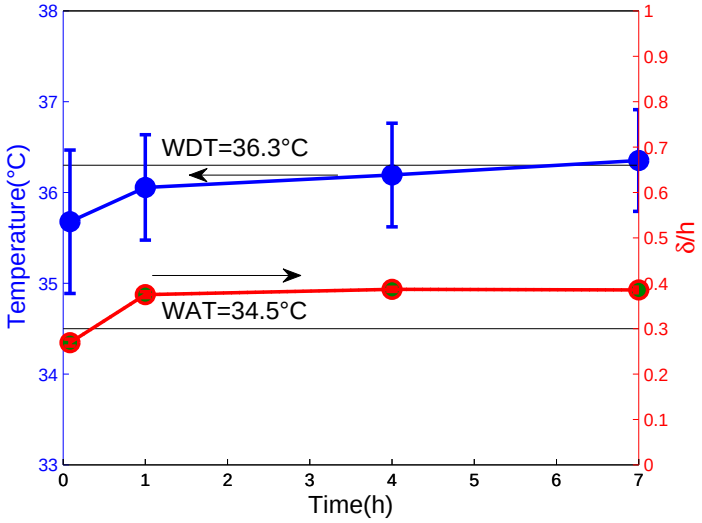


Figure 7.2: Time evolution of deposit-liquid interface temperature and deposit thickness for Re = 532.

An observation of the data displayed in Figure 7.2 indicates that the temperature of the deposit-liquid interface is around $1^oC$ above the WAT, after 5 minutes of deposition, asymptotically reaching the value of the WDT, as time progresses. The simultaneous presentation of the deposit thickness and interface temperature data in the figure allows one to verify the interface temperature evolution at different stages of the deposition process. The interface temperature is seen to increase as the deposit thickness increases, reaching the WDT at approximately the same time as when the deposit reaches its steady state thickness.

Figure 7.3 presents the data of Figure 7.2 for the first hour of deposition process using an enlarged scale for the time axis in the abscissa. In the figure the first measured data point at 5 minutes can be better visualized. An observation of this figure indicates that it would have been desirable to have information for intermediate times between 5 min and 1 hour in order to better describe the warming trend of the interface. However, the experiments reported were time consuming and it was not feasible to obtain these additional data within the time frame of the present work.

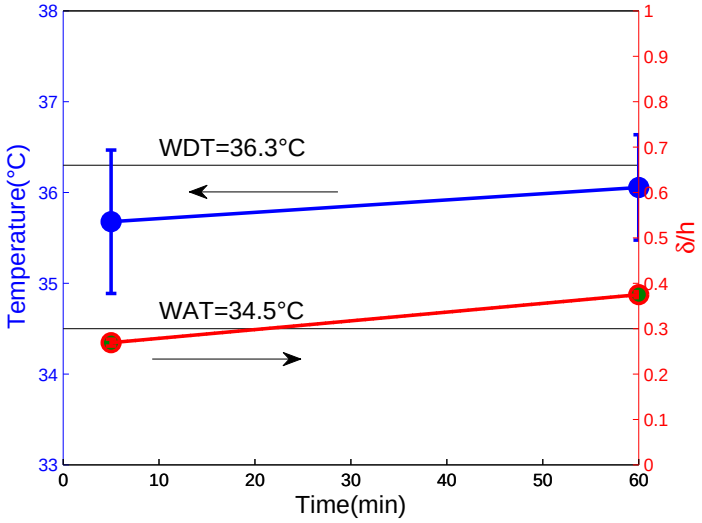


Figure 7.3: Time evolution of deposit-liquid interface temperature and deposit thickness for Re = 532. Results for the first hour of deposition.

Figures 7.4 to 7.7 present similar results for the interface temperature and deposit thickness, for the other two values of the Reynolds number investigated. An analysis of these figures reveals the same behaviour as that reported for the case of the lower Reynolds number, i.e, the interface temperature warmer than the WAT at 5 min and asymptotically reaching the WDT as the deposit reached its steady state thickness value.



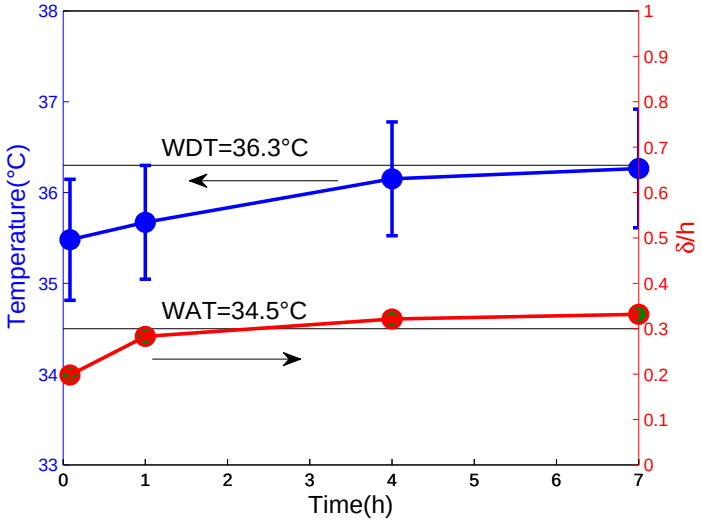


Figure 7.4: Time evolution of deposit-liquid interface temperature and deposit thickness for Re = 876.

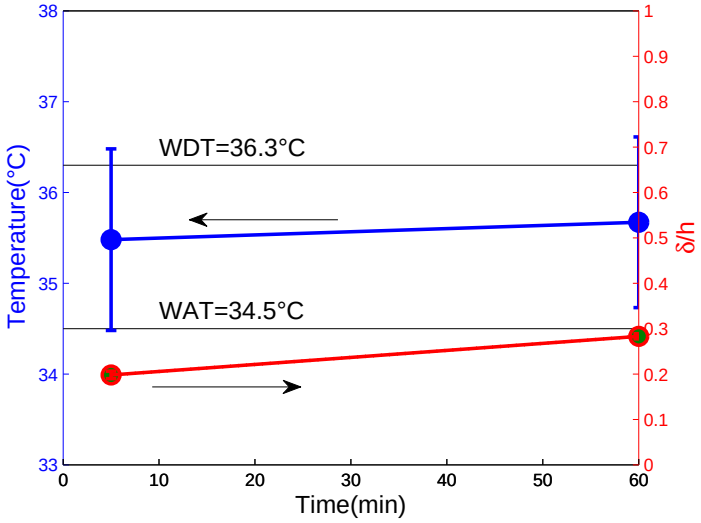


Figure 7.5: Time evolution of deposit-liquid interface temperature and deposit thickness for Re = 876. Results for the first hour of deposition.

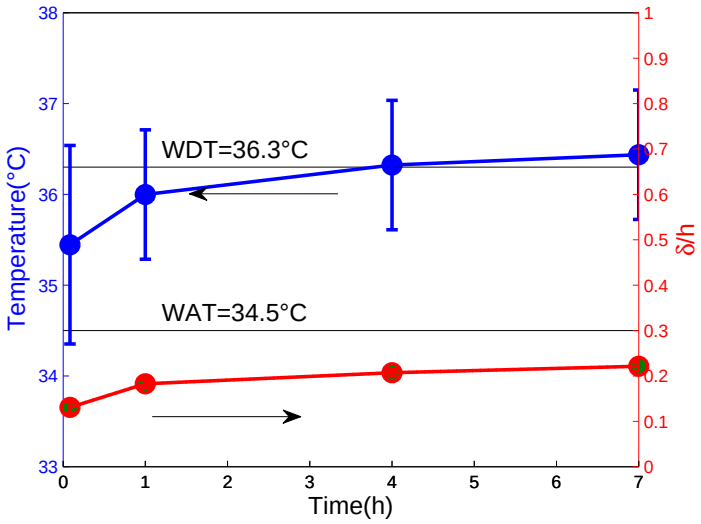


Figure 7.6: Time evolution of deposit-liquid interface temperature and deposit thickness for Re = 1737.

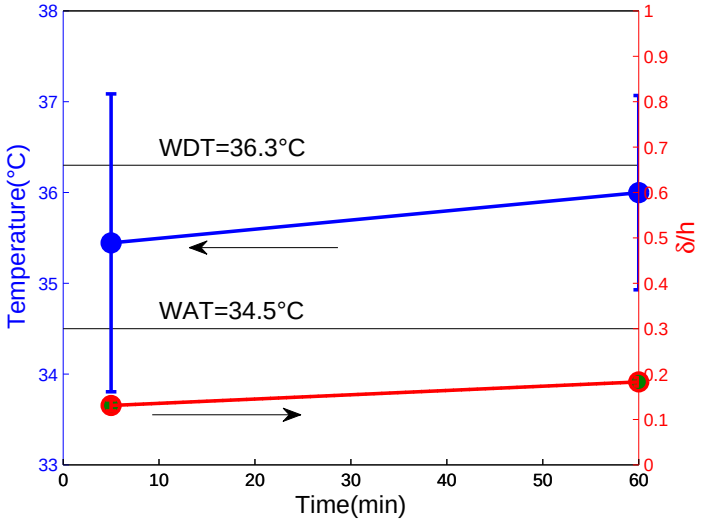


Figure 7.7: Time evolution of deposit-liquid interface temperature and deposit thickness for Re = 1737. Results for the first hour of deposition.

The measurements performed in the present study can be rationalized by the proposition of the following scenario for the deposition process:

**1.** As the wall is cooled, the necessary degree of sub cooling for initiation of the crystallization process is attained and the first layer of crystals, attached to the wall, is formed. This process occurs at temperatures less or equal to the WAT measured for the solution by microscopy.

**2.** Once crystals are already present at the wall, they act as nucleation sites for further crystallization, and the necessary degree of sub cooling to form new crystals is no longer as large as that for the first crystals, so the deposition front progresses at temperatures above de WAT, as evidenced by the measured increase of the interface temperature during the growth phase of the deposit thickness.

**3.** The temperature growth of the deposit interface continues up to the limit of the WDT, the maximum temperature that a solid phase can exist, since this is considered a good representation for the thermodynamic liquidus temperature (Bhat and Mehrotra (2004)).

This scenario corroborates the valid criticism found in the paper by Bidmus and Mehrotra (2008b) regarding the diffusion-based deposition models that assume the interface temperature should always be at a temperature below the WAT for the deposit to grow. Our experiments indicate that the correct condition for the limitation of the interface growth for the diffusion-based

models should be the attainment of the WDT and not the WAT. Also, the results of the present experiment are not in agreement with the experiments of Bidmus and Mehrotra (2008a) conducted for a cylindrical tank for static and sheared conditions. In their work, the interface temperature evolved at the WAT for either static or sheared conditions. The cooling rate applied in their experiments, of the order of $2°C/min$, was half the one used in the present work. In the present experiments, the deposition process was shown to evolve, with an interface temperature that varied from a value close to the WAT to the WDT, when a steady state deposition thickness was attained. The cooling rate effect was not evaluated in the present work.

It might be interesting to verify the effect of the shear rate, or the Reynolds number, on the interface temperature as the deposit thickness evolves. To this end, Figure 7.8 was prepared where the temperature evolution of the deposit–liquid interface is presented for the three values of the Reynolds numbers tested. These are the same data presented in the previous figures.



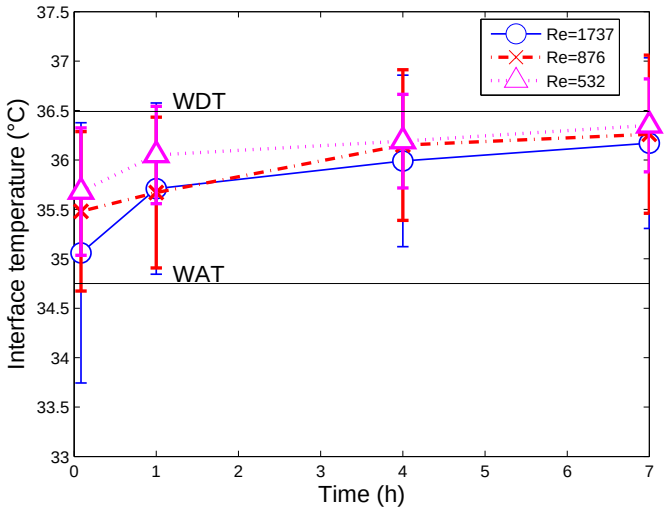


Figure 7.8: Measured time evolution of the deposit-liquid interface temperature for different values of the Reynolds number.

As can be verified in Figure 7.8, the interface temperatures measured for 5 min, 1, 4 and 7 hours are virtually the same for the three values of the Reynolds numbers tested and indicated in the figure. Therefore, one is led to the conclusion that there is no influence of the shear rate on the evolution of the interface temperature, for the range of Reynolds numbers tested and for the cooling rate employed.

## 7.4
## Results for the deposit–liquid interface temperature: annular test section experiments

The time evolution of the deposit–liquid interface temperature was also measured for the annular test section. As described in Chapter 3, the Plexiglass outer pipe, forming the annular test section, was equipped with a port, located at a distance from the flow entrance plane equal to 0.80 of the pipe length. This port was especially designed to allow for the coupling with the thermocouple probe, described in Chapters 3 and 6. As already mentioned, due to the need to firmly fix the probe holder on the curved outer wall of the Plexiglas tube, the piece that connected the temperature probe and the micrometer screw on the wall covered the view from the thermocouple tip. This shortcoming in the probe design prompted the development of a special experimental procedure for measuring the deposit-liquid interface temperature for the annular test section. Meanwhile, a new design for the probe support was being prepared to allow for visual access to the probe tip inside the annular channel. Unfortunately, the new probe design had not been constructed by the time the present research was being conducted. Following is a description of the experimental procedure developed to measure the deposit-liquid interface temperature without visual access to the probe tip.

As explained in the previous chapter, the digital camera that recorded the time evolution of the deposit thickness, inside the annular channel, was positioned so as to image a region adjacent to the probe holder, as seen in Figure7.9. Previous deposition experiments have demonstrated that at this axial position, far from the entrance plane, the deposit interface was already perfectly horizontal. That fact guaranteed that the deposit thickness, measured by the digital camera, was the same as that a few millimetres downstream, where the thermocouple probe was located and not visible by the camera.

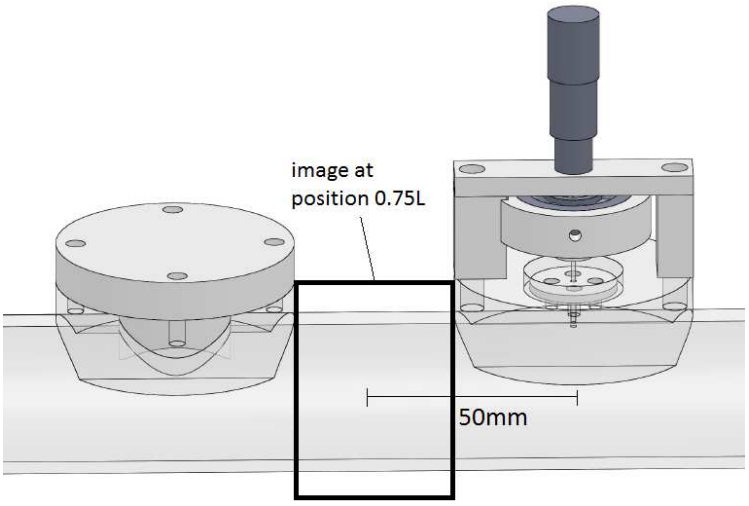


Figure 7.9: Camera field of view adjacent to the thermocouple probe for measuring the deposit-liquid interface temperature in the annular test section.

The experiment started with the solution being pumped through the annular section, at a pre-set Reynolds number value and at a temperature equal to the inner copper tube temperature. After the thermal steady state condition was attained, cooling of the copper wall was initiated, by pumping cold water through the inner copper tube. The digital camera was started, initiating the recording of the deposit thickness time evolution. At a pre-defined time after the initiation of the cooling, the probe was manually traversed through the annular space, recording the temperature profile in the liquid phase and also within the already formed deposit, until the copper surface was reached. The exact position of the copper wall was known from previously conducted calibration experiments, so the exact setting on the micrometer drum, driving the probe, could be adjusted.

The deposit thickness and the temperature profile data results could be matched to obtain the interface temperature. As an example, the deposit–liquid interface temperature at 5 minutes was obtained by verifying the measured distance from the wall, to the deposit–liquid interface, at 5 minutes after the initiation of the copper wall cooling. Then, the temperature value corresponding to this distance was obtained from the measured temperature profile. This temperature was the interface temperature value assigned to the interface at 5 min.

Figure 7.10 summarizes the procedure employed for determining the interface temperature in the annular section for the three values of the Reynolds number tested, 743, 1440 and 2073, and for the four time intervals after the initiation of the wall cooling, 5 minutes, 1, 4 and 7 hours. In each

plot, the solid horizontal line represents the position of the deposit-liquid interface, measured by the digital camera at the particular time and Reynolds number indicated. The position is given in the ordinate, in dimensionless form relative to annular gap space, i.e., zero represents the cooper tube surface, and 1 the plexiglass wall. The symbols in the figures are the temperature measurements taken by the temperature probe across the annular gap. The intercept between the horizontal line with the temperature profile indicates the interface temperature.

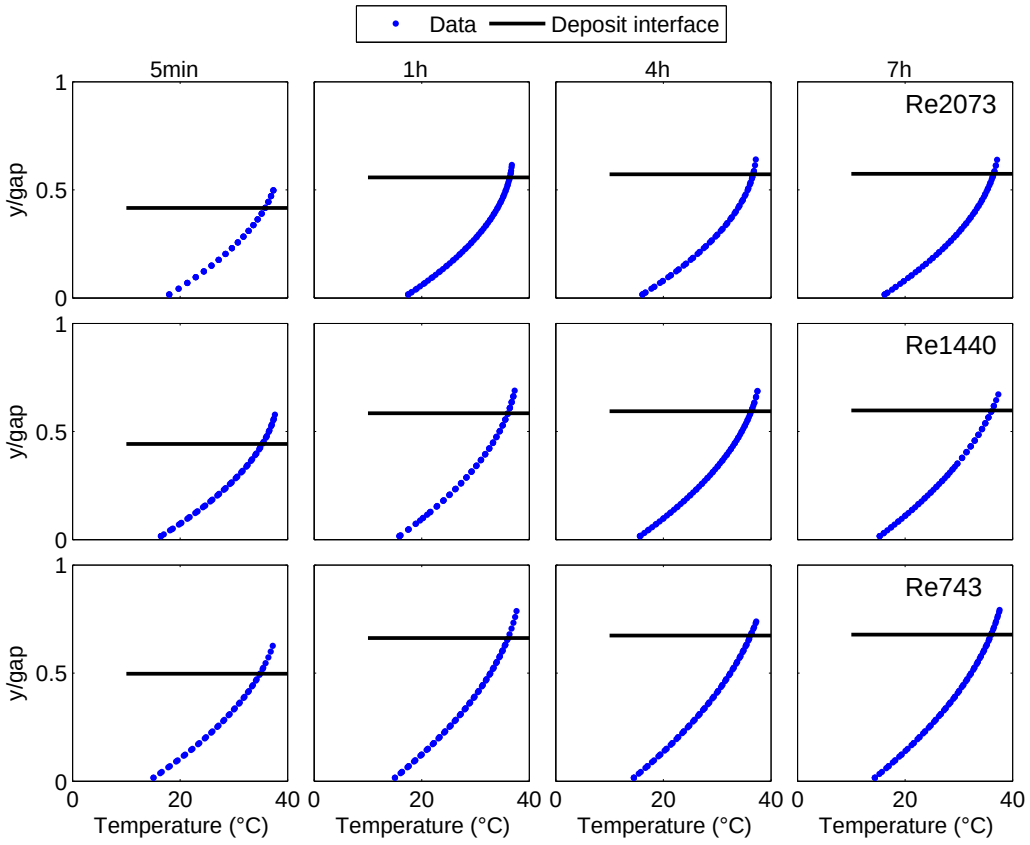


Figure 7.10: Measured temperature profiles and deposit thicknesses for different times and values of the Reynolds number indicated in the figure. Intercept of the deposit thickness and temperature profile data determines the deposit-liquid interface temperature.

Table 7.3 presents the results for the measured deposit–liquid interface temperatures. In the table, the last column indicates an estimate for the measurement uncertainties. The uncertainty level was estimated by combining the calibration uncertainty of the thermocouples, with the standard deviation of the measured temperature fluctuations and the uncertainty associated with the probe size. Even though the probe could be considered small, with a size of approximately 0.2 mm, the uncertainty associated with the probe size was the dominant one. This component of the uncertainty was evaluated by

employing the measured temperature gradient, at the interface location. As mentioned before, corrections due to heat transfer through the probe wires to the measuring tip, were found to be negligible for the lowest Reynolds number cases (see the Appendix B). However a correction of the order of $0.3°C$ was included in the higher Reynolds number case according to the work by Hennecke and Sparrow (1970). It is worth mentioning that each data point presented represents the averaged value from the replication of three experiments.

Table 7.3: Time evolution of the deposit-liquid interface temperature for different Reynolds numbers for the annular test section.

| | **Interface Temperature** | | |
|---|---|---|---|
| | Time instant | Temperature ($°C$) | Uncertainty ($\pm°C$) |
| **Re=743** | | | |
| | 5 min | 35.31 | 0.60 |
| | 1 h | 36.05 | 0.84 |
| | 4 h | 36.21 | 0.68 |
| | 7 h | 36.01 | 0.58 |
| **Re=1440** | | | |
| | 5 min | 35.30 | 0.73 |
| | 1 h | 36.03 | 0.53 |
| | 4 h | 36.34 | 0.60 |
| | 7 h | 36.13 | 0.78 |
| **Re=2073** | | | |
| | 5 min | 35.41 | 0.64 |
| | 1 h | 36.10 | 0.55 |
| | 4 h | 36.44 | 0.97 |
| | 7 h | 36.20 | 0.70 |



The information from Table 7.3 is presented next, in graphical form, employing the same format as that used for the presentation of the results from the rectangular test section, i.e., presentation of the time evolution of the interface temperature together with the time evolution of the deposit thickness.

Figure 7.11 presents the evolution of the interface temperature data and the deposit thickness for Reynolds number equal to 743. Interface temperature and deposit thickness data are presented for 5 min, 1, 4 and 7 hours after the initiation of the cooling of the wall. The simultaneous analysis of the interface

temperature and thickness data of Figure 7.11 leads to similar observations as those made for the rectangular channel test section. Indeed, it is seen that, as the deposit grows toward its steady state thickness, the interface temperature increases, from a value above the WAT at 5 min, to a value close to the WDT. Figure 7.12 shows the same data as the previous figure, using an enlarged time scale for the abscissa, in order to facilitate the observation of the early times, in the deposition process.

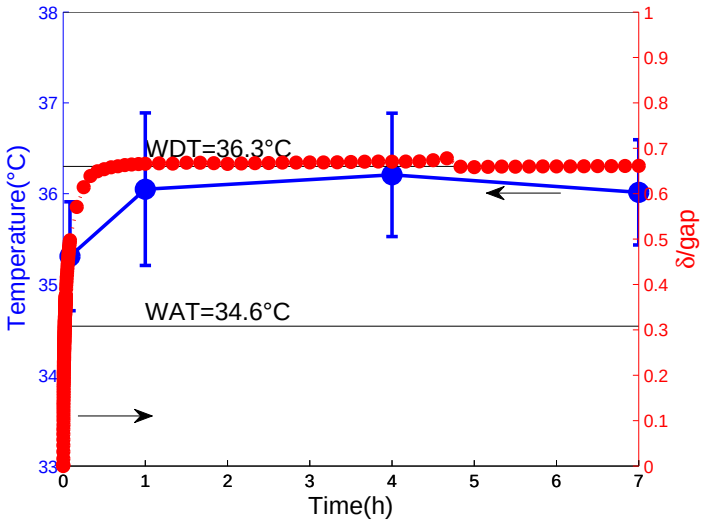


Figure 7.11: Time evolution of deposit-liquid interface temperature and deposit thickness for Re = 743.

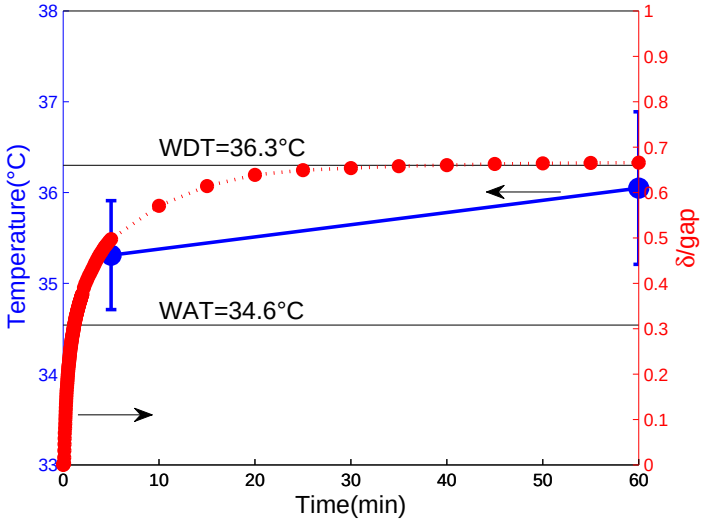


Figure 7.12: Time evolution of deposit-liquid interface temperature and deposit thickness for Re = 743, at the first time instants.

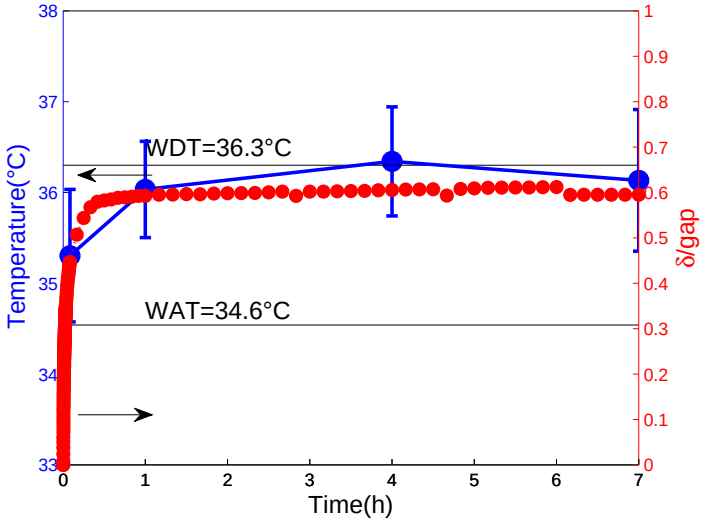


Figure 7.13: Time evolution of deposit-liquid interface temperature and deposit thickness for Re = 1440.

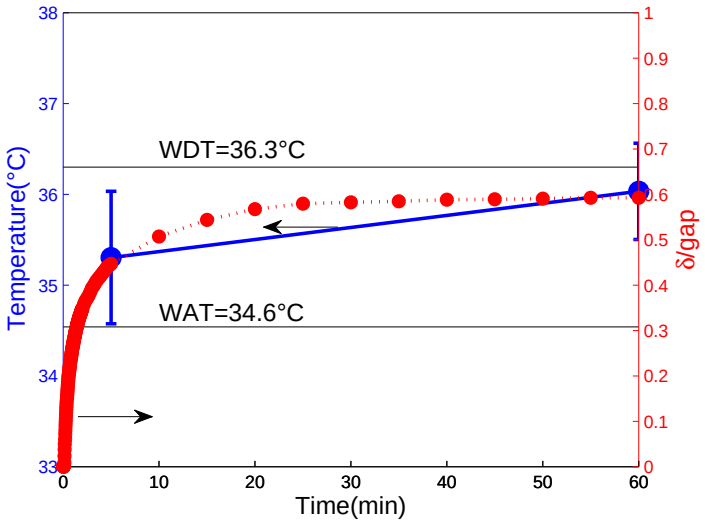


Figure 7.14: Time evolution of deposit-liquid interface temperature and deposit thickness for Re = 1440, at the first time instants.

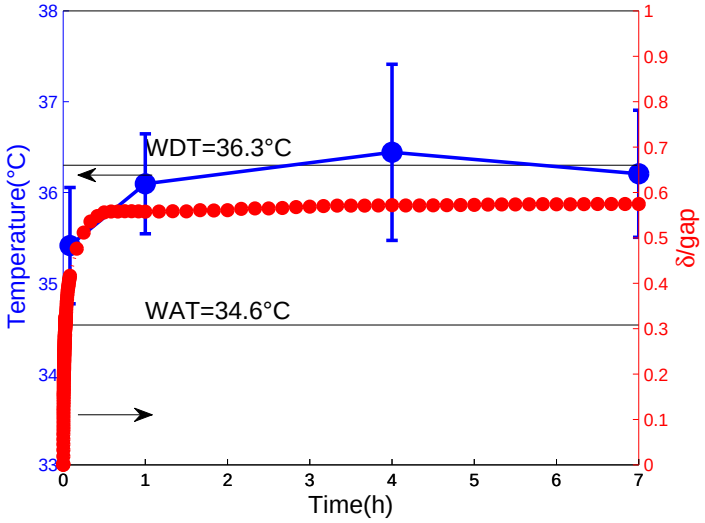


Figure 7.15: Time evolution of deposit-liquid interface temperature and deposit thickness for Re = 2073.

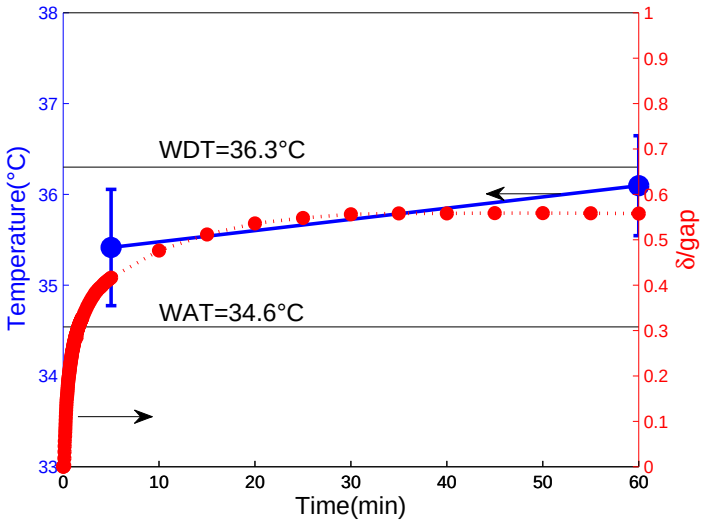


Figure 7.16: Time evolution of deposit-liquid interface temperature and deposit thickness for Re = 2073, at the first time instants.

Figures 7.13 to 7.16 present similar results for the interface temperature and deposit growth, for the other two values of the Reynolds number investigated. Again, the same trends described for the case of the lower Reynolds number investigated, and shown in Figure 7.11, can be observed in these results, for the other two higher values of the Reynolds number.

These results, obtained for the annular test section and those for the rectangular test section, indicate the same behaviour of the interface temperature, warming from a value close to the WAT up to the WDT, when the deposit approaches its steady state configuration. Other cooling rates, cooling

wall temperature levels and shear rates should be investigated in order to yield a more complete picture for the deposit–liquid interface evolution, during the deposit formation.

As it was shown for the rectangular channel experiments, the influence of the shear rate on the deposit interface temperature can be observed with the aid of Figure 7.17. In the figure, the time evolution of the interface temperature data, for the three values of the Reynolds numbers investigated, are plotted for comparison purposes.

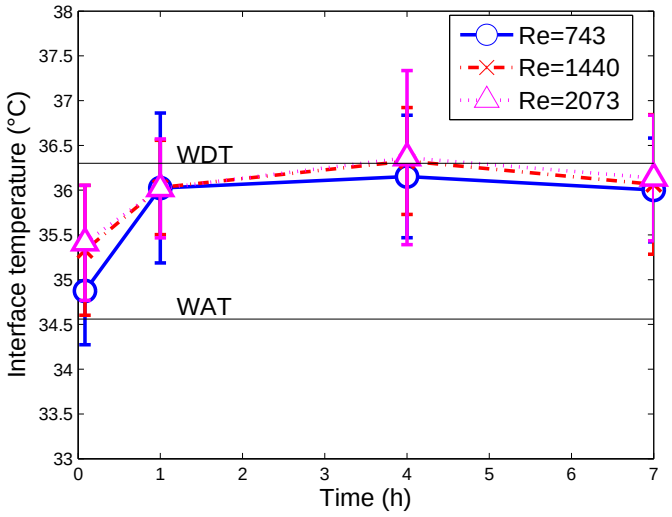


Figure 7.17: Measured time evolution of the deposit-liquid interface temperature for different values of the Reynolds number.

Although the estimated uncertainty levels in the temperature measurements may preclude a definite conclusion, there seems to be an observable trend of the interface temperature increasing with the Reynolds number, at the early stages of the deposit formation. From 1 hour of deposition on, the Reynolds effect on the interface temperature is no longer present, as the interface temperature approaches the thermodynamic liquidus temperature represented by the WDT. Again, other cooling rates should be investigated and, if feasible, employing temperature probes with lower uncertainty levels.

## 7.5 Conclusions

The present chapter presented results for the evolution of the deposit–liquid interface temperature with time, measured by a fine probe, until the interface attains its steady state configuration. Measurements were performed for both, the rectangular and annular test sections. The results indicated that, for the range of the laminar Reynolds numbers tested, the interface

temperature evolved from a value close to the WAT to a temperature close to the WDT, as the deposit thickness grew and attained its steady state configuration. These results seem to be an original piece of information that contradict some hypothesis incorporated in a number of molecular-diffusion-based deposition models. Those models assume the temperature of the interface reaching the WAT, as the deposit reaches its steady state thickness.

Experiments were also conducted to demonstrate that the values for the WAT and WDT measured under flowing conditions are similar to those measured at static conditions, for the range of Reynolds number and cooling rates investigated.

# 8
# Deposit composition

One of the main concerns in wax deposition mitigation is the ability to estimate the strength of wax deposits. The prediction of composition and mechanical characteristics of the deposit is relevant when defining the method for removing wax deposits from production lines.

Rheology measurements have been used to study crystalization kinetics (Ronningsen et al. (1991); Singh and Fogler (1999); Silva and Coutinho (2004); da Silva and Coutinho (2007)). The evolution of rheological parameters has been shown to depend on the degree of crystallinity of the compound. For some compounds, the variation on rheological properties is only noticeable at very high degrees of crystallinity. In the case of paraffin crystallization, variation on rheological properties are observed at low solid saturation, which suggests that few junctions are needed to form a crystal network in that case (da Silva and Coutinho (2007)).

Wax deposits are known to be formed by a matrix of crystals, filled with entrapped oil. They are also known to change its structure with time, becoming richer in high molecular weight molecules and with lower amounts of entrapped oil. As mentioned in Chapter 2, some research groups have tryied to capture the physical phenomena behind that specific behaviour, the so called aging process, (Singh et al. (2001b); da Silva and Coutinho (2007); Bhat and Mehrotra (2008); Hoteit et al. (2008)), however no consensus on the topic has yet been attained. Generally speaking, diffusion, Ostwald Ripening and shear effects have been cited in the literature as possible mechanism that would produce more paraffin and less solvent into the deposit.

Singh et al. (2001b) have proposed that the aging process is directly related to the temperature gradient across the deposit, suggesting that when the temperature gradient goes to zero, the aging process ceases. More specificaly, the work of Singh et al. (2001b) suggests that a particular carbon number indicates the threshold for the counter-diffusion process, as proposed by Singh et al. (2000). Which means that molecules with carbon number higher than a critical value would diffuse towards the gel-like deposit and those under that value would diffuse out. The result of this counter-diffusion process would be

the variation in the carbon distribution of the wax deposit when subjected to a long process of deposition. The authors indicate that the cooling rate may affect the nature of the gel, however the variation in carbon distribution is assumed to exist, independently of the cooling rate.

Experimental information on the variation of the deposit composition may provide a useful database for the development of more accurate wax deposition models. In the present work, experimental data on the composition of the deposit layer was obtained, employing the experimental setup and procedures described in Chapters 3, 5 and 6. The composition results obtained for the rectangular and annular test sections will be presented and discussed below.

## 8.1
## Composition measurements in the rectangular test section

### The sampling

Samples from the wax deposit formed over the bottom plate of the rectangular test section were removed and analysed by High Temperature Gas Chromatography, HTGC. Samples were collected from experiments corresponding to three values of the Reynolds numbers, based in the clean channel dimensions, namely, 532, 876 and 1737. For each Reynolds number, samples were removed for three time intervals, one, four and seven hours, counted after the initiation of the deposition process. Repeatability tests were conducted for Reynolds number equal to 1737. In these experiments, five samples were taken from the one and seven hour tests, while three samples from the four hours test.

The composition tests were conducted in conjunction with the deposit thickness and temperature profiles measurements described in Chapters 5 and 6. The deposit samples were removed after these tests were completed. Three auxiliary runs were conducted, where temperature profile measurements were not performed prior to the sampling. These runs had the objective of verifying whether the penetration of the thermocouple probe in the deposit altered the deposit composition, by allowing the penetration of the liquid solution into the deposit. No composition changes were observed among the deposits collected from the experiments following the temperature profile measurements and those in which these measurements were not performed.

As described in Chapter 3, the top part of the test section consisted of a polypropylene block that could be easily removed for exposing the deposit and allowing the sampling procedure. The sampling procedure, for a particular data

run, was initiated after the experiments for measuring the deposit thickness evolution and deposit temperature profile were completed, as described in Chapters 5 and 6. Before stopping the pump, the liquid inside the rectangular test section was drained by opening a valve at the outlet of the test section. When the test section was drained, the pump was turned off and the top part of the test section was removed to permit access to the deposit. A thin layer of liquid was observed to remain over the deposit. This thin liquid layer was carefully removed and then a sample of the deposit was obtained with the aid of a small spatula. Special attention was directed to the sampling operation, in order to guarantee that a homogeneous sample was obtained, representing the average composition of the deposit, from the plate-deposit interface, to the deposit-air interface. The removed sample was located over the position of the heat flux sensor, installed in the back of the bottom channel wall. Other deposit properties, such as thermal conductivity, were obtained at his position and will be presented in Chapter 9. So it is interesting to have the data on the deposit composition at the same location.

Each sample removed from the test section was homogenized in a heated glass container. When the sample was in liquid form , a volume of 1 ml was removed and placed in a tight glass bottle to be sent for analysis. The rest of the sample was returned to the tank in the test section. This procedure was adopted in order to reduce depletion of the mixture initial composition.

The total depletion caused by the samplings was smaller than the depletion associated with the deposition process itself. A typical depletion caused by the sampling is exhibited in Table 8.1. As can be verified, the depletion from sampling reduced the wax content of the solution from the initial 20% down to 19.7% wax content, a value considered adequate for the experiments.

Table 8.1: Depletion due to sampling.

| **Geometry test section** | **Mass depleted(g)** | **Final wax content(mass%)** |
|---|---|---|
| rectangular | 16.88 | 19.70 |

### Results

The results for the composition of the wax deposits will now be presented. As already mentioned, measurements were obtained for three values of the Reynolds number based on the clean channel configuration, namely, 532, 876 and 1737, and for three different durations of the experiments, 1, 4 and 7 hours.

Before presenting the quantitative results, it is interesting to comment on the visual characteristics of the deposits. Qualitatively, it was verified that the texture of the deposit was not homogeneous across its thickness. The deposit layer close to the deposit-liquid interface appeared as a hard shell, while the layer close to the cold wall was softer, indicating the presence of larger amounts of liquid. For the lower Reynolds number, a liquid thin layer was found over the cold wall. Some authors have reported experimental studies that show a non-homogeneous composition of the deposit, including the presence of liquid close to the cold wall (Singh and Fogler (1999); Singh et al. (2001a)). Singh and Fogler (1999) made rheometry tests with a model mixture of wax in oil varying the cooling rate and the applied shear stress. The results indicated that a thin layer of liquid appeared close to the fixed cold wall in low cooling rates or high steady shear stresses. Similarly to those results, the same research group Singh et al. (2001a) presented results from flow loop experiments, where the deposit layer was divided in two parts and analyzed separately by HTGC. The results indicated that thick deposits - with thickness higher than 0.5 pipe radius - exhibited non-uniform composition, with the layer closer to the deposit-liquid interface being richer in paraffin wax. The authors have suggested that the thickness of the deposit would have a direct influence over the homogeneity in their composition. In the present study, thinner deposits were obtained and the characteristics observed were similar to the observations of Singh and Fogler (1999). The effect of the deposit thickness on the liquid distribution within the deposit deserves further study.

The tests in the rectangular channel were performed employing the solution containing WAX1, with properties described in Chapter 4. It is a 20% solution in mass of paraffin wax in $C_{12}$ solvent. Table 8.2 presents the data on the presence of the solvent $C_{12}$ in the deposit, for the three Reynolds numbers tested and three experiments durations. The last column in the table represents the uncertainty in the chromatography data, based exclusively on the deviations due to the sampling replication. Since the chromatography experimental uncertainty is of the order of 0.5%, the sampling uncertainty dominates, and the equipment contribution can be disregarded. In the case of the rectangular test section, the sampling uncertainty was evaluated from replication experiments, performed only for the 1737 Reynolds number case. In the replication tests, five samples of the deposit aged for one and seven hours were analysed, as well as three samples for four–hour tests. The sampling uncertainty was calculated as twice the mean deviation of those data. The sampling uncertainty was found to be of the order of $\pm 7\%$ within a 95.4% confidence level. It should be reminded that the quantitative data

were obtained for a homogeneous sample, across the deposit thickness, so no quantitative information on composition variation across the deposit will be given. The results of Table 8.2 can be better visualized in the graph of Figure 8.1.

Table 8.2: Time evolution of the solvent $C_{12}$ quantity inside the deposit layer.

| | **Presence of solvent** | | |
|---|---|---|---|
| | Time instant | $C_{12}$ quantity (Mass%) | Uncertainty (%) |
| **Re=532** | | | |
| | 1 h | 78.74 | - |
| | 4 h | 72.23 | - |
| | 7 h | 68.48 | - |
| **Re=876** | | | |
| | 1 h | 75.04 | - |
| | 4 h | 69.11 | - |
| | 7 h | 62.82 | - |
| **Re=1737** | | | |
| | 1 h | 69.90 | 7.7 |
| | 4 h | 58.81 | 6.8 |
| | 7 h | 52.35 | 7.9 |

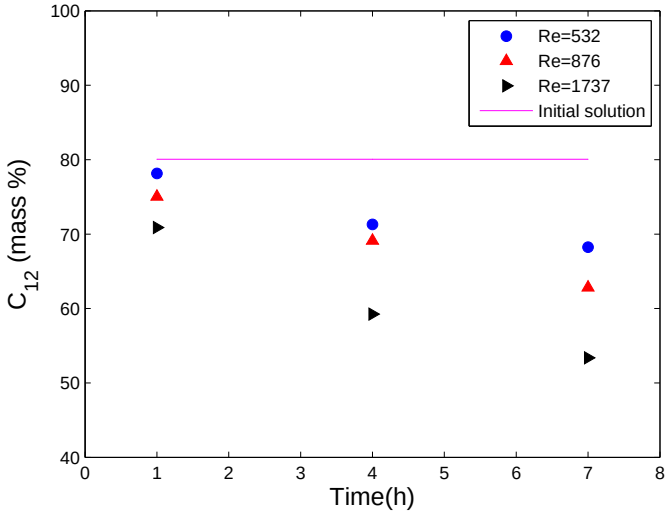


Figure 8.1: Time variation of the mass content of solvent $C_{12}$ in the deposit for different Reynolds numbers. Rectangular test section.

Figure 8.1 presents the temporal variation of the mass concentration of the solvent $C_{12}$ in the deposit, for each value of the Reynolds number investigated. As can be observed, the mass percentage of solvent in the deposit decreases with the duration of the experiment, for all values of the Reynolds number. This behaviour is well documented in the literature representing the aging of the deposit. The decrease observed is more pronounced for the higher Reynolds number values tested. Indeed, percentage variations of the solvent mass concentration equal to 27, 17 and 12% were measured respectively for Reynolds numbers of 1737, 876 and 532. This tendency of lower solvent content for higher Reynolds numbers can, conceivably, be attributed to the increased mass transfer coefficients, associated with the higher Reynolds values, which enhance the mass transfer process of the higher carbon number species, from the flowing solution, into the deposit. For the same experiment duration, one can observe in Figure 8.1 that the variation of $C_{12}$ mass content in the deposit with Reynolds is of the same order of that observed for the time variation and a fixed Reynolds, namely,9, 21 and 27% respectively for 1, 4 and 7 hours at the highest Reynolds number.

The temporal evolution of the wax distribution measured in the samples collected along the rectangular channel experiments are presented in Figures 8.2, 8.3 and 8.4, respectively, for Reynolds numbers equal to 532, 876, and 1737. In each of these figures the species carbon number distributions are plotted for 1, 4 and 7 hours of experiments. The initial carbon distribution of the solution is also plotted to serve as a reference. A general observation of Figures 8.2, 8.3 and 8.4 indicates that the distribution of the species carbon numbers is shifted toward higher values for longer experiments. This effect is more pronounced for the higher values of the Reynolds numbers investigated, as can be verified by a comparison of the results from Figures 8.4 and 8.2, corresponding, respectively, to Reynolds numbers of 1737 and 532. As already commented, this process is referred to as the deposit aging in the literature.

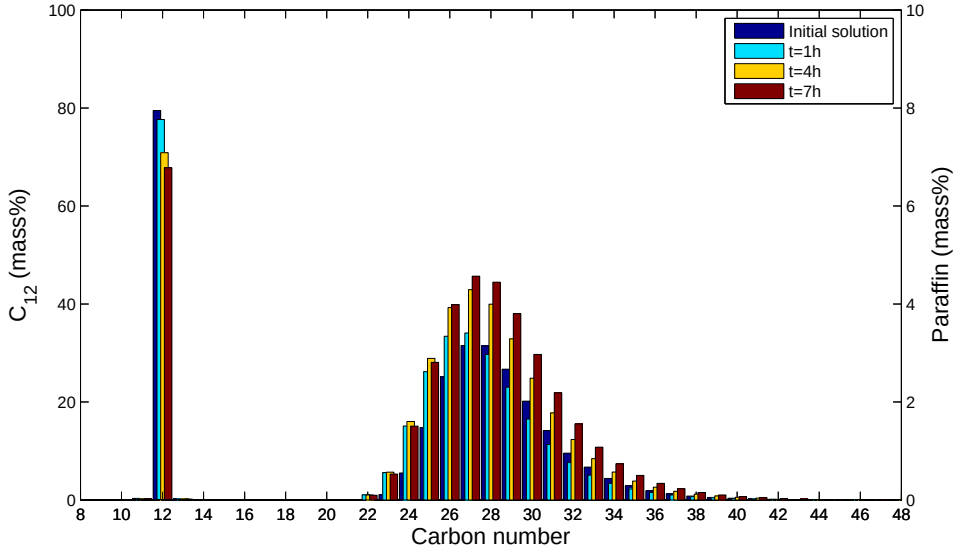


Figure 8.2: Composition varying with time for Re=532.

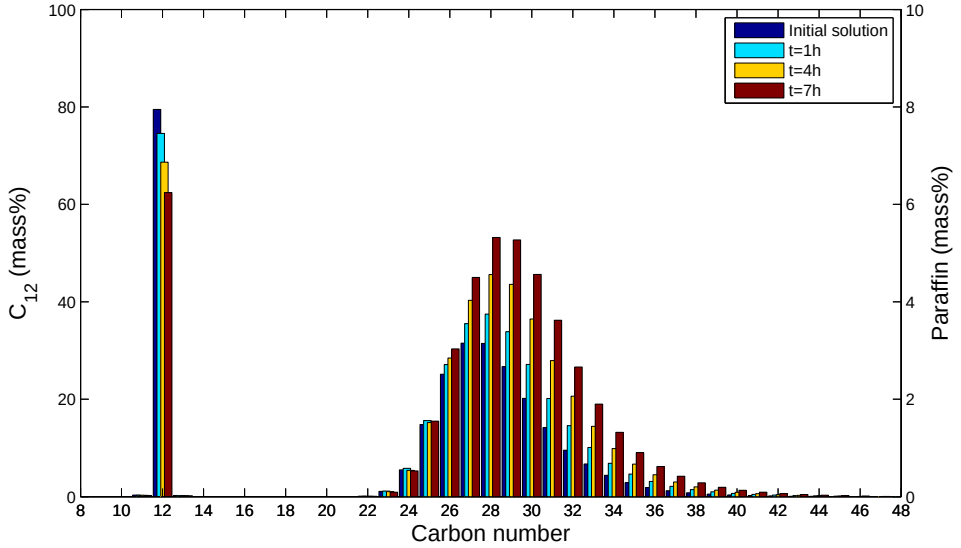


Figure 8.3: Composition varying with time for Re=876.

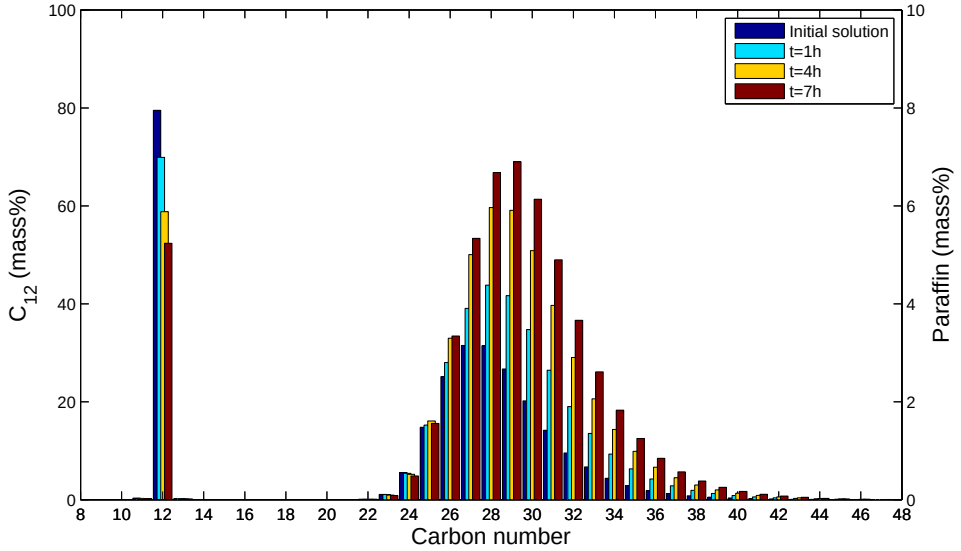


Figure 8.4: Composition varying with time for Re=1737.

An enlarged view of the data displayed in Figures 8.2 to 8.4 is presented in Figures 8.5 to 8.7. In these figures the time variation of each species concentration can be clearly seen. For the higher Reynolds values, 876 and 1737, Figures 8.6 and 8.7, a critical carbon number was identified. As proposed by Singh et al. (2001b), the critical carbon number is the carbon number of the species, above which all species mass concentrations increase with time within the deposit. In Figure 8.6, a comparison of the initial solution distribution to the distribution corresponding to 7 hours of experiment indicates no decrease in mass concentration for $C_{24}$. Above that value all species experience an increase in mass concentration after 7 hours. So, $C_{24}$ should be called the critical carbon number for the deposit. The same value for the critical carbon number is identified for Reynolds number equal to 1737, in Figure 8.7. For the lowest value of the Reynolds number studied and presented in Figure 8.2, a critical carbon number value number could not be identified.

However the critical carbon number results should be analysed with care since the mass fraction of the components with carbon number under 25 is smaller than 1%, leaving any conclusions about the critical carbon numbers too close to the limitations of the experimental technique.

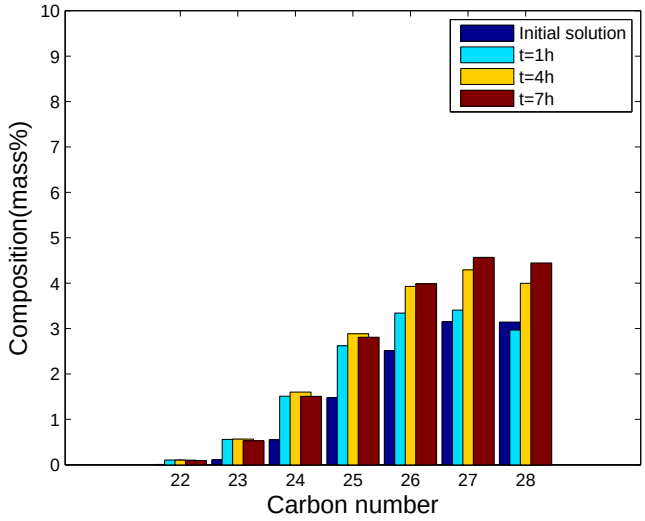


Figure 8.5: Detail of the composition varying with time for Re=532, in the carbon number region between n=22 to n=26.

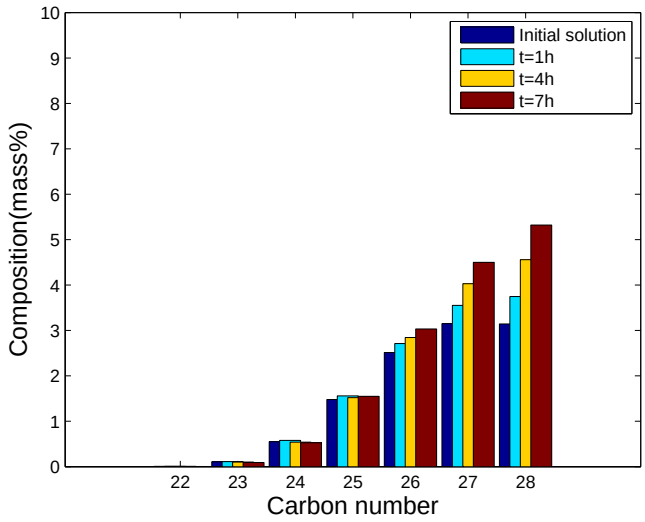


Figure 8.6: Detail of the composition varying with time for Re=876, in the carbon number region between n=22 to n=26.

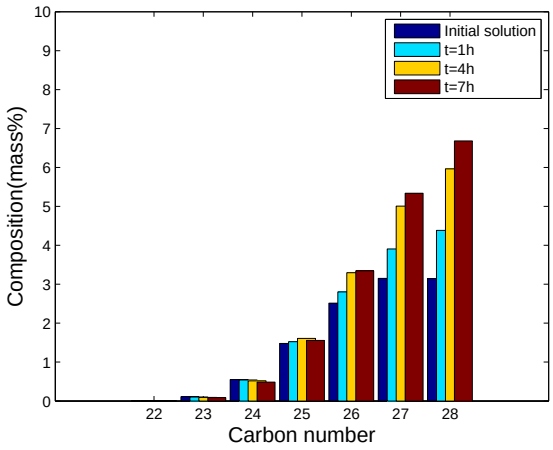


Figure 8.7: Detail of the composition varying with time for Re=1737, in the carbon number region between n=22 to n=26.

An additional view of the carbon distribution of the samples extracted from the deposits can be found in Figures 8.8 and 8.9. In these figures, the species carbon number distributions are presented as lines, what facilitates the analysis of the trends with Reynolds and time. In Figure 8.8, the carbon number distributions for each Reynolds number are plotted for the three durations of the experiments. The initial carbon number distribution of the solution is also plotted as a reference. In Figure 8.8 the wax content increases with time, for every time interval, from the initial to the seven-hour composition. The tendency is observed for all Reynolds numbers. The lower Reynolds number data, however, shows a slight shift to the left, in relation to the other Reynolds number data. That behaviour was associated with experimental uncertainties. The average carbon number distribution of the deposit, varying with the Reynolds number, is exhibited in Figure 8.9. In the figure, it is possible to observe that the wax content increases with the Reynolds number for every pair of Reynolds number analysed. That behaviour is repeated for all time intervals.

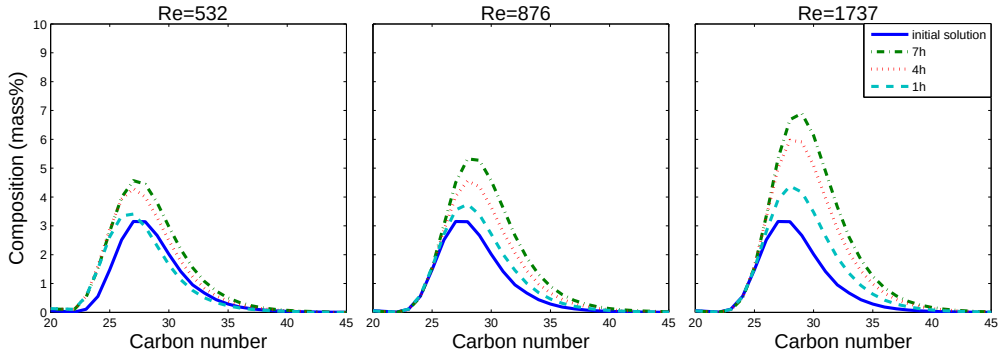


Figure 8.8: Average mass composition of the deposit varying with time for the Reynolds number 532, 876 and 1737.

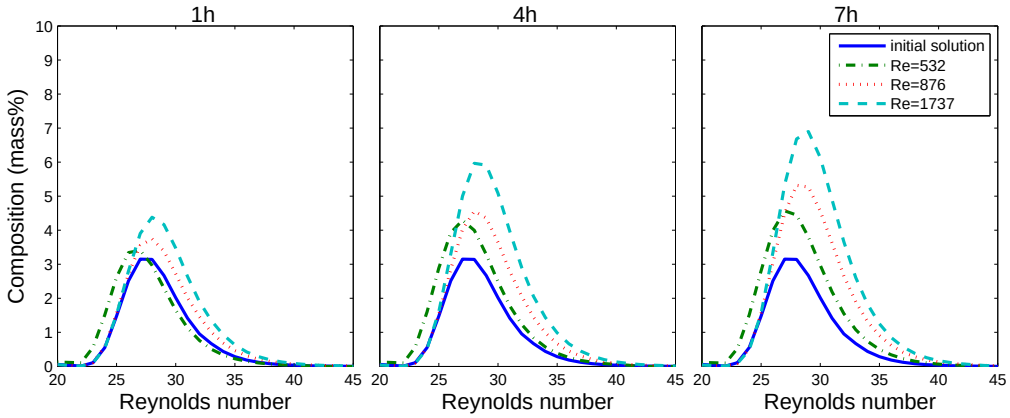


Figure 8.9: Average mass composition of the deposit varying with the Reynolds number for three time instants: one, four and seven hours.

## 8.2 Composition measurements in the annular test section

Attention is now turned to the experiments conducted with the annular test section. As in the case for the rectangular channel just described, the composition measurements were performed by analysing deposit samples removed after the deposit thickness and deposit temperature profile experiments were performed.

### The sampling

Samples from the deposit, formed over the cold internal pipe of the annular test section, were removed and analysed by High Temperature Gas Chromatography, HTGC. Samples were taken for three Reynolds number, 743, 1440 and 2073 and for three time durations of the experiments, one, four and seven hours. The repeatability of the measurements was inferred from the results of three replications tests, of every configuration. A total of 27 deposit samples were analysed.

Figure 8.10 illustrates the outer plexiglass pipe of the annular test section. As described in Chapter 3, this pipe had a port designed for allowing the sampling of the deposit, placed at 730 mm from the inlet of the test section, which corresponds to 0.70 of the copper tube length. When opened, the port allowed access to the internal part of the test section. The port could be closed with the aid of a cap.

After a deposition test, described in Chapter 5, had been conducted up to the desired time duration, the test section was drained. In order to minimize the draining time, the pump, responsible for maintaining the flow of solution through the test section, was maintained on. An appropriate valve operation

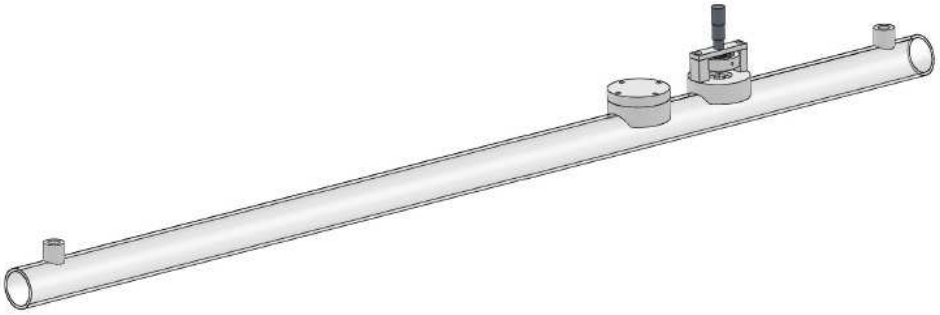

Figure 8.10: Window for sampling in the annular test section.

allowed the pump to rapidly suck the solution from the test section. Typically, the test section was drained in 20 seconds. After that, the pump was switched off and the water contained in the external box, surrounding the test section, was also drained, until the sampling port was exposed to the ambient. The cap of the port was then removed, giving access to the interior of the annular test section.

The sampling procedure was the same as that already described for the rectangular test section experiments. It involved the removal of a homogeneous sample of the deposit with the aid of a small spatula, the heating of the sample until it attained a liquid state and the removal of a 1-ml sample for analysis. The remaining of the sample was returned to the solution reservoir in order to minimize the depletion of the solution. The total depletion caused by the samples removed was less significant than the depletion caused by the deposition process. Table 8.3 shows the depleted mass, due to sampling, in the test with the annular section, and the final mass concentration of the solution. It can be seen that, also in the case of the annular test section experiments, the final wax concentration is 19.91%, a value indicating a negligible depletion from the initial solution with 20% paraffin wax in mass.



Table 8.3: Depeltion due to sampling.

| **Geometry test section** | **Mass depleted(g)** | **Final wax content(mass%)** |
|---|---|---|
| annular | 20.71 | 19.91 |

### Results

The presentation of the deposit composition results for the annular test section will follow the same format as that used for presenting the deposition experiments in the rectangular test section. The results will be presented for

Reynolds numbers equal to 743, 1440 and 2073, and for experiments durations of 1, 4 and 7 hours.

Qualitatively, observations of the deposit characteristics were made and presented similar results as those observed for the rectangular channel experiments. Indeed, it was noticed that the texture of the deposit was not homogeneous in the thickness and that a hard layer was present close to the deposit–liquid interface. Also the layer of deposit closer to the cold wall was softer, indicating the presence of a high liquid content.

Table 8.4 presents the data on the percentage mass concentration of solvent $C_{12}$, in the deposit, for the different Reynolds numbers and experiment durations investigated. The last column indicates the uncertainty expected for the measurements, based solely on the sampling replications, as already explained for the rectangular test section case.

Table 8.4: Time evolution of the solvent $C_{12}$ quantity inside the deposit layer.

| | **Presence of solvent** | | |
|---|---|---|---|
| | Time instant | $C_{12}$ quantity (Mass%) | Uncertainty (%) |
| **Re=743** | | | |
| | 1 h | 56.06 | 30.3 |
| | 4 h | 59.24 | 2.9 |
| | 7 h | 50.01 | 11.5 |
| **Re=1440** | | | |
| | 1 h | 71.13 | 0.9 |
| | 4 h | 54.84 | 4.4 |
| | 7 h | 47.28 | 6.8 |
| **Re=2073** | | | |
| | 1 h | 69.11 | 1.7 |
| | 4 h | 49.99 | 15.6 |
| | 7 h | 46.20 | 11.9 |

The results of Table 8.4 are presented in graph format in Figure 8.11. In the figure, the solvent content is presented as a function of the duration of the experiments, for each Reynolds number tested.

An analysis of the results in Figure 8.11 shows a similar trend for the solvent content as that observed for the rectangular channel experiments. The mass percentage of solvent in the deposit is seen to decrease with the duration of the experiments, for the three Reynolds numbers investigated, characterizing

the deposit aging process. However, for the annular test section the drop in $C_{12}$ concentration with time is more pronounced than that observed in the rectangular channel. Also, there is an asymptotic trend with time, observed in the values of the $C_{12}$ concentration, for the three values of the Reynolds number tested. This trend was not observed in the rectangular channel experiments and may be attributed to the longer length of the annular channel, as compared to the rectangular test section. Also, in the annular configuration, the dependence of the solvent concentration on the Reynolds number is less pronounced,for all time durations of the experiments.

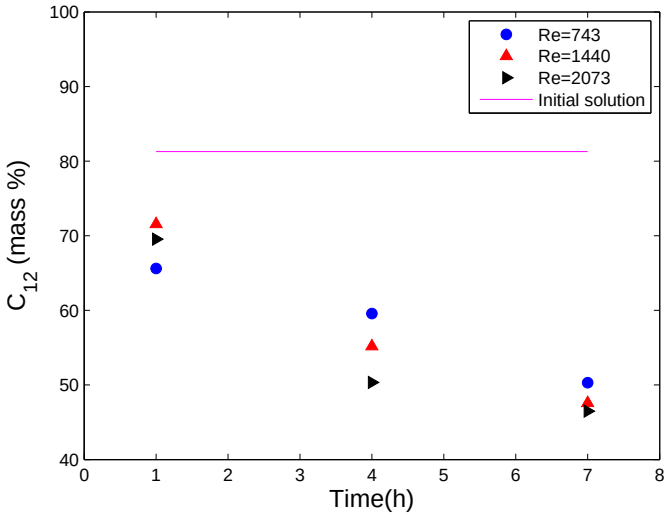


Figure 8.11: Time variation of the mass content of solvent $C_{12}$ in the deposit for different Reynolds numbers. Annular test section.

The temporal evolution of the wax distribution, measured in the samples obtained from the annular test section, are presented in Figures 8.12 ,8.13, and 8.14, respectively for Reynolds numbers equal to 743, 1440, and 2073. In each figure, the species concentration distributions are presented for experiments durations of 1, 4 and 7 hours. The solution initial wax distribution is also plotted for reference purposes. The observation of these three figures reveals the aging process, whereby the deposit tend to get richer in the heavier species. The results for the lower Reynolds number, however, show an unexpected behaviour. It is observed in Figure 8.12 a non-monotonic behaviour in the species composition, with regard to the time duration of the experiments. For any particular species carbon number, the concentration measured at 4 hours is smaller than that measured at 1 hour. A plausible explanation for this behaviour was not found, and one can only attribute it to problems in the experiments of unexpected high levels of experimental uncertainties. The expected monotonic behaviour of the species concentration with time is indeed

observed for the other two values of the Reynolds number investigated, as can be verified in Figures 8.13, and 8.14.

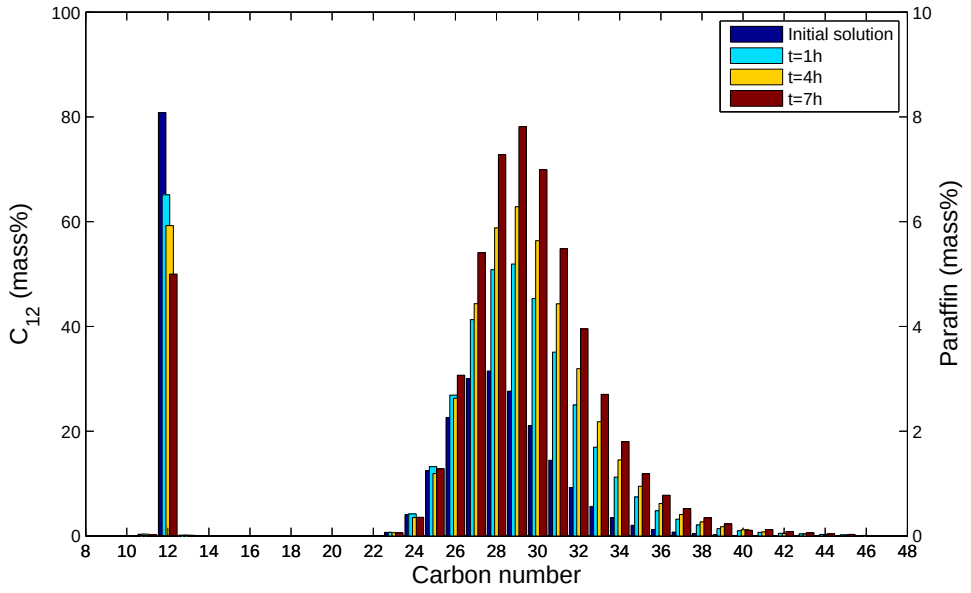


Figure 8.12: Average mass composition of the deposit varying with time for the 736 Reynolds number.

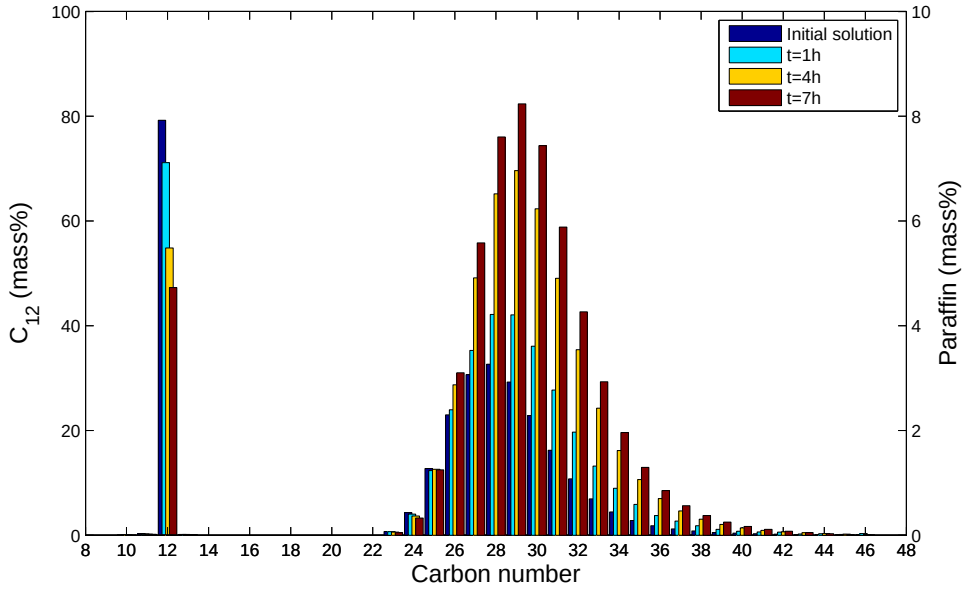


Figure 8.13: Average mass composition of the deposit varying with time for the 1440 Reynolds number.

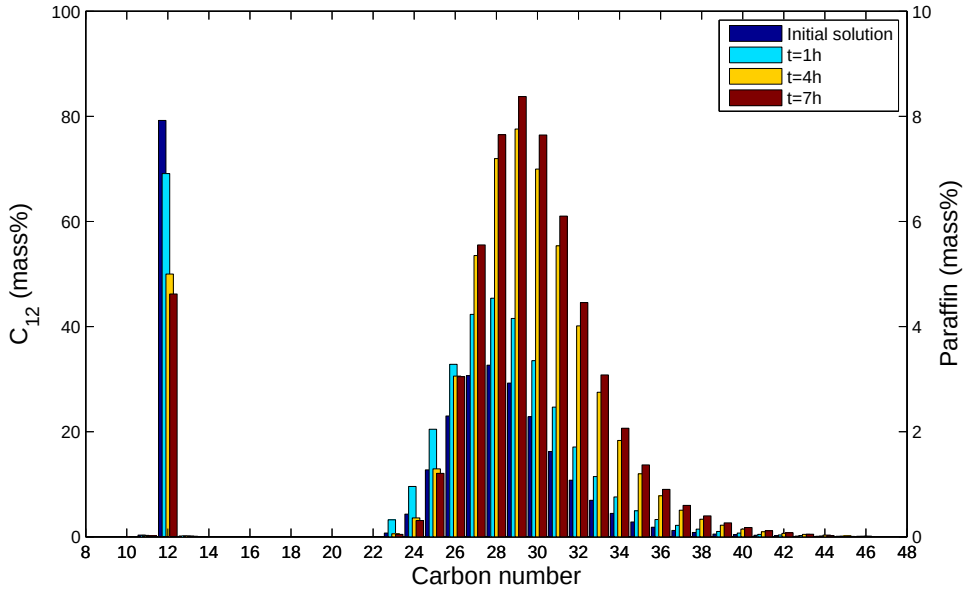


Figure 8.14: Average mass composition of the deposit varying with time for the 2073 Reynolds number.



An enlarged view of the previous results is presented in Figures 8.15 to 8.17. These figures allow one to identify the critical carbon number for each test configuration. As in the rectangular channel experiments, the $C_{24}$ appears as the critical carbon number, above which all components experience an increase in its concentration, in the deposit, with time. Again, the critical carbon number results should be analysed considering that the mass fraction, of the components with carbon number under 25, is smaller than 1%, leaving any conclusions about the critical carbon numbers, too close to the limitations of the experimental technique.

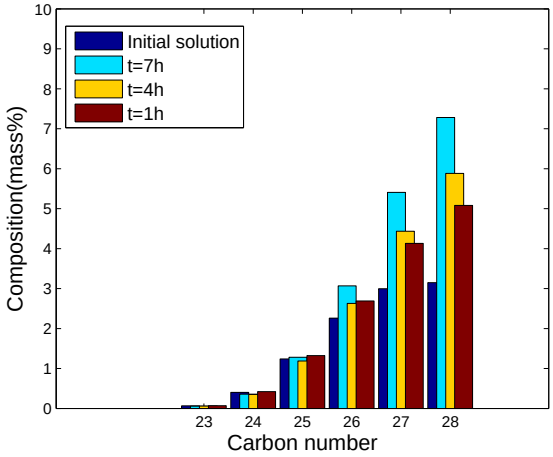


Figure 8.15: Average mass composition of the deposit varying with time for the 736 Reynolds number.

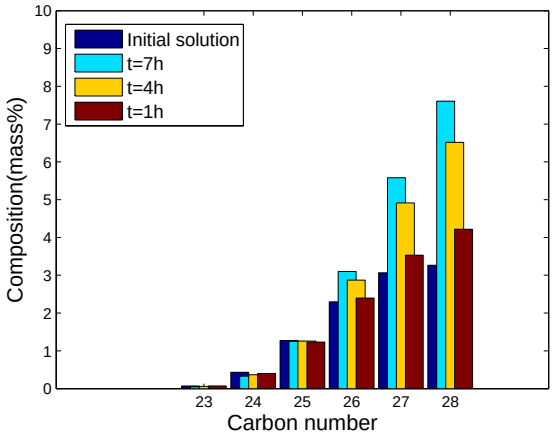


Figure 8.16: Average mass composition of the deposit varying with time for the 1440 Reynolds number.

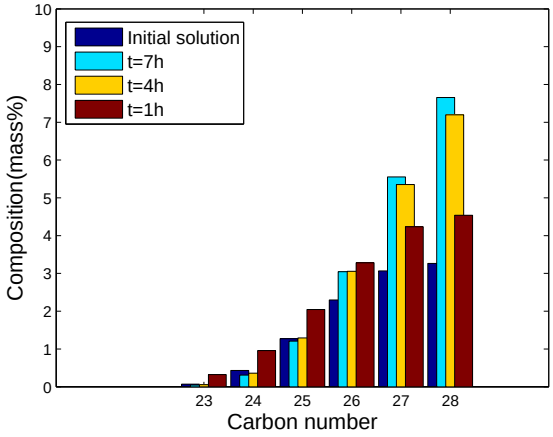


Figure 8.17: Average mass composition of the deposit varying with time for the 2073 Reynolds number.



Figures 8.18 and 8.19 display an additional view of the carbon distribution of the samples, extracted from the deposits. In these figures, continuous distributions of the species carbon number are presented, to facilitate the analysis of the changes observed in the data, with time and Reynolds number. In the figures, the initial carbon distribution is plotted for comparison purposes. In Figure 8.18, the carbon distributions for each time duration are presented together, for each Reynolds number. The observation of the results, for the three Reynolds numbers, show the shift of the peak of the initial carbon distribution, with time, toward the higher carbon numbers, characterizing the aging of the deposit. In Figure 8.19, the same data are plotted as a function of the experiment duration, for the three Reynolds numbers. The interesting information from this figure is the observation that for the long experiment duration, virtually the same carbon distribution is obtained, irrespective of the Reyn-

olds number value, indicating that the influence of the Reynolds number on the carbon distribution is only relevant during the transient deposition phase.

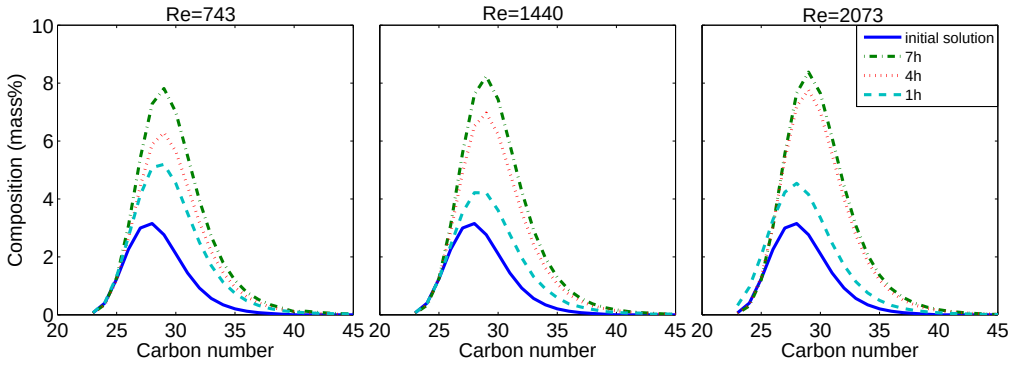


Figure 8.18: Average mass composition of the deposit varying with time for the three Reynolds number: 743, 1440 and 2073.

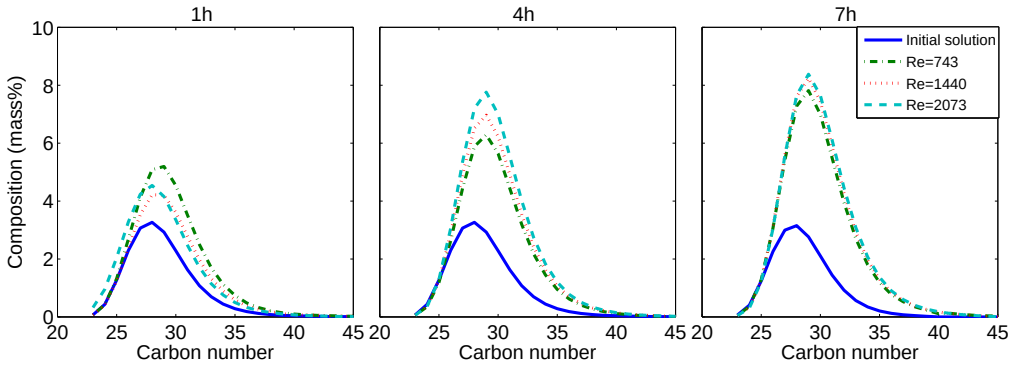


Figure 8.19: Average mass composition of the deposit varying with the Reynolds number for the three time instant: one, four and seven hours.

## 8.3 Conclusions

The present chapter presented a study of the wax deposit composition variation with Reynolds number and the duration of the experiments. Experiments were performed for test solutions made of WAX 1 and WAX2, in the rectangular and the annular channel test sections, respectively. The chromatography analysis of the deposit indicated a similar behaviour between the samples obtained from the two flow configurations. In both test section the mass concentration of the solvent was observed to decrease with time and Reynolds number. The carbon distribution of the paraffins present in the deposits displayed a small shift toward the heavier carbon species, characterizing the so called aging process of the deposit. The critical carbon number was identified to be the same for all Reynolds numbers, in both test sections, indicating that the critical carbon number is linked to the solution properties, and not

to the flow characteristics. However those results should be interpreted with caution since the mass fraction of the components, under the critical carbon number identified, are below 1% of the deposit mass.

However, some distinction between the results from the two test section emerged. The decrease of the solvent fraction in the deposit presented an asymptotic behaviour with time, in the annular test section. The solvent fraction was significantly reduced from one to four hours, a less expressive decrease was observed from four to seven hours. This saturation behaviour was not present in the results from the rectangular test section. This different behaviour can be attributed to differences in the flow characteristics in the two test section and need further investigation, perhaps with the aid of numerical simulations.

# 9
# Deposit thermal conductivity

Heat transfer, from the flowing oil, to the colder environment, seems to be a necessary condition for wax deposition to occur on the internal pipe wall. No matter the level of sophistication of a deposition model, heat transfer across the deposit wax layer plays a significant role in determing the deposit geometric and physical characteristics. Bidmus and Mehrotra (2004) proposed a purely heat transfer model to predict wax deposition and found that the thermal resistance of the deposited layer becomes the dominant resistance when the deposited thickness attains 5% of the pipe diameter, in the case of a typical, non-insulated subsea line.

In order to stress the importance of the knowledge of the deposit thermal conductivity for an accurate wax deposition prediction, a simulation exercise was performed employing the sophisticated compositional deposition model developed by Souza (2014) , based on the work of Banki et al. (2008). This model was briefly described in the Appendix A and it was used in the comparisons with the experimental results obtained, in Chapter 5. In this exercise, the simulation model was run for different values of the deposit thermal conductivity, maintaining all other input information constant. The range of variation of the thermal conductivity input to the model reflects the range encountered in the literature for wax deposit thermal conductivities. The simulation was performed for the annular geometry, described in the previous chapters. The deposit thickness predicted by the model was calculated at a position equal to 0.75 of the annular channel length and for steady state conditions. The results of the simulation exercise are presented in Figure 9.1. As can be seen in the figure, the variation of the deposit thermal conductivity from 0.1 to 0.4 $\frac{W}{m^oC}$, produced a variation of approximately 50% in the estimated deposit thickness.

Tippically, wax deposits are composed by wax crystals on a mixture of liquid wax and solvent. Some authors have suggested that as little as 2% solid is sufficient to form a deposit layer (Holder and Winkler (1965); Singh and Fogler (1999)). Indeed, considering the high content of solvent found in the deposits, some authors proposed the use of the solvents thermal conductivity

in the modelling of deposit properties (Cordoba and Schall (2001); Correra et al. (2007); Guozhong and Gang (2010)). However, as deposits age, the solid content tend to increase and may approach as much as 80% of solid fraction. In those cases, the thermal conductivity could approach the solid thermal conductivity.

Thermal conductivity experimental data is scarce in the literature, even for the solid and liquid phases of n-alkanes. Most works adress n-alkanes with carbon numbers under 20 (Calado et al. (1988); Stryker and Sparrow (1990); H.Watanabe and Seong (2002); Holmen et al. (2002); Konstantinov et al. (2009, 2011); Nabil and Khodadabi (2013); Vélez et al. (2015a,b)). The work of Vélez et al. (2015a,b) presents data of n-alkanes thermal conductivity, in the liquid and solid phases, with good agreement to other studies results. That work suggests that n-alkanes have their thermal conductivity enhanced by a factor between 2 and 3 when passing from the liquid to the solid phase.

Matzain (1999) have reported measurements for the thickness of deposits, during single phase flow, employing the liquid displacement level detection method, which they found to be the most reliable technique. In order to estimate the thermal conductivity of wax deposits, the author compared deposit thickness data from uni-dimensional heat transfer estimations, with the measured deposit thickness. The thermal conductivity was varied until the predicted deposit thickness matched the measured thickness. The thermal conductivity of the deposit was shown to decrease as the entrapped oil fraction increased, being from 1.4 to 2 times the thermal conductivity of the liquid phase. Although the information on the variation trends of the thermal conductivity are useful, this method is associated with high levels of uncertainty, due to its indirect nature, based on a simplified model of the deposition process. Latter, Hoffmann and L.Amundsen (2010) suggested that the knowledge about the thermal conductivity of deposits varying with time would provide a new method to estimate the deposit thickness.

In the work of Bidmus and Mehrotra (2004), the authors propose an one dimensional heat transfer model to investigate wax deposition. The thermal conductivity of the wax deposit was analysed in order to find the best fit between experiments and the numerical model. The thermal conductivity that fitted well the model results was a bit higher than the solid paraffin wax thermal conductivity. However, the authors stated that convective effects could be taking place within the deposit, causing the thermal resistance of the deposit to drop.

As it was demonstrated in this brief introduction, despite its relevance for the proper modelling of wax deposition process, there is no reliable

information on the deposit thermal conductivity, particularly under flowing conditions. The present chapter describes the study conducted with the objective of contributing to providing quantitative information on the deposit thermal conductivity. Also, as will be described, the thermal conductivity measurements will be used as a means of obtaining information on the solid and liquid phase contents of the deposit.

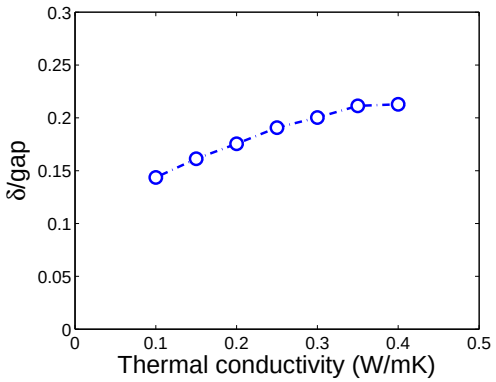


Figure 9.1: Sensibility analysis of thermal conductivity based on the work by Souza (2014).



## 9.1
## Deposit thermal conductivity measurements

The experimental thermal conductivity of the deposit layer, $k_{exp}$, was determined employing the rectangular test section described in Chapter 3. That test section allowed the measurement of the thickness of the deposit, the deposit–liquid interface temperature, the wall temperature and the heat flux through the deposit. Under thermal steady state conditions, these data yield the desired thermal conductivity of deposit, under flowing conditions.

The experimental procedure employed in the thermal conductivity measurements was the same as that described in Chapters 6 and 7, where the rectangular test section was used in the study of the temperature profile in the deposit and its interface temperature. An experimental data run was initiated at a steady state condition with the inlet fluid entering at $38^oC$ and the bottom wall maintained at the same temperature. To initiate a data run, the bottom wall was cooled until it attained $12^oC$. At the cooling rate employed, it took approximately 15 minutes to attain that temperature. A wax deposit wax then gradually formed over the bottom wall of the test section. The heat flux per unit area measured by the heat flux sensor installed in the wall, the wall temperature and the inlet fluid temperature were monitored at a rate of one data per second for about seven hours. The thickness of the deposit and the

interface temperature were measured by the thermocouple probe following the procedure described in Chapters 6 and 7.

A heated air jet was constantly blowing over the external walls of the test section in order to avoid unwanted deposit formation, over the internal Plexiglass wall of the test section, that could disturb the visualization of the interior of the channel. As explained before, the temperature of the lateral Plexiglas wall could drop below the solution crystallization temperature, due to the the thermal contact between the cooled bottom plate and the Plexiglass wall. The use of the heated jets avoided this effects but caused disturbances in the readings of the heat flux sensor. For that reason, at seven hours, the jet was turned off and a comparatively short time period was allowed for a new thermal equilibrium to be attained. The measurements used to determine the thermal conductivity of the deposit were acquired after this new steady state condition, with the heated air jets off. It is important to mention that, although the temperature profile inside de deposit changed by turning the jet off, no growth of the deposit was observed.

It should also be mentioned that, contrary to the deposit thickness measurements of Chapter 5, the visual access to the interior of the channel was not used to directly optically measure the deposit thickness. In the present case, the visual access was used to detect when the tip of the thermocouple probe was touching the deposit–liquid interface. The micrometer reading at this position yielded the deposit thickness.



### 9.1.1
### Data reduction for thermal conductivity determination

For a one dimensional steady state heat transfer condition, considering pure conduction, the heat flux per unit area, crossing the deposit thickness, is given by $q''_y = k\dfrac{dT}{dy}$, where $k$ is the thermal conductivity of the deposit layer, considered constant with temperature, as sketched in Figure 9.2. In pure conduction, a linear temperature profile is expected and the experimental deposit thermal conductivity can be determined by Equation 9-1,

$$k_{exp} = \delta_d \frac{q''}{T_{int} - T_{wall}} = \frac{q''}{dT/dy} \tag{9-1}$$

where $q''$ is the heat flux per unit area, measured by the heat flux sensor.

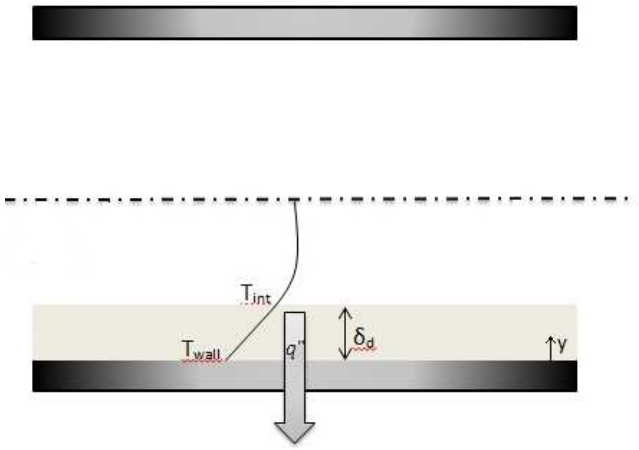


Figure 9.2: Sketch of the one-dimensional heat transfer inside the rectangular test section.

The thickness of the deposit, $\delta_d$ , was measured by the traversing thermocouple device and the results obtained were reported in Chapter 6. $T_{int}$ and $T_{wall}$ are the interface and wall temperatures, and were measured by the traversing thermocouple probe. The temperature derivative in relation to the wall normal coordinate, $dT/dy$, was obtained from the angular coefficient of a linear fit made in the temperature profile data, from Chapter 6. The results of thermal conductivity found employing the discrete values of temperature and thickness and those found employing the angular coefficient of the linear fit were very similar, within 2% of error. The method chosen to calculate the thermal conductivity was the one employing the angular coefficient of the temperature profiles linear fit.



### 9.1.2 Validation tests

Prior to initiating the experiments for measuring the deposit thermal conductivity, preliminary tests were undertaken to validate the measuring procedure. To this end, a Plexiglas plate, with thermal conductivity known from the literature, was used as a reference. The plate, with a thermal conductivity reported in the literature of 0.19 $\frac{W}{mK}$, was machined with the same internal dimensions as those of the rectangular channel and positioned over the bottom plate of the test section. The Plexiglas plate covered the entire surface of the bottom plate, in the exact same way as wax deposit would do, in a data experiment for measuring the deposit thermal conductivity. The thickness of the plate was 5 mm.

The thermal conductivity of the plexiglass was measured under flowing conditions, as in an actual test with wax deposit. The exact same mixture was

pumped through the test section at similar Reynolds numbers, as those used in the wax deposition tests. A temperature gradient was established through the Plexiglas plate, by cooling the bottom plate of the test section and maintaining the incoming test fluid heated. Two levels of hot and cold temperatures were tested, to assess the influence of heat transfer to the external ambient. For the first tests, the bottom plate was maintained at 11 $^oC$ and the flow inlet temperature at 38 $^oC$, resulting in a temperature difference of 27 $^oC$. For the second set of tests, the temperature difference was 11 $^oC$, with the inlet flow at 42 $^oC$ and the cooled plate at 31 $^oC$. All measurements were acquired after the system attained thermal equilibrium. The tests were performed with the heated air jets turned on and off.

Table 9.1 presents the results obtained for the validation tests, made for the Reynolds numbers 876 and 1737. In the last column figures the Plexiglass thermal conductivity from the literature, measured by the Cenco-Fitch ASTM method. As the results demonstrate, the measurement procedure yielded a value for the thermal conductivity of the Plexiglass that differed by only 5% from the value reported in the literature when measured at a Reynolds number equal to 876, with the heated jets turned off. For the highest Reynolds number case, however, 10 and 15% difference were found relative to the literature value. Based on these results, the measuring procedures were considered validated and were employed on the determination of the deposit thermal conductivity, under flowing conditions.

Table 9.1: Thermal conductivity of the plexiglass sheet.

| **Re** | $T_{hot}$ | $T_{cold}$ | $T_{average}$ | **Jet** | $k_{measured}$ $(\frac{W}{mK})$ | $k_{litterature}(\frac{W}{mK})$ **(23**$^oC$**)** |
|---|---|---|---|---|---|---|
| 1737 | 38 | 11 | 24.5 | **ON** | 0.388 | 0.190 |
| 1737 | 38 | 9.1 | 23.6 | **OFF** | 0.215 | 0.190 |
| 1737 | 42 | 31.9 | 37.0 | **ON** | 0.349 | 0.190 |
| 1737 | 42 | 31.2 | 36.6 | **OFF** | 0.206 | 0.190 |
| 876 | 42 | 31.8 | 36.9 | **ON** | 0.344 | 0.190 |
| 876 | 42 | 31.2 | 36.6 | **OFF** | 0.194 | 0.190 |

## 9.2
## Deposit thermal conductivity results

Table 9.2 presents the results obtained for the deposit thermal conductivity measured after a period of 7 hours, for three different values of the

Reynolds numbers indicated in the table. The results indicate that the maximum deviation from the mean thermal conductivity, calculated between the three values of Reynolds number, was of the order of 5%. Considering the average uncertainty level estimated for the measurements of the order of ±12%, it can be concluded that for the range of flow rates investigated, the deposit thermal conductivity is not influenced by the Reynold number. The measured average deposit thermal conductivity was 0.223 $\frac{W}{m^oC}$. The estimated average uncertainty of ± 11.7% was calculated based on the experimental uncertainty of the heat flux, of the temperature profile and the of the measuring probe.

Table 9.2: Thermal conductivity of the deposit.

| **Re** | **K($\frac{W}{mK}$)** | **Uncertainty(%)** |
|---|---|---|
| 532 | 0.225 | 13.5 |
| 876 | 0.228 | 12.7 |
| 1737 | 0.217 | 19.9 |



### 9.2.1 Spatial variation of the thermal conductivity

The thermal conductivity just reported represents an average value across the total thickness of the wax deposit. It was calculated based on the measured heat flux and on the angular coefficient of a linear fit, made over the temperature profile data. This calculation implicitly assumes that the temperature profile is linear. Indeed, the measurements of the temperature profiles obtained with the traversing temperature probe, reported in Chapter 6, indicate that, for the 7-hour tests, the profiles were linear for the three values of the Reynolds number investigated. A careful look at those data, however, reveals that there are slight changes in the profile inclination for different regions within the deposit thickness.

In the present section we attempt to explore those slight differences in the temperature profile inclinations and associate them with possible local variations of the deposit thermal conductivity. The decision whether the profile resulting from the adjustment of the measured data is represented by a single linear curve or by a set of linear curves, each one adjusted to a portion of the deposit thickness, is dictated by the level of experimental uncertainty associated to the data. Wider uncertainty bands can only accommodate a single curve adjusting the temperature data for the whole deposit thickness. On the other hand, tighter uncertainty bands may allow the use of different

fits for different regions in the deposit, thereby resulting in different values for the thermal conductivity across the wax deposit layer.

The procedure employed for estimating the local values of the thermal conductivity will now be outlined. To facilitate the description of the employed procedure, figures from Chapter 6 are reproduced here. They received a new number 9.3. These figures display the temperature profiles, measured with the temperature traversing probe, for the 7-hour experiments, for the three values of the Reynolds numbers investigated. As already mentioned, only for the 7-hour experiments, the temperature profiles indicated a linear behaviour, within the estimated uncertainty level. This fact was taken as a demonstration that heat transfer, within the deposit, was governed purely by conduction. Based on this finding, the 7-hour data were chosen to be employed in the present analyses.

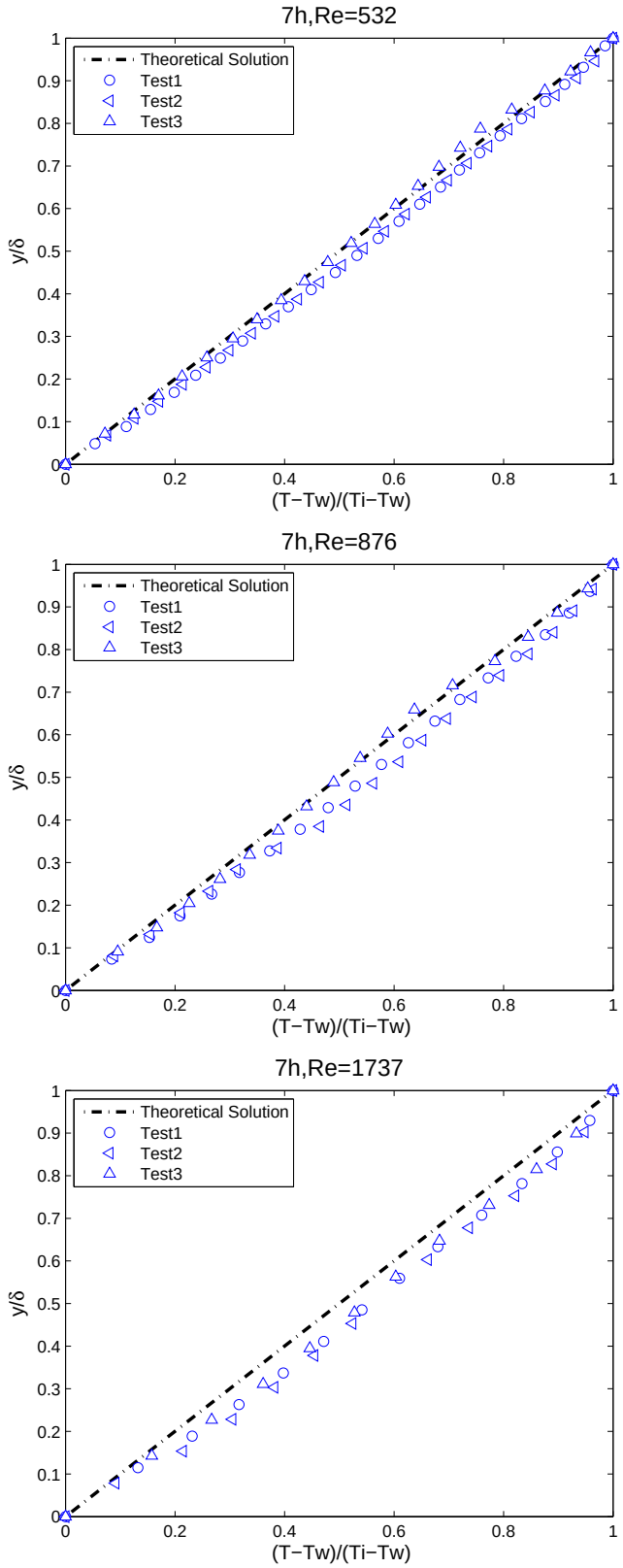


Figure 9.3: Dimensionless temperature profiles measured after seven hours from the beginning of the cooling process, for Reynolds number equal to 532, 876 and 1737.

The deposit thickness was divided in regions and the thermal conduct-

ivity of each region was determined based on the derivative of the temperature profile prevailing in each region, as in equation 9-1. The heat flux was taken as constant across all regions.

In each region, the derivative of the temperature profile was obtained by a linear fit, through the measured data, within the particular region of analysis. The number of regions in which the deposit was divided defined the spatial resolution obtained for the thermal conductivity of the deposit. An uncertainty analysis determined the maximum number of regions to be used. Too many regions implied in narrow regions, with a reduced number of temperature data points within the region, what increased the uncertainty in the calculation of the local value for the deposit thermal conductivity.

Also, the uncertainty analysis revealed that the main source of uncertainty was the size of the thermocouple junction. Although the probe was made of fine thermocouple wires, the size of the measuring junction did not allow that measurements were made in regions where elevated values of the temperature gradient prevailed. Setting a maximum limit of 15% for the uncertainty in the thermal conductivity value, the uncertainty analysis indicated that a maximum of three regions could be employed to determine the local values of the thermal conductivity. A larger number of regions would certainly be desired, but that would require smaller sensing thermocouple junctions and thicker deposits.

It should de mentioned that in the case of the highest Reynolds number, which produced the thinner deposit thicknesses, the limiting value of 15% was exceeded, and the highest uncertainty was 20%.

The measured values for thermal conductivity within the three regions, across the wax deposit, are presented in Figure 9.4. The figure displays results for the three values of the Reynolds numbers investigated. In the figure, the ordinate represents the transverse position, in dimensionless form relatively to the deposit thickness, i.e. zero represents the bottom wall and 1 represents the deposit-liquid interface. The abscissa gives the measured wax deposit thermal conductivity, $k_{exp}$.

The results displayed in the figure show that the thermal conductivity inside the deposit layer is a weak function of the flow Reynolds number, since the observed differences in thermal conductivity, for different Reynolds numbers, are within the estimated uncertainty levels.

An interesting finding obtained from the analysis of the data is that, for the three Reynolds numbers, the thermal conductivity is smaller in the region closer to the bottom wall of the test section. A careful examination of the temperature data close to the wall indeed shows a stronger temperature

gradient, as compared to the other regions away from the wall. For Reynolds numbers equal to 532 and 876, the differences between the thermal conductivity close to the wall and that close to the deposit liquid interface are of the order of 24% and 30%, respectively. For Reynolds number 1737 that difference dropped to only 20 %, which is a value of the order of the estimated uncertainty level for that case. So, this value should be interpreted with caution. However, for the two other values of Reynolds, the difference in thermal conductivity observed corresponds to twice the estimated uncertainty level. So, the finding that the thermal conductivity drops close to the wall seems to be a reliable piece of information.

A smaller value for the deposit thermal conductivity close to the cold wall was not an expected result. Indeed, the wall region is colder than the deposit–liquid interface region, and as n-alkanes tend to have thermal conductivities inversely proportional to the temperature, a higher value for the thermal conductivity should prevail close to the cold wall. However, one should recall that, in Chapter 8, it was mentioned that deposit samples had a non-uniform texture, being softer close to the cold wall, indicating that liquid was trapped in that region. A comparison between the measured deposit thermal conductivity, $k_{exp}$ and the thermal conductivity of wax in the solid phase, $k_s$, and $C_{12}$ in the liquid phase, $k_{C_{12}}$, is exhibited in Figure 9.5 and can be used to support the assumption of higher concentration of liquid close to the wall. The solid wax used for comparison in the figure had a melting point of 64 $^oC$ Ukrainczyk et al. (2010). The thermal conductivity of the solvent in the liquid phase, $k_{C_{12}}$, was obtained from the measurements of Tanaka. et al. (1988).

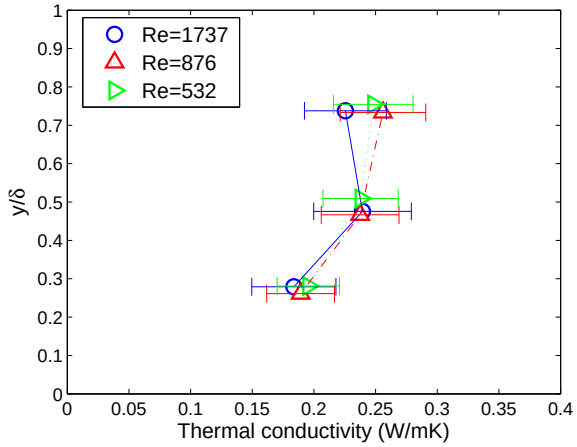


Figure 9.4: Thermal conductivity varying inside the deposit layer, for the three Reynolds number evaluated, 532, 876 and 1737.

In the figure, it is seen that the measured deposit thermal conductivity, $k_{exp}$, is bounded by the solid and liquid thermal conductivity values,

approaching the liquid value, at regions close to the bottom wall. This result indicates that comparatively more liquid could be entrapped close to the cold wall than close to the deposit–liquid interface, confirming the visual observations reported in Chapter 8.

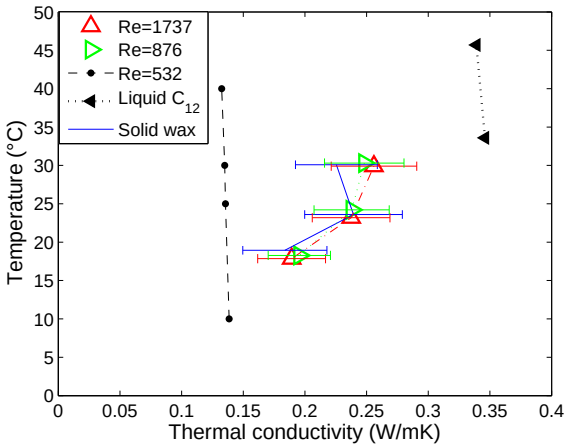


Figure 9.5: Thermal conductivity data in comparison with pure components thermal conductivity.



### 9.2.2
### Temperature based solid-fraction analysis

The results of Figure 9.5 suggest a methodology for estimating the wax liquid and solid contents, across the deposit thickness. The sensitivity observed of the measured thermal conductivity to the solid and liquid contents formed the basis for the prosed method, that will now be outlined.

Several theoretical models have been proposed in the literature that address to the thermal conductivity of heterogeneous materials Wang et al. (2006). Between the models cited in the work by Wang et al. (2006) the parallel and the Maxwell-Eucken are the most employed to address for wax deposits Singh et al. (2000, 2001a); Hernandez et al. (2003); Couto et al. (2006); Banki et al. (2008); Haj-Shafieia et al. (2014). In the present work the parallel model, described in equation 9-2, was employed.

$$\begin{aligned} k_{eff} &= k_s S_s + k_l(1 - S_s) \\ S_s &= \frac{(k_{eff} - k_l)}{(k_s - k_l)} \end{aligned} \tag{9-2}$$

The solid saturation of the deposit becomes an explicit function of the pure phases thermal conductivity and of the effective thermal conductivity of the deposit, measured in the present work. The solid and liquid thermal conductivities employed were obtained from the literature as mentioned before Ukrainczyk et al. (2010); Tanaka. et al. (1988). The thermal conductivity of

the liquid was considered to be equal to the solvent thermal conductivity in the liquid phase.

In the present experimental procedure it was possible to measure the variation of the deposit thermal conductivity across the deposit thickness. So, in principle, it should be possible to infer the deposit solid and liquid contents, at different positions across the deposit. The results for the deposit liquid fraction, obtained by the methodology proposed, are shown in figure 9.6. These values are presented for three dimensionless positions across the deposit thickness, where the coordinate zero corresponds to the bottom wall and the coordinate one to the deposit–liquid interface position. Indeed closest to the wall the liquid fraction is from 20 to 30% higher than close to the deposit–liquid interface for the three Reynolds number analysed. These results indicate that there seems to exist more liquid close to the cold wall. The results on the liquid fraction distribution can be rationalized with the aid of available results in the literature.

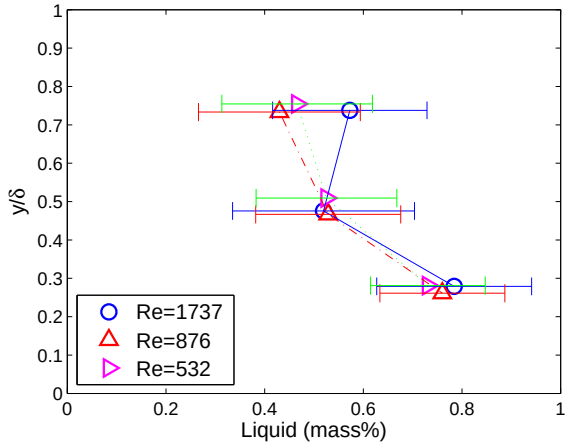


Figure 9.6: Estimative of the solvent content varying with the transversal coordinate inside the deposit layer.

Rheometry experiments have shown evidence of deposits expelling liquid when submitted to shear stress (Singh and Fogler (1999)). In that work the authors suggest that if the deposit is submitted to shear before the gelation is completed, it may expel liquid out to form a lubricating layer close to the cold wall. Singh et al. (2001a) suggest that thick deposits - deposits with thickness up to 50% of the pipe radius - may have non-homogeneous composition, while thin deposits - deposits with thickness up to 20% of the pipe radius - have homogeneous composition. The authors claim that if the deposit is thick, in the aging process, the diffusion of liquid out of the gel may get restricted. A characteristic diffusion length was used to model the non-uniform composition of thick deposits. In the authors view, the diffusion of liquid out of the gel

is restricted to the characteristic diffusion length. If the deposit thickness is bigger than that length, the diffusion of liquid may be inhibited.

In the work of Banki et al. (2008), a multisolid approch was used for predicting the solid–liquid equilibrium, coupled with molecular and thermal diffusion of species, resullting in non-homogeneous composition inside the deposit layer (Hoteit et al. (2008)). In that work, particularly, it was found a significant higher solid fraction close to the cold pipe wall, for higher wall temperatures. However for lower wall temperature and thick deposits a higher wax fraction was estimated close to the deposit–liquid interface. The authors attributed that behaviour to the multicomponent behaviour of thermal and molecular diffusion.

However other studies have shown that shear may induce crystallization and ordering of macromolecules (Koppi et al. (1993); Varga and Karger-Kocsis (1996)). Since in the deposit–liquid interface shear is the highest, it is possible that reorganization is taking place, preventing the entrapped liquid to leave the deposit layer. Further investigation is necessary to clarify those observations.



## 9.3 Conclusions

The experiments presented in the present chapter are, seemly, the first direct measurements of the thermal conductivity of wax deposit, under flowing conditions, available in the open literature. The results obtained in the rectangular channel test section have indicated no variation of the deposit thermal conductivity with the Reynolds number, for the range investigated.

An original technique was also implemented to enable the measurement of the deposit thermal conductivity as a function of the wall normal coordinate, across the deposit thickness. A non-uniform thermal conductivity was found within the deposit thickness, indicating that a less conductive material was present in regions close to the bottom cooling surface of the test section. This finding suggests the presence of liquid in that region. These measurements agreed with qualitative visualizations that also identified the presence of liquid close to the cold wall of the test section.

The local measurements of the deposit thermal conductivity indicated that the value of this property could be used to estimate the local deposit solid and liquid contents. A procedure was proposed and implemented to quantitatively estimate the liquid and solid content at different transverse positions in the deposit. The results confirmed the presence of higher liquid content close to the colder bottom wall of the channel. However, the procedure

proposed uses an integral information on the solvent composition that yielded unrealistic results for the deposit liquid content.

# 10
# Overview of the work

The present research provided original information to aid the understanding of the physical mechanisms governing wax deposition in pipelines. The research program addressed a number of relevant open questions in the literature regarding the formation, growth and aging of the wax deposit layer, by providing detailed local information on the deposit characteristics.

To this end, an experimental program was devised following a strategy of conducting simple experiments, employing lab-scale test sections with well-defined boundary and initial conditions, and using simple test fluids with known properties. The experiments were supported by detailed numerical simulations that faithfully modelled the test conditions. Comparisons between experiments and simulations helped to better understand the underlying mechanisms responsible for wax deposition and deposit aging.

The experimental program encompassed measurements performed in a rectangular and in an annular test section, both especially designed to allow for optical measurements of the time evolution of the spatial distribution of the wax deposit thickness. The test sections were equipped with heat flux sensor, temperature traversing probes and deposit sampling ports that allowed the measurement of relevant information on the deposit, such as, thermal conductivity, temperature profiles within the deposit, deposit–liquid interface temperature, and deposit composition.

Visual observations of the wax deposit formation in the annular test section revealed that wax crystals first appear close to the cold surface of the pipe when the surface reaches the WAT for the solution, and are convected by the flow. An immobile deposit layer is formed once a certain wax crystals solid saturation is attained, although a cloud of flowing crystals still existed over the deposited layer at the first instants of the immobile layer formation. The temporal and spatial evolution of the deposit layer were measured for different values of the laminar flow Reynolds number. Measurements were made since the start of the deposition, until the achievement of a steady state configuration of the deposit thickness.

Excellent agreement was obtained between measured values of the

deposit thickness and predictions from a numerical model developed previously in our research group. This excellent level of agreement was verified since the early stages of the deposition process, until steady state, for the range of laminar Reynolds numbers investigated. The numerical model employed in the comparisons and developped by Souza (2014) solved the coupled equations governing the fluid flow, heat, mass and concentration fields, together with a multi-solid thermodynamic model, yielding the spatial and temporal distributions of the components of the test mixture, temperature and velocity fields, as well as the deposit thickness, solid fraction, and chemical composition.

The high quality of the agreement obtained in the present study was never achieved in our previous experiments, and it is attributed to the excellent control of the test conditions, to the proper characterization of the simple solution employed in the tests, and to the well-developed and complete simulation model employed.

The measurements of the wax deposit growth, together with the measurements of the evolving deposit–liquid interface temperature obtained with a fine–gage traversing temperature probe, allowed the proposition of the following scenario for the deposit formation. As the wall is cooled, the necessary degree of sub–cooling for initiation of crystallization is attained, and the first layer of crystals attached to the wall is formed. This process occurs at temperatures less or equal to the WAT measured for the solution by microscopy. Once crystals are present at the wall, they act as nucleation sites for further crystallization, and the necessary degree of sub-cooling to form new crystals is no longer as large, so the deposition front progresses at temperatures above the WAT, as evidenced by the interface temperatures measured employing the traversing probe. The temperature growth of the deposit interface continues up to the limit of the WDT, the wax disappearance temperature, the maximum temperature that a solid phase can exist.

This scenario contradicts most models available in the literature that employ a molecular diffusion mass flux at the interface as a mechanism for deposit growth. In these models, the interface temperature is always below the WAT, and deposition ceases when the WAT is attained.

The temperature traversing probe was also employed to obtain information on the temperature profiles within the wax deposit layer under flowing conditions. This is a relevant and original piece of information that can be used to verify the prevailing heat transfer regime within the deposit. Most models in the literature assume that pure conduction is the prevailing heat transfer mechanism in the deposit layer. A comparison of the measured temperature profiles within the deposit with the theoretical, one-dimensional heat conduc-

tion solution was used to assess the possible presence of liquid flow in the deposit porous matrix. Conceivably, this flow would be induced by shear at the interface imposed by the bulk flow over the deposit. The measured profiles obtained indicated that a deviation from the purely conductive temperature profiles existed for the higher values of the Reynolds numbers, where shear is larger, and for the initial stages of the deposition process, when the deposit is more permeable. This is an indication that liquid flow may be present in the deposit matrix and contribute to the heat and mass transfer processes. For lower values of the Reynolds numbers and for longer deposition times, the measured temperature profiles agreed with the purely-conductive profiles.

The rectangular test section was equipped with a traversing temperature probe, a heat flux sensor and thermocouples mounted in the wall over which the wax deposition occurred. These measurements allowed the determination of the thermal conductivity of the wax deposit measured under flowing conditions. The results obtained demonstrated that the wax deposit thermal conductivity did not vary with shear rate, for the range of laminar Reynolds numbers tested and for the cooling rate employed. The values obtained for the deposit thermal conductivity were bounded by the values of the thermal conductivity for the solvent in the liquid phase and that of the wax in the solid phase.

The traversing temperature probe was used to measure the variation of the deposit thermal conductivity across the deposit thickness. Although limited by the uncertainty levels obtained at some operational conditions of the experiments, the results revealed variations of the thermal conductivity across the deposit. For instance, close to the cold wall the presence of a less conductive deposit was detected and associated with a higher liquid content within the deposit in that region.

The variation of the measured thermal conductivity was employed as a technique to estimate the solid and liquid contents of the deposit. Although approximate and limited by experimental uncertainty, profiles of solid and liquid fraction within the deposit were obtained under flowing conditions.

Deposit samples were obtained from both, the rectangular and annular test sections, and analysed by high temperature gas chromatography, for the range of the laminar Reynolds numbers tested and for different durations of the deposition experiments. The analyses revealed that the carbon distributions of the deposit samples presented a shift toward higher carbon numbers both, with increasing deposition time and Reynolds number, characterizing the aging process of the deposit. The carbon number distributions were seen to display an asymptotic behaviour with Reynolds number, for samples obtained from

the final portion of the longer deposition lengths of the annular test section.

Critical carbon number values were identified to be the same for the two test section and different values of the Reynolds numbers, indicating that the critical carbon number value is dependent on the test solution properties, and not on the flow characteristics. This conclusion, however, should be further investigated, since the critical carbon number identification was associated with high levels of experimental uncertainties.

As it commonly occurs, the research conducted offered valuable information, but raised other issues that deserve further investigation. The extension of the experiments to turbulent Reynolds numbers is a natural suggestion for future work. Also, the investigation of different cooling rates and bulk-to-wall temperature differences seems necessary. From the stand point of the experimental setup, an effort should be devoted to reduce the uncertainty of the measurements, in particular, those associated with the traversing temperature probe. Improved sampling techniques would, conceivably, yield information on the transverse variation of the deposit composition at different deposit axial locations.

The present research produced data of excellent quality, obtained under controlled conditions and employing fluids with well–defined properties. Local information on the deposit temperature profiles and composition were also provided. These data offer an opportunity for definitive testing of simulation codes that employ different deposition models and thermodynamic calculations. This is, perhaps, the most valuable contribution of the present work.

## Bibliography


Aiyejina, A., Chakrabarti, D. P., Pilgrim, A., and Sastry, M. K. S. (2011). Wax formation in oil pipelines: A critical review. *Journal of Multiphase Flow*, **37**:671–694.

Al-Syabi, Z., Danesh, A., Tohidi, B., Todd, A. C., and Tehrani, D. H. (2001). A residual viscosity correlation for predicting the viscosity of petroleum reservoir fluids over wide ranges of pressure and temperature. *Chemical Engineering Science*, **56**:6997–7006.

Azevedo, L. F. A. and Teixeira, A. M. (2003). A critical review of the modeling of wax deposition mechanisms. *Petroleum Science and Technology*, **21**(3 and 4).

Bahadori, A. and Mokhatab, S. (2008). Estimating thermal conductivity of hydrocarbons. *Chemical Engineering*.

Banki, R., Hoteit, H., and Firoozabadi, A. (2008). Mathematical formulation and numerical modeling of wax deposition in pipelines from enthalpy-porosity approach and irreversible thermodynamics. *Internatinal Journal of Heat and Mass Transfer*, **51**(3387–3398).

Bhat, N. V. and Mehrotra, A. K. (2004). Measurement and prediction of the phase behavior of wax-solvent mixtures significance of the wax disappearance temperature. *Industrial Engineering Chemistry Research*, **43**(13):3451–3461.

Bhat, N. V. and Mehrotra, A. K. (2005). Modeling of deposit formation from "waxy" mixtures via moving boundary formulation:radial heat transfer under static and laminar flow conditions. *Industrial Engineering Chemistry Research*, **44**(17).

Bhat, N. V. and Mehrotra, A. K. (2008). Modeling the effect of shear stress on the composition and growth of the deposit layer from waxy mixtures under laminar flow in a pipeline. *Energy and Fuels*, **22**(5).

Bidmus, H. and Mehrotra, A. K. (2008a). Measurements of the liquid-deposit interface temperature during solid deposition from wax-solvent mixtures under sheared cooling. *Energy and Fuels*, **22**(6).

Bidmus, H. and Mehrotra, A. K. (2008b). Measurements of the liquid-deposit interface temperature during solid deposition from wax-solvent mixtures under static cooling conditions. *Energy and Fuels*, **22**(2).

Bidmus, H. O. and Mehrotra, A. K. (2004). Heat-transfer analogy for wax deposition from paraffinic mixtures. *Industrial Engineering Chemistry Research*, **43**(3).

Bott, T. R. and Gudmundsson, J. S. (1977). Deposition of paraffin wax from kerosene in cooled heat exchanger tubes. *The Canadian Journal of Chemical Engineering*, **55**.

Brenner, H. (1966). Hydrodynamic resistance of particles at small reynolds numbers. *Advances in Chemical Engineering*, **6**(1).

Brent, A. D., Voller, V. R., and Reid, K. J. (1988). Enthalpy porosity technique for modeling convection-diffusion phase-change: application to the melting of pure metal. *Numerical Heat Transfer*, **13**(3):297–318.

Brown, T. S., Niesen, V. G., and Erickson, D. D. (3-6 October 1993). Measurement and prediction of the kinetics of paraffin deposition. In *SPE annual technical conference and exhibition.*

Burger, E. D., Perkins, T. K., and Striegler, J. H. (1981). Studies of wax deposition in the trans alaska pipeline. *Journal of Petroleum Technology*, pages 1075–1086.

Cabanillas, J. P., Leiroz, A. T., and Azevedo, L. F. A. (2016). Wax deposition in the presence of suspended crystals. *Energy and Flues*, **30**:1–11.

Calado, J. C. G., Fareleira, J. M. N. A., Mardolcar, U. V., and de Castro, C. A. N. (1988). Thermal conductivity of liquid n-alkanes. *International Journal of Thermophysocs*, **9**(3):352–363.

Carman, P. C. (1937). Fluid flow through granular beds. *Transactions of the Institution of Chemical Engineers*, **15**:150–166.

Carslaw, H. S. and Jaeger, J. C. (1959). *Conduction of heat in solids.* Oxford University Press, 2nd ed edition.

Cordoba, A. J. and Schall, C. A. (2001). Solvent migration in a paraffin deposit. *Fuel*, **80**:1279–1284.

Correra, S., Fasano, A., Fusi, L., and Merino-Garcia, D. (2007). Calculating deposit formation in the pipelining of waxy crude oils. *Meccanica*, **165**:149–165.

Couto, G. H., Chen, H., Dellecase, E., Sarica, C., and Volk, M. (1-4 may 2006). An investigation of two-phase oil water paraffin deposition. In *Offshore Technology Conference*.

Cox, R. G. and Mason, S. G. (1971). Suspended particles in fluid flow through tubes. *Annual Review of Fluid Mechanics*, **3**(1).

Creek, J. L., Lund, H. J., Brill, P. J., and Volk, M. (1999). Wax deposition in single phase flow. *Fluid Phase Equilibria*, **158-160**:801–811.

da Silva, J. A. L. and Coutinho, J. A. P. (2007). Analysis of the isothermal structure development in waxy crude oils under quiescent conditions. *Energy and Fuels*, **21**(6).

Dauphin, C., Daridon, J. L., Coutinho, J., Baylère, P., and Potin-Gautier, M. (1999). Wax content measurements in partially frozen paraffinic systems. *Fluid Phase Equilibria*, **161**:135–151.

Fey, U., M.König, and Eckelmann, H. (1998). A new strouhal reynolds number relationship for the circular cylinder in the range 47 re 23105. *Physics of Fluids*, **10**:1547–1549.

Firoozabadi, A. (1999). *Thermodynamics of hydrocarbon reservoirs*. McGraw-Hill.

Guozhong, Z. and Gang, L. (2010). Study on the wax deposition of waxy crude in pipelines and its application. *Journal of Petroleum Science and Engineering*, **70**:1–9.

Haj-Shafieia, S., Serafini, D., and Mehrotra, A. K. (2014). A steady-state heat-transfer model for solids deposition from waxy mixtures in a pipeline. *Fuel*, **137**:346–359.

Hamouda, A. A. and Davidsen, S. (14-17 Februrary 1995). An approach for simulation of paraffin deposition in pipelines as a function of flow characteristics with a reference to teesside oil pipeline. In *SPE International Symposium on Oilfield Chemistry*.

Hayduk, W. and Minhas, B. S. (1982). Correlations for prediction of molecular diffusivities in liquids. *The Canadian Journal of Chemical Engineering*, **60**:295–299.

Hennecke, D. K. and Sparrow, E. M. (1970). Local heat sink on a convectively cooled surface - application to temperature measurement error. *International Journal of heat and mass transfer*, **13**:287–304.

Hernandez, O. C., Hensley, H., Sarica, C., Brill, J. P., Volk, M., and Delle-case, E. (5-8 October 2003). Improvements in single-phase paraffin deposition modeling. In *Spe Annual Technical Conference and Exhibition*.

Himran, S. and Suwono, A. (1994). Characterizarion of alkanes and paraffin waxes for application as phase change energy storage medium. *Energy Sources*, **16**:117–128.

Ho, B. P. and Leal, L. G. (1974). Inertial migration of ridig spheres in two-dimensional unidirectional flows. *Journal of Fluid Mechanics*, **65**(1).

Hoffmann, R. and L.Amundsen (2010). Single-phase wax deposition experiments. *Energy and Fuels*, **24**:1069–1080.

Holder, G. A. and Winkler, J. (1965). Wax crystallization from distillate fuels. *Journal of the Institute of Petroleum*, **51**(499).

Holmen, R., Lamvik, M., and Melhus, O. (2002). Measurements of the thermal conductivities of solid and liquid unbranched alkanes in the c16 to c19 range during phase transition. *International Journal of Thermophysics*, **23**(1).

Hoteit, H., Banki, R., and Firoozabadi, A. (2008). Wax deposition and aging in flowlines from irreversible thermodynamics. *Energy and Fuels*, **22**(4).

Huang, Z., Lee, H. S., Senra, M., and Fogler, H. S. (2011). A fundamental model of wax deposition in subsea oil pipelines. *Aiche Journal*, **57**(11).

Huang, Z., S.Zheng, and Fogler, H. S. (2015). *Wax Deposition Experimental characterisations theoretical modeling and fields practices*. CRC Press.

Hunt, E. B. (1962). Laboratory study of paraffin deposition. *Journal of Petroleum Technology*, **14**(11).

H.Watanabe and Seong, D. J. (2002). The thermal conductivity and thernal diffusivity of liquid n-alkanes: Cnh2n+2 n=5t o 10 and toluene. *International Journal of Thermophysics*, **23**(2):337–356.

Jessen, F. W. and Howell, J. N. (1958). Effect of flow rate in paraffin accumulation in plastic, steel, and coated pipe. *Petroleum transactions*, **213**.

Kang, P. and andJ.Lim, D. L. (15-20 June 2014). Status of wax mitigation technologies in offshore oil production. In *International Ocean and Polar Engineering Conference*.

Kasumu, A. S. and Mehrotra, A. K. (2015). Solids deposition from wax-solvent-water waxy mixtures using a cold finger apparatus. *Energy and Fuels*, **29**:501–511.

Konstantinov, V. A., Revyakin, V. P., and Sagan, V. V. (2009). Isochoric thermal conductivity of solid n-alkanes: propane c3h8. *Low temperature physics*, **35**.

Konstantinov, V. A., Revyakin, V. P., and Sagan, V. V. (2011). Isochoric thermal conductivity of solid n-alkanes: propane c6h14. *Low temperature physics*, **37**.

Koppi, K. A., Tirrell, M., and Bates, F. S. (1993). Shear-induced isotropic-to-lamellar transition. *Physical Review Letters*, **70** .

Lira, C. H. S. (2001). Solidification in square section. *Theoria*, **10**:47–56.

Lira-Galeana, C., Firoozabadi, A., and Prausnitz, J. M. (1996). Thermodynamics of wax precipitation in petroleum mixtures. *Thermodynamics*, **42**(1).

Lira-Galeana, C. and Hammami, A. (2000). Wax precipitation from petroleum fluids a review. *Developments in petroleum Science*, **40**.

Matzain, A., Apte, M. S., Zhang, H.-Q., Volk, M., Brill, J. P., and Creek, J. L. (2002). Investigation of paraffin deposition during multiphase flow in pipelines and wellbores- part1:experiments. *Journal of Energy Resourses Technology*, **124**.

Matzain, P. (1999). *Multiphase flow paraffin deposition*. PhD thesis, The University of Tulsa.

MBaye, M. and Bilgen, E. (2001). Phase change process by natural convection diffusion in rectangular enclosures. *Heat Mass Transfer*, **37**(1):35–42.

Merino-Garcia, D., Mergarone, M., and Correra, S. (2007). Kinectics of waxy gel formation from batch experiments. *Energy and Fuels*, **21**(3).

Michelsen, M. L. (1982). The isothermal flash problem: I. stability. *Fluid Phase Equilibria*, **9**:1–19.

Nabil, M. and Khodadabi, J. M. (2013). Experimental determination of the temperature-dependent thermal conductivity of solid-eicosane-based nanostructure-enhanced phase change materials. *International Journal of heat transfer*, **67**:301–310.

Patton, C. C. (1970). Paraffin deposition from refined wax-solvent systems. *Society of Petroleum Engineers Journal*, **10**(1).

Pedersen, K. S., Skovborg, P., and Ronningsen, H. P. (1991). Wax precipitation from north sea crude oils. 4. thermodynamic modeling. *Energy and Fuels*, **5**(6).

Peng, D. Y. and Robinson, D. B. (1976). A new two-constant equation of state. *Industrial and Engineering Chemistry: Fundamentals*, **15**:59–64.

Pimentel, D. M. (2013). Experimental study of wax deposition on coated surfaces. Master's thesis, Pontifical University of Rio de Janeiro.

R.Hoffmann, L.Amundsen, Z.Huang, S.Zheng, and H.S.Fogler (2012). Wax deposition in stratified oil/water flow. *Energy and Fuels*, **26**:3416–3423.

Ronningsen, H. P., Bjorndal, B., Hansen, A. B. E., and Pedersen, W. B. (1991). Wax precipitation from north sea crude oils. 1. crystallization and dissolution temperatures, and newtonian and non-newtonian flow properties. *EnergyandFuels*, **5**(6).

Segrè, G. and Silberberg, A. (1962). Behavior of macroscopic ridig spheres in poiseuille flow, part1. *Journal of Fluid Mechanics*, **14**(136).

Silva, J. A. L. and Coutinho, J. A. P. (2004). Dynamic rheological analysis of the gelation behaviour of waxy crude oils. *Rheologic Acta*, **43**:433–441.

Singh, P. and Fogler, H. S. (1999). Prediction of the wax content of the incipient gel wax-oil gel in a pipeline: An application of the controled-stress rheometer. *Journal of Rheology*, **43**(6).

Singh, P., Venkatesan, R., and Fogler, H. S. (2001a). Morphological evolution of thick wax deposits during aging. *Aiche Journal- Fluid Mechanics and Transport Phenomena*, **47**(1).

Singh, P., Venkatesan, R., Fogler, H. S., and Nagarajan, N. (2000). Formation and aging of incipient thin film wax-oil gels. *Aiche Journal-Materials, Interfaces and Electrochemical*, **46**(5).

Singh, P., Youyen, A., and Fogler, H. S. (2001b). Existence of a critical carbon number in the aging of a wax-oil gel. *Aiche Journal- Thermodynamics*, **47**(9).

Snyder, R. G., Conti, G., Strauss, H. L., and Dorset, D. L. (1993). Thermally-induced mixing in patially microphase segregated binary n-alkane crystals. *Journal of Physical Chemistry*, **97**(28).

Snyder, R. G., Goh, M. C., Srivatsavoy, V. J. P., Strauss, H. L., and Dorset, D. L. (1992). Measurements of the growth kinetics of microdomains in binary n-alkane solid solutions by infrared spectroscopy. *Journal of Physical Chemistry*, **96** (24).

Souza, L. B. (2014). *Wax deposition in pipelines: numerical and experimental study.* PhD thesis, PUC-Rio University.

Stryker, P. C. and Sparrow, E. M. (1990). Application of a spherical thermal conductivity cell to solid n-eicosane paraffin. *International Journal of Heat and Mass Transfer*, **33**(9).

Tanaka., Y., Itani, Y., Kubota, H., and Makita, T. (1988). Thermal conductivity of five normal alkanes in the temperature range 283-373 k at pressures up to 250 mpa. *International Journal of Thermophysics*, **9**(3).

Tinsley, J. F. and Prud'homme, R. K. (2010). Deposition apparatus to study the effects of polymers and asphaltenes upon wax deposition. *Journal of Petroleum Science and Engineering*, **72**:166–174.

Ukrainczyk, N., Kurajica, S., and Sipusic, J. (2010). Thermophysical comparison of five commercial paraffin waxes as latent heat storage materials. *Chemical and Biochemical Engineering Quaterly*, **24**:129–137.

Varga, J. and Karger-Kocsis, J. (1996). Rules of supermolecular structure formation in sheared lsotactic polypropylene melts. *Journal of Polymer Science: Part B: Polymer Physics*, **34**:657–670.

Veiga, H. B., Souza, L. B., Minchola, L., Palomino, L. F., Nieckele, A. O., and Azevedo, L. (1-6 July 2012). Wax deposition in laminar and turbulent flow in pipelines. In *International Conference on Ocean, Offshore and Artic Engineering.*

Vélez, C., de Zárate, J. M. O., and Khayet, M. (2015a). Thermal properties of n-pentadecane, n-heptadecane and n-nonadecane in the solid/liquis phase change region. *International Journal of Thermal Science*, **94**:139–146.

Vélez, C., Khayet, M., and de Zárate, J. M. O. (2015b). Temperature-dependent thermal properties of solid/liquis phase change even-numbered n-alkanes:n-hexadecane, n-octane and n-eicosane. *Applied Energy*, **143**:383–394.

Venkatesan, R. and Fogler, H. S. (2004). Comments on analogies for correlated heat and mass transfer in turbulent flow. *AIche Journal-RandD Notes*, **50**(7).

Venkatesan, R., Nagarajan, N. R., Paso, K., Yi, Y.-B., Sastry, A. M., and Fogler, H. S. (2005). The strensth of paraffin gels formed under static and flow conditions. *Chemical Engineering Science*, **60**:3587–3598.

Voller, V. R. and Prakash, C. (1987). A fixed grid numerical modeling methodology for convection-diffusion mushy region phase-change problems. *Journal of Heat and Mass Transfer*, **30** (18):1709–1719.

Wang, J., Carson, J. K., North, M. F., and Cleland, D. J. (2006). A new approach to modelling the effective thermal conductivity of heterogeneous materials. *International Journal of Heat and Mass Transfer*, **49**:3075–3083.

Weingarten, J. S. and Euchner, J. A. (1988). Methods for predicting wax precipitation and deposition. *Spe Production Engineering*, pages 121–126.

Williamson, C. H. K. (1988). Defining a universal and continuous strouhal-reynolds number relationship for the laminar vortex shedding of circular cylinder. *Physics of Fluids*, **31**:2742–2744.

# 11
# Appendix A

## 11.1
## Mathematical Modelling

In this chapter a brief description is given of the mathematical model employed to simulate the wax deposition process in the annular channel. This model was developed in the work of Souza (2014), and its predictions were used in the present work to gain insight into the deposition phenomena. The experimental data obtained for the transient spatial distribution of the wax deposit thickness in the annular channel test section were compared with the predictions of the numerical model developed to solve the set of equations forming the mathematical model.

### 11.1.1
### General description of the mathematical model

The model developed solves the axisymmetric, two-dimensional version of the governing equations for momentum, temperature and species concentration, together with a multi-solid phase thermodynamic calculation to solve for the local solid-liquid equilibrium. The main outputs are the velocity, temperature, species concentration and solid fraction fields, both, in the deposit and in the liquid phase of the solution. The transient axial distribution of the deposit thickness is also predicted. The computational domain employed was defined so as to reproduce the annular test section described in Chapter 3.

The model was based on the enthalpy-porosity approach proposed by Banki et al. (2008). One of the main features of this model is the unified treatment of the computational domain, without any separation from liquid flow and solid deposits. As will be detailed, the momentum equation incorporates a source term controlled by the local value of the solid fraction, what allows the calculation of the flow fields in the bulk, as well as within the porous deposit.

The following assumptions were made in the model:

- Two-dimensional, axisymmetric, laminar flow
- Newtonian fluid
- Constant molar heat capacity of each component in the solid phase
- Negligible molecular diffusion in the axial direction
- Brownian diffusion, shear dispersion and deposition by gravity neglected
- The Peng-Robinson cubic equation of state (Peng and Robinson, 1976) was employed to calculate the density, the variation of molar enthalpy and the fugacities of the mixture in the liquid phase (Firoozabadi, 1999).

### 11.1.2 Local Solid–Liquid Equilibrium

The multisolid–phase thermodynamic model proposed by Lira-Galeana et al. (1996) was employed in the local solid–liquid equilibrium. To estimate thecomposition of a new state, the model performs a two-step procedure, namely, the stability analysis and the composition calculation (Banki et al., 2008).

The stability analysis determines the nature of the components which precipitate for a given condition of temperature, pressure and composition. A component $i$ precipitates if Michelsen (1982):

$$f_{o,i}(P,T,z_i) - f_{s,i}^{pure}(P,T) \geq 0 \tag{11-1}$$

where $f_{o,i}(P,T,z_i)$ is the fugacity of component $i$ in the liquid (oil) phase with composition $z_i$ and $f_{s,i}^{pure}(P,T)$ is the fugacity of pure component $i$ in the solid phase.

After the stability analysis, a material balance is held to calculate the new composition. This process produces a final stable solid phase that consists predominantly of pure components (Pedersen et al., 1991; Ronningsen et al., 1991; Snyder et al., 1992, 1993).

### 11.1.3 Governing Equations

The velocity, pressure, temperature and composition fields are required as an input to the local solid–liquid equilibrium calculation. Those fields derive from the solution of the governing equations, which will be presented next.

Wax deposition is a free boundary problem. Transformed and fixed grids are the two main approaches to solve this kind of problem. In the first one, a generalized curvilinear coordinate system is required. In the second method, a fixed grid is applied, and the interface conditions are accounted by the definition of appropriate source terms. The fixed grid technique, known as the enthalpy-porosity approach, has been successfully used in some studies (Voller and Prakash, 1987; Brent et al., 1988; Lira, 2001; MBaye and Bilgen, 2001).

The present model adopts an enthalpy-porosity approach based on the work of Banki et al. (2008). As already mentionned, based on its multiphase composition, wax deposits have been associated with a porous medium where the liquid represents the pores (Holder and Winkler, 1965; Singh et al., 2000, 2001a). Hence, Banki et al. (2008) added a Darcy type source term to the linear momentum equations in order to describe the flow deceleration in the gel. As the solid phase appears in the domain, the source term dominates and the momentum equation is transformed in Darcy's equation that prevails where the solid content is higher.

#### Mass Conservation Equation

Since the solid is a non moving phase, the mass conservation equation for the domain is:

$$\frac{\partial}{\partial t}(S_o\rho_o + S_s\rho_s) + \nabla.(S_o\rho_o\mathbf{u}) = 0 \tag{11-2}$$

where $S_s$ is the solid saturation, $S_o$ is defined as the porous medium porosity ($S_o = 1 - S_s$), $\rho_s$ is the solid density, $\mathbf{u}$ is the velocity vector of liquid phase, and $\rho_o$ is the density in the liquid phase, calculated from:

$$\rho_o = \frac{M_o}{v} = \frac{P}{Z}\frac{M_o}{RT} \tag{11-3}$$

where $M_o$ is the molecular weight of the liquid phase, $v$ is the molar specific volume, $P$ is the pressure, $Z$ is the compressibility factor given from PR-EOS, $R$ is the gas constant and $T$ is the temperature.

### Linear Momentum Equation

The linear momentum conservation equation for the domain is:

$$\frac{\partial}{\partial t}(S_o\rho_o\mathbf{u}) + \nabla.(S_o\rho_o\mathbf{uu}) = -S_o\nabla p + \nabla.(S_o\tau) \tag{11-4}$$

where $\tau$ is the viscous stress tensor.

The deceleration in the porous medium in described by adding the following source term $S_{poro}$ to the right side of the linear momentum equation (Voller and Prakash, 1987; Banki et al., 2008):

$$S_{poro} = -\Lambda\mathbf{u} \tag{11-5}$$

where $\Lambda$ is a function of the gel porosity, such that in the liquid region, where the porosity $S_o$ is equal to one, $\Lambda$ is zero. The flow in the gel is described by a Darcy type equation where the pressure gradient is written as:

$$\nabla p = -\frac{\mu}{K}\mathbf{u} \tag{11-6}$$

where $\mu$ is the dynamic viscosity of the fluid, calculated from Lohrenz, Bray and Clark correlation for reservoirs multicomponent fluids given in Al-Syabi et al. (2001), and $K$ is the effective permeability of the medium, which can be related to the porosity, $S_o$, by the Carman-Koseny expression (Carman, 1937):

$$K = \frac{1}{C}\frac{S_o^3}{(1-S_o)^2} \tag{11-7}$$

By combining equations 11-5, 11-6 and 11-7,

$$\Lambda = C\mu\frac{(1-S_o)^2}{S_o^2} \tag{11-8}$$

where $C$ is a constant whose value depends on the morphology of the medium. In the present model, preliminary experiments were used to estimate this parameter, as made by Banki et al. (2008) and Hoteit et al. (2008). The value of $C = 10^9 m^{-2}$ showed the best fit to the experimental data, and was used to represent the morphology of the porous medium made of wax crystallites for our simulated cases.

As the formation of solid begins, the solid fraction increases and the value of porosity $S_o$ drops gradually. In the deposit, $\Lambda$ dominates over the transient, convective and diffusive terms. Thus, the momentum equation approaches the Darcy's law, representing the deposit as a porous medium adequately. Over time, the solid fraction increases and the deposit becomes less porous.

### Energy Equation

The energy equation in terms of temperature for the domain can be written as:

$$\frac{\partial}{\partial t}(S_o\rho_o T) + \nabla.(S_o\rho_o \mathbf{u}T) = \nabla.(\frac{k_{ef}}{Cp_o}\nabla T) + \frac{1}{Cp_o}\frac{\partial(S_s\rho_s)}{\partial t}[(H_o - Cp_oT) - (H_s - Cp_sT)] + \frac{k_{ef}}{Cp_o}\nabla T.\frac{1}{cp_o}\nabla Cp_o - \frac{Cp_s}{Cp_o}[\frac{\partial}{\partial t}(S_s\rho_s T)] \tag{11-9}$$

where $H_o$ and $H_s$ are the enthalpies of the liquid and solid phases, respectively. $Cp_o = \frac{\Delta H_o}{\Delta t}$ and $Cp_s = \Sigma_{i=1}^{n} x_{s,i} Cp_{s,i}$. $x_{s,i}$ is the molar fraction of component $i$ in the solid phase, and $Cp_{s,i}$ is the heat capacity of component $i$ in solid phase. The effective thermal conductivity, $k_{ef}$, was calculated from the Maxwell's correlation Carslaw and Jaeger (1959):

$$k_{ef} = \frac{2k_o + k_s - 2S_s(k_o - k_s)}{2k_o + k_s + S_s(k_o - k_s)}k_o \tag{11-10}$$

where $k_o = \Sigma_{i=1}^{n} x_{o,i} * k_i$ and $k_s = \Sigma_{i=1}^{n} x_{s,i} * k_i$. The $x_{o,i}$ is the molar fraction of component $i$ in liquid phase. The thermal conductivity of components $i$, $k_i$, were calculated by the correlation in Bahadori and Mokhatab (2008).

The molar enthalpy of the liquid phase, $\bar{H}_o$, was computed from PR-EOS (Firoozabadi, 1999), while the molar enthalpy of the solid phase, $\bar{H}_s$, was calculated from Banki et al. (2008):

$$\bar{H}_s(P, T, x_s) = \Sigma_{i=1}^{n} x_{s,i} * \bar{H}_{s,i} \tag{11-11}$$

$$\bar{H}_{s,i}(P, T) = \bar{H}_{o,i}(P_i^f, T_i^f) - \lambda_i + Cp_{s,i}(T - T_i^f) \tag{11-12}$$

where $\lambda_i$ is the molar latent heat of component $i$, which can be assumed constant. $P_i^f$ and $T_i^f$ are the melting point, pressure and temperature of component $i$, respectively. The values of $Cp_{s,i}$ and $\lambda_i$ were taken from Himran and Suwono (1994). The molar enthalpy of component $i$ at the melting point, $\bar{H}_{o,i}(P_i^f, T_i^f)$, was estimated also from PR-EOS. With the molar enthalpies, one can obtain the enthalpies in liquid and solid phases, $H_o$ and $H_s$, for the energy equation.

### Species Balance Equations

Neglecting velocity and diffusion in the solid phase, one obtains the species balance equations for $i = 1 : n - 1$,

$$\frac{\partial}{\partial t}(cz_i) + \nabla.(cz_i\mathbf{u}) = -\nabla.(S_o\mathbf{J}_{o,i}) + \nabla.(S_s c_s x_{s,i}\mathbf{u}) \tag{11-13}$$

where $cz_i$ is a variable defined as $cz_i = S_o c_o x_{o,i} + S_s c_s x_{s,i}$. Here, $c_s$ is the molar density of solid phase and $\mathbf{J}_{o,i}$ is the molar diffusion flux of component $i$ in liquid phase, which is written as:

$$\mathbf{J}_{o,i} = -c_o D_M \nabla x_{o,i} \tag{11-14}$$

Equation 11-14 represents the molecular diffusion, where the driving force is the concentration gradient $\nabla x_{o,i}$. $D_M$ is the molecular diffusion coefficient, which was determined using the Hayduk and Minhas correlation Hayduk and Minhas (1982).

To complete the species balance, the total molar balance equation is:

$$\frac{\partial c}{\partial t} + \nabla.(S_o c_o \mathbf{u}) = 0 \tag{11-15}$$

### 11.1.4 Initial and Boundary Conditions

The developed model was used to predict deposition in the experimental annular setup built and employed in this work, and described in chapter 3. Figure11.1 illustrates the physical domain. The copper pipe outer diameter was of 19 mm while the plexiglass pipe inner diameter was of 34 mm, thereby forming an annular space of 7.5 mm. The copper pipe length was, L, equal to 1.05 m.

### 11.1.5 Solution Composition

The solvent–wax solution used in the experiments, based on WAX2, and described in Chapter 4, was employed as the multicomponent fluid in the simulations. The composition of solution is listed in Table 11.1. The properties of these components were calculated from correlations suggested in the work of Souza (2014).

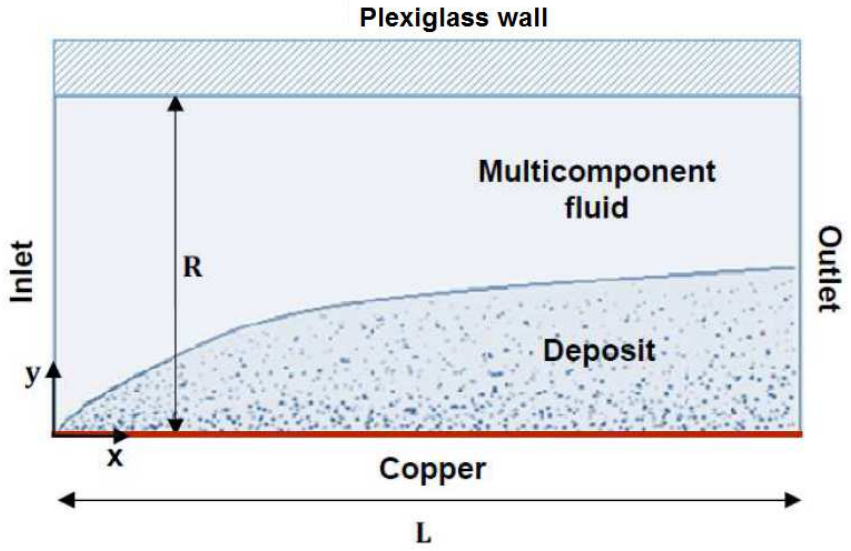


Figure 11.1: Schematic view of the computational domain.

### 11.1.6 Boundary and initial conditions

The following initial and boundary conditions were considered to solve equations 11-2, 11-4, 11-9, 11-13 and 11-15. The problem was solved on a cylindrical coordinate system. At the inlet, all variables were set as having an uniform profile. The inlet mixture temperature is $T_{in} = 38^oC$, the overall composition of the species was uniform (feed composition), and a uniform velocity profile was considered. The multicomponent fluid was injected at the inlet with constant volumetric flow rate, Q. The equations below summarize the conditions adopted,

$$T(x=0,y,t) = T_{in} \quad (11\text{-}16)$$

$$z_i(x=0,y,t) = (z_i)_{in} \quad (11\text{-}17)$$

$$U(x=0,y,t) = u_m \quad (11\text{-}18)$$

$$V(x=0,y,t) = 0 \quad (11\text{-}19)$$

where $u_m$ is the average velocity given by the ratio between the volumetric flow rate, Q, measured in the experiments and the cross section area of the test section $A_t$, so that the Reynolds number was the same as the experimental Reynolds number. Thus,

$$u_m = \frac{Q}{A_t} \quad (11\text{-}20)$$

Table 11.1: Data composition of the solution used in the experiments and simulations.

| **Carbon number** | **i** | **Feed molar fraction ($z_i$)** |
|---|---|---|
| 12 | 1 | $6.8117\ 10^{-01}$ |
| 22 | 2 | $1.5867\ 10^{-04}$ |
| 23 | 3 | $1.4925\ 10^{-03}$ |
| 24 | 4 | $8.1312\ 10^{-03}$ |
| 25 | 5 | $2.3242\ 10^{-02}$ |
| 26 | 6 | $4.0839\ 10^{-02}$ |
| 27 | 7 | $5.1932\ 10^{-02}$ |
| 28 | 8 | $5.2231\ 10^{-02}$ |
| 29 | 9 | $4.4272\ 10^{-02}$ |
| 30 | 10 | $3.3264\ 10^{-02}$ |
| 31 | 11 | $2.2986\ 10^{-02}$ |
| 32 | 12 | $1.5432\ 10^{-02}$ |
| 33 | 13 | $9.9747\ 10^{-03}$ |
| 34 | 14 | $6.3611\ 10^{-03}$ |
| 35 | 15 | $4.0292\ 10^{-03}$ |
| 36 | 16 | $2.3309\ 10^{-03}$ |
| 37 | 17 | $1.3308\ 10^{-03}$ |
| 38 | 18 | $5.4664\ 10^{-04}$ |
| 39 | 19 | $2.7629\ 10^{-04}$ |



With respect to the flow equations, no slip condition were imposed at the solid walls (copper and plexiglass walls). At the outlet plane, the diffusive flux of all variables was considered null. Thus,

$$\frac{\partial \phi}{\partial y}(x = L, y, t) = 0; \phi = U, V, T, cz_i \tag{11-21}$$

At the beginning of the process, the copper pipe wall temperature was the same as the inlet solvent-wax solution temperature. The initial condition was achieved after steady state was reached with the whole domain at the same temperature $T_{in}$. At this temperature above the WAT, no deposition was observed, and the thickness of the deposit was null, $\delta(x, t = 0) = 0$. The plexiglass wall had a constant temperature thermal boundary conditions. The copper wall was then cooled. During the initial cooling transient, the wall

axial temperature distribution measured from the thermocouples installed in the copper wall was imposed as boundary condition. After approximately 10 minutes, the wall temperature was constant and equal to $T_w = 12^oC$, the same constant value measured in the experiments.

### 11.1.7 Determination of the deposit thickness

The thickness of the deposit was determined as a post-processing operation of the numerical results. Based on information from the literature, it was arbitrated that 2% of solid was necessary to form an immobile deposit layer (Holder and Winkler, 1965; Singh et al., 2001a; Banki et al., 2008). It should be mentioned that the WAT estimated from the thermodynamic model corresponding to a solid saturation value equal to 2%, matched the measured WAT for the solution. This fact is an indication that the 2% value for the solid saturation is a reasonable assumption.

As wax is formed on the cooled copper pipe, a porous deposit is created initially displaying 98% of liquid. The solid saturation is calculated as a function of time, given by the ratio of the solid volume and total (solid and liquid) volume, ie,

$$S_s = \frac{\forall_s}{\forall_s + \forall_o} = \frac{m_s/\rho_s}{m_o/\rho_o + m_s/\rho_s} \tag{11-22}$$

The gel thickness layer grows with time as the copper wall is cooled, and the solid saturation increases. Once the steady state deposit thickness is attained, the deposit solid saturation may continue to rise, characterizing the aging process.

### 11.1.8 Validation of the numerical model

To validate the thermodynamic model, the equilibrium data obtained with the model were compared to experimental data published in literature. Dauphin et al. (1999) measured the composition of synthetic systems in the solid and liquid phases for temperature values below the WAT. The comparison showed that the mole fractions in the solid and liquid phases calculated using the model agreed quite well with the measured fractions in the temperature range used in Dauphin et al. (1999). The complete results of this validation tests can be found in Souza (2014).

To validate the annular geometry flow calculation implemented on a cylindrical coordinate system, comparisons were made of the numerical results with the analytical solutions for laminar, one-dimensional, fully-developed flow

in steady state, considering constant properties and no deposition of paraffin. Excellent agreement was obtained.

# 12
# Appendix B

## 12.1
## Systematic uncertainty caused by the traverse temperature probe

Special devices were developed in both test sections to access the temperature data of the wax deposit formed over the cold surfaces. The devices were designed to allow controlled positioning of a thermocouple probe. The device and the thermocouple itself were designed to be as little as possible, in order to minimize the disturbance of the flow. However, during the deposit–liquid interface measurements, the contact between the probe, heated by the wax mixture flow, and the cooled deposit–liquid interface could cause errors in the temperature measurements.

In order to quantify the probe errors, an analysis of the systematic uncertainty caused by conduction of heat though the probe was conducted. The analysis was based on a model proposed by Hennecke and Sparrow (1970). The model is based on the presence of a rod heated by forced convection touching a cooled surface as illustrated in figure 12.1. The rod in contact with the cooled surface behaves like a fin. In the calculations proposed by Hennecke and Sparrow (1970), the Biot number of the surface and the conductance of both the thermocouple and the surface are taken into account to estimate the temperature error.

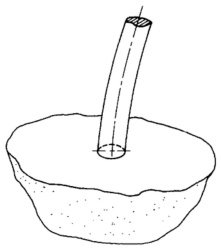

Figure 12.1: Illustration of the model based on a thermocouple installed at a cooled surface.

The final Reynolds number of the flow when a deposit is already present was used in the uncertainty calculation. The calculation was done for the two

geometries employed in the measurements of the deposit–liquid temperature, namely, the rectangular and annular test sections. The results are shown in table 12.1. In the table, the cases analysed are described by the initial Reynolds number on the top, and the time instant of the measurement on the left, for both test section cases. The systematic uncertainty is given in $^oC$.

Table 12.1: Uncertainty estimation in the interface temperature measurements, $\Delta T$, caused by forced convection.

| | Systematic uncertainty ($^oC$) | | | | | |
|---|---|---|---|---|---|---|
| | Annular Geometry | | | Rectangular Geometry | | |
| **time instant** | $Re = 743$ | $Re = 1440$ | $Re = 2073$ | $Re = 532$ | $Re = 876$ | $Re = 1737$ |
| 5min | 0 | 0 | 0.39 | 0 | 0 | 0 |
| 1h | 0 | 0 | 0.29 | 0 | 0 | 0 |
| 4h | 0 | 0 | 0.23 | 0 | 0 | 0 |
| 7h | 0 | 0 | 0.27 | 0 | 0 | 0 |

It was found that in the worst case, for the two geometries, the thermocouple touching the surface would measure a temperature around $0.4^oC$ higher than the actual interface temperature. So, if the surface would be at 36 $^oC$ the thermocouple would measure 36.39 $^oC$. Since the uncertainty evaluated here is systematic, the $\Delta T$ exhibited in table 12.1 was deduced from the data in the deposit–liquid interface temperature presented in the present work.